



HAL
open science

Spectroscopie à corrélation de fluorescence multi-confocale : développement et application à l'étude de la réponse cellulaire au choc thermique

Meike Kloster Kloster-Landsberg

► **To cite this version:**

Meike Kloster Kloster-Landsberg. Spectroscopie à corrélation de fluorescence multi-confocale : développement et application à l'étude de la réponse cellulaire au choc thermique. Autre [cond-mat.other]. Université de Grenoble, 2012. Français. NNT : 2012GRENY053 . tel-00770264

HAL Id: tel-00770264

<https://theses.hal.science/tel-00770264>

Submitted on 4 Jan 2013

HAL is a multi-disciplinary open access archive for the deposit and dissemination of scientific research documents, whether they are published or not. The documents may come from teaching and research institutions in France or abroad, or from public or private research centers.

L'archive ouverte pluridisciplinaire **HAL**, est destinée au dépôt et à la diffusion de documents scientifiques de niveau recherche, publiés ou non, émanant des établissements d'enseignement et de recherche français ou étrangers, des laboratoires publics ou privés.

THÈSE

Pour obtenir le grade de

DOCTEUR DE L'UNIVERSITÉ DE GRENOBLE

Spécialité : **Physique pour les Sciences du Vivant**

Arrêté ministériel : 7 août 2006

Présentée par

Meike Kloster-Landsberg

Thèse dirigée par **Antoine Delon**

et codirigée par **Irène Wang**

préparée au sein du **Laboratoire interdisciplinaire de Physique**
dans le cadre de l' **Ecole Doctorale de Physique, Grenoble**

Multi-confocal fluorescence correlation spectroscopy and its application to the study of the cellular response to heat shock

Thèse soutenue publiquement le 1er octobre 2012 ,
devant le jury composé de :

Franz Bruckert

Professeur, Phelma Grenoble, Président

Catherine Royer

DR Inserm, Centre de Biochimie Structurale Montpellier, Rapporteur

Claus Seidel

Professeur, Heinrich Heine Universität Düsseldorf, Rapporteur

Emmanuel Courtade

Maitre de Conférences, Laboratoire de Physique des Lasers, Atomes et Molécules Lille,
Examineur

Antoine Delon

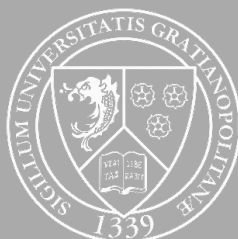
Professeur, Laboratoire interdisciplinaire de Physique Grenoble, Directeur de thèse

Irène Wang

IR, Laboratoire interdisciplinaire de Physique Grenoble, Invitée

Catherine Souchier

CR Inserm, Institut Albert Bonniot Grenoble, Invitée



Contents

Acknowledgments	ix
Summary/Résumé	xi
1. Introduction	1
2. Experimental methods	9
2.1. The experimental setup	9
2.2. Creation of multiple spots with an SLM	11
2.3. The EMCCD camera as a detector for FCS	14
2.4. Temperature control in the sample	16
2.5. Data acquisition	16
2.6. Data processing	17
2.6.1. Correction for offset and drift	17
2.6.2. Correction for crosstalk and background	21
2.6.3. Fit models	25
2.7. Dyes	28
2.8. Cell culture	29
3. Characteristics and performances of the mFCS technique	31
3.1. Spatial resolution for the different excitation and detection pathways	31
3.2. Sensitivity of the EMCCD camera compared to the APD	33
3.3. Calibration of the observation volume	34
3.4. Spots out of the optical axis	37
3.5. Comparison of single and multiple spot measurements	38
3.6. Control measurements in eGFP solution	40

4. Biological background	43
4.1. The heat shock response in eukaryotic cells	43
4.2. The structure of heat shock factor 1 (HSF1) and the deletion mutants	45
4.2.1. HSF1	45
4.2.2. The deletion mutants	46
5. Measurements in living cells	47
5.1. Protocol for measurements in living cells	47
5.2. Control measurements in HELA-eGFP cells	48
5.2.1. General remarks	48
5.2.2. Dynamics of an inactive eGFP molecule at 37°C and during heat shock	48
5.2.3. Influence of chromatin structure modifications during heat shock	51
5.2.4. Correlation between diffusion times measured in calibration and cell measurements	52
5.3. HSF1-eGFP in the heat shock response	53
5.3.1. General remarks	53
5.3.2. Changes in concentration and brightness of HSF1-eGFP .	54
5.3.3. Changes in the dynamics of HSF1-eGFP	56
5.4. HSF1-eGFP deletion mutants in the heat shock response	63
5.4.1. Control measurements in HELA-HSF1-eGFP and HELA- HSF1-eGFP siRNA cells	63
5.4.2. HELA-HSF1- Δ Trim-eGFP	65
5.4.3. HELA-HSF1-K80Q-eGFP and -HELA-HSF1-K80Q-eGFP siRNA	67
5.4.4. HELA-HSF1- Δ DBD-eGFP	70
5.4.5. HELA-HSF1- Δ AD2-eGFP siRNA	71
5.4.6. Overview over the dynamic properties of HSF1 and the deletion mutants	73
6. mFCS experiments with a CMOS-SPAD detector	77
6.1. The CMOS-SPAD camera as detector for mFCS	77

6.2. Data acquisition	78
6.3. Data processing	79
6.3.1. Calculation of the autocorrelation function	79
6.3.2. Correction for crosstalk and background effects	79
6.4. Calibration in solution	83
6.5. Measurements in HELA-eGFP cells	87
7. Conclusion	91
A. Appendix	97
A.1. Time resolutions for different EMCCD camera readout modes	97
A.2. Correlation between the fit parameters B and τ_{off}	98
B. Partie française	99
B.1. Introduction	99
B.2. Résumé et conclusion	106
C. Publications and presentations	113
Bibliography	115

Acknowledgments

Merci beaucoup à ...

- Catherine Royer et Claus Seidel d'avoir accepté de lire et évaluer mon manuscrit
- Franz Bruckert et Emmanuel Courtade d'avoir accepté de juger mon travail
- Antoine Delon pour m'avoir donné l'opportunité d'effectuer cette thèse passionnante sous sa direction, l'encadrement hors pair, son implication, le temps pour des discussions et sa porte qui était toujours ouverte
- Irène Wang pour la co-direction excellente, sa disponibilité pour des discussions et pour m'avoir prêté main forte
- Catherine Souchier, Gaëtan Herbomel et Claire Vourc'h pour leur collaboration agréable et fructueuse ainsi que pour leur patience en répondant à toutes les questions biologiques
- Yves Usson pour la collaboration agréable
- Rémi Galland pour m'avoir permis de bien démarrer sur la manip mFCS
- Philippe Moreau pour son soutien et pour les pauses de midi sympas
- Martial Balland pour ses conseils précieux et le bon état de la salle de culture
- MOTIV pour la bonne ambiance au quotidien
- LIPhy et son directeur Jacques Derouard pour le cadre scientifique stimulant
- l'Agence Nationale de la Recherche pour le financement (ANR-08-PCVI-0004-01)

Thanks a lot to ...

- David Tyndall and Robert Henderson for the pleasant collaboration on the mFCS-CMOS-SPAD project

Vielen Dank an ...

- meine Familie für die beständige Unterstützung
- Janek, dass er für mich da ist, ich mich immer auf ihn verlassen kann und er mich in allen Belangen bestärkt und unterstützt

Summary/Résumé

The cell nucleus is spatially heterogeneous in its structure and activity and many of its components are in dynamic interactions with each other. When investigating the cellular response to an external signal such as heat shock, standard fluorescence correlation spectroscopy (FCS) experiments, which are limited to one observation volume, do only give partial results because of the missing spatial information.

This work introduces a novel multi-confocal FCS (mFCS) technique that allows simultaneous FCS measurements in different locations within a cell. It is based on the use of a spatial light modulator (SLM) to create several distinct observation volumes at a time and an electron-multiplying charge coupled device (EMCCD) camera to perform parallel detection. The spatial resolution as well as the sensitivity of the mFCS system are close to that of a classical FCS setup and using a special readout mode, a temporal resolution of $14\mu\text{s}$ is reached.

The mFCS technique is applied to study the cellular response to thermal stress by monitoring the transcription factor heat shock factor 1 (HSF1), which is a key regulator of the heat shock response. mFCS experiments in living cells reveal changes in the dynamics of HSF1 upon heat shock. These changes concern the affinity as well as the spatial homogeneity of its interactions with DNA.

Additionally, the performance of a CMOS-SPAD camera, consisting of an array of single photon avalanche diodes, is evaluated and the device is tested as an alternative detector for mFCS in living cells.

Key words: FCS, spatial light modulator, electron multiplying CCD camera, CMOS-SPAD camera, heat shock, transcription factor HSF1

Le noyau d'une cellule est spatialement hétérogène par sa structure et son activité et beaucoup de ses composants interagissent de façon dynamique. Lors de l'étude de processus cellulaires comme la réponse au stress thermique, des expériences classiques de spectroscopie de corrélation de fluorescence (FCS), qui sont habituellement limitées à un seul volume d'observation, n'apportent que des résultats partiels à cause des informations spatiales manquantes.

Ce mémoire de thèse présente une nouvelle technique de FCS multi-confocale (mFCS) qui permet des mesures FCS simultanées à différents endroits d'une cellule. La technique est basée sur l'emploi d'un modulateur spatial de lumière pour la création de plusieurs volumes d'observations distincts et d'une caméra "electron-multiplying" CCD (EMCCD) pour la détection en parallèle. La résolution spatiale ainsi que la sensibilité du système mFCS sont proches de celles d'un système FCS classique et en utilisant un mode d'acquisition particulier une résolution temporelle de $14\mu\text{s}$ a pu être atteinte.

La technique mFCS est appliquée à l'étude de la réponse cellulaire au stress thermique en observant le facteur de transcription heat shock factor 1 (HSF1), qui est un régulateur clé de la réponse au stress thermique. Des mesures mFCS dans des cellules vivantes révèlent des changements dans la dynamique de HSF1 pendant le choc thermique. Ces changements concernent l'affinité ainsi que l'homogénéité spatiale des interactions avec l'ADN.

En outre, nous avons également évalué les performances d'une caméra CMOS-SPAD et testé le dispositif en tant que capteur alternatif pour la mFCS en cellules vivantes.

Mots-clés: FCS, modulateur spatial de lumière, caméra EMCCD, caméra CMOS-SPAD, choc thermique, facteur de transcription HSF1

1. Introduction

When Magde et al. published their results of the first fluorescence correlation spectroscopy (FCS) experiments in 1972, they stated that the method could have interesting applications in biophysics [1]. As it turned out, they were right. Especially since the combination with confocal microscopy [2–5], FCS has become a powerful tool to investigate the dynamics of fluorescently labeled biomolecules.

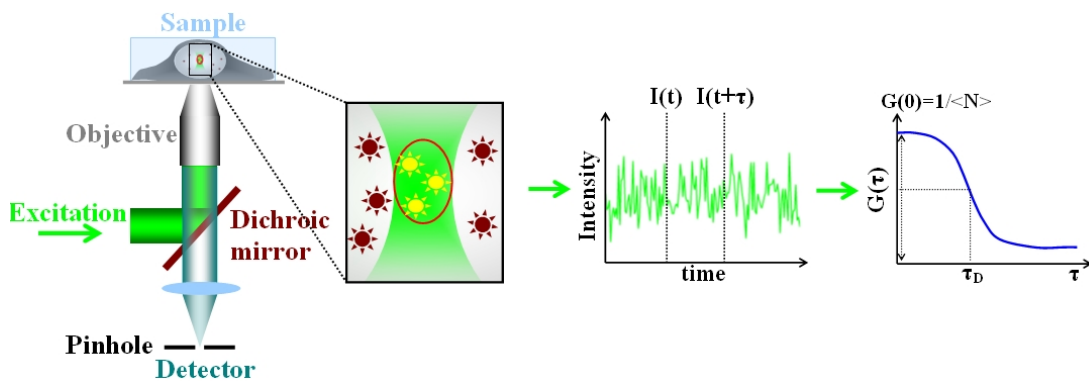


Figure 1.1.: Principle of the FCS technique. A fluorescent species is diffusing through the observation volume of a confocal microscope. Information about its concentration and dynamics is obtained by autocorrelating the resulting intensity fluctuations.

The technique is based on the study of small intensity fluctuations, caused by a fluorescent species that is diffusing through the observation volume of a confocal microscope (as depicted in figure 1.1). The observed intensity fluctuations depend on the concentration and the dynamics of the observed molecule or complex. The normalized autocorrelation of the detected intensity fluctuations yields the autocorrelation function $G(\tau)$, where τ is the lag time. Fitting a model to $G(\tau)$ yields the average number of particles N and their average residence time τ_D in the observation volume. When the size of the latter is known, absolute values

such as the concentration or the diffusion constant of the studied species can be calculated.

As FCS is very sensitive and non-invasive [6], it is well adapted to assess the dynamics of biomolecules in living cells. However, the cell and especially the cell nucleus, has a highly complex architecture. The latter features distinct compartments [7], such as nucleolus [8], splicing factor compartments [9], Cajal body [10] or chromosome territories [11, 12], which induce a heterogeneity in its structure and activity [13]. In addition, many nuclear components (chromatin, RNA, transcription factors,...) are in dynamic interaction with each other [7, 12]. In order to gather the necessary spatial and temporal information to gain some insight into the cellular machinery, measurements in several locations within the cell are required.

As the classical FCS technique is limited to one observation volume, spatial information can only be obtained by measuring successively in different positions. This task is time consuming and gives information from only one location at a time. However, fast temporal and spatial changes in the cellular activity can only be assessed if information from several different positions is monitored simultaneously.

In the last years several techniques based on fluorescence fluctuation spectroscopy have been developed to this end. One of them is temporal image correlation spectroscopy (tICS), which is based on taking images in a time series and spatially autocorrelating them [14–17]. Since the time resolution of this technique is limited by the frame rate of the camera, it is rather adapted to monitor slow dynamics. In order to overcome this limitation, Digman et al. developed a method called raster scanning image correlation spectroscopy (RICS) [18, 19]. RICS is based on the use of a laser scanning microscope [20–23] and gives access to spatial and temporal information within a wide range by correlating signals on adjacent pixels, lines or frames [18]. A disadvantage of this technique is that the region of interest (ROI) has to be rather large in order to avoid undersampling, which can result in an incomplete decay of the autocorrelation function and thus in an incorrect estimate of the dynamic parameters [24].

Instead of using a laser scanning microscope, Capoulade et al. [25] illuminated the sample by a light sheet and imaged the section on an EMCCD camera. Em-

ploying this technique, spatial and temporal information on an entire 2D section of a cell is available [25]. The limitation of the method is that the larger the section analyzed, the lower is the temporal resolution.

A technique that has been adapted to various biological problems is scanning FCS (sFCS) (see for example [26–34]). Spatial and temporal information is obtained by scanning the sample with one excitation volume, usually on a circle [31–34] or on a line [26–30]. By shifting the excitation volume, photobleaching effects are reduced and it is not necessary to know the exact position of the target, which is advantageous when measuring for example dynamics in membranes [14, 35]. The disadvantage of this technique is that a compromise between the spatio-temporal resolution and spatial extension has to be made. Furthermore it is not possible to get information independently and simultaneously from various locations within the cell, since only one excitation volume is used.

It is thus advantageous to create several independent excitation volumes at a time. To achieve this goal, spinning disk confocal microscopes have been employed in combination with CCD or EMCCD cameras [36, 37]. With these devices it is possible to create a large number of excitation volumes in a sample. In contrast, the time resolution is still limited by the readout rate of the camera.

A very promising approach is to combine a spinning disk confocal microscope with time-integrated multipoint moment analysis (TIMMA), which results in a time resolution of $20\mu\text{s}$ [38]. The TIMMA technique also uses an EMCCD camera for detection, but the dynamics of the probed fluorescent species is obtained from the dependence of the mean and the variance of the signal on the exposure time [38]. The temporal resolution is thus limited by the smallest possible exposure time of the camera and not by its readout rate. However, the implementation of this method is complicated. Amongst others, the readout noise has to be eliminated by splitting the signal into two identical pictures and calculating their covariance and the EMCCD camera gain has to be adjusted with increasing exposure times in order to avoid saturation of the detector [38].

A new multi-confocal FCS technique (hereafter called mFCS), which allows to assess the dynamics of the studied cellular component independently and at exactly the same moment in various locations within a cell with a high time resolution is thus interesting.

The first requirement on a mFCS technique is the creation of several independent excitation volumes. Originally it was intended to choose the location of the laser spots freely, while observing the cell in a wide-field acquisition. In order to create several laser spots in a user-defined geometry, a spatial light modulator (SLM) is used. SLMs are mainly known for their applications in optical trapping [39–41] and as wavefront correctors in astronomy [42], but are also well adapted for mFCS experiments. Blancquaert et al. for example measured molecular flows and the permeability of a phospholipidic membrane by means of spatial fluorescence cross correlation spectroscopy in two SLM generated observation volumes [43]. The initial idea of choosing the spot geometry adapted to each individual cell was not implemented for two reasons: Firstly, a precise alignment of every spot on a detector pinhole is required. An alignment procedure takes some minutes and is thus not compatible with measurements in living cells. Secondly, detection with high time resolution comes to the price of a spot geometry that is confined to one row. Nevertheless, the flexibility in spot positioning when using a SLM for excitation is advantageous, since the number of spots and their distances can easily be adapted before starting measurements.

The second challenge is to achieve detection in parallel: The detector has to be

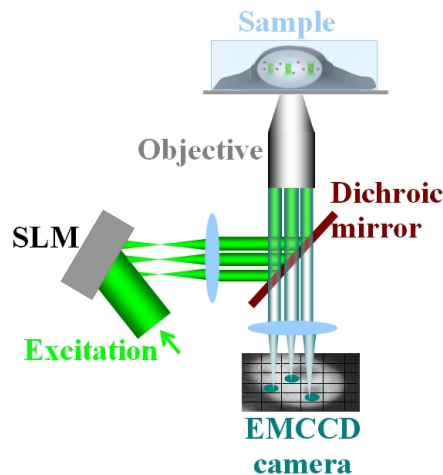


Figure 1.2.: Schematics illustrating the originally intended mFCS technique. Several laser spots can flexibly be positioned by a SLM in a geometry adapted to the respective cell. Detection is performed on the pixels of a EMCCD camera that act as individual pinholes for confocal detection.

a matrix of individual pinholes, sensitive to single photons and fast enough to obtain a temporal resolution that is compatible with the dynamics of the analyzed cellular component. To this end, an EMCCD camera has been used. It has already been shown that the pixels of an EMCCD camera can act as individual single photon detectors for FCS experiments [44–46] and that a high temporal resolution can be achieved by employing special readout modes. For example Burkhardt et al. [44] conducted FCS experiments with detection on an EMCCD camera in two excitation volumes in dye solutions and achieved a time resolution of $20\mu s$. In this work, the so-called Crop FvB readout mode is used, which results in a frame rate of 70kHz and thus a time resolution of $14\mu s$.

Newly emerging Complementary Metal Oxide Semiconductor-Single Photon Avalanche Diode (CMOS-SPAD) cameras offer the possibility of multiplexing and achieving single photon sensitivity with the time resolutions of APDs. The feasibility of mFCS experiments using an SLM for excitation and a CMOS-SPAD detector for detection in 8 and 64 spots in solution were recently shown by Colyer et al. [47, 48]. However, to the best of my knowledge the SLM-CMOS-SPAD system has up to now never been used for measurements in living cells and cross-contributions from neighboring spots are still an unsolved problem [48]. This is an important issue for measurements in living cells: The excitation volumes cannot be placed at a large distance from each other, since they have to fit in the same cell. In this work, a new CMOS-SPAD camera will be assessed as a detector for mFCS experiments, a solution to the crosstalk-problem will be proposed and the device will be tested for measurements in living cells.

The principal goal of this work is to develop the mFCS system and to use it to gain some insight into the cellular response to external stress. Antoine Delon and Catherine Souchier have chosen to study the dynamics of a transcription factor, heat shock factor 1 (HSF1), which plays a key role in the response to heat shock [49]. Upon heat shock, HSF1 is known to be activated, trimerized [49, 50], phosphorylated [51] and bound to specific binding sites on the DNA [52–54]. The number of these specific binding sites in the genome is limited [55]. The mFCS technique is thus perfectly adapted to assess the dynamics of HSF1, as it gives not only access to temporal, but also to spatial information. In addition, it yields a larger amount of data than the classical FCS technique, and should thus allow

to obtain statistically significant results in less time.

This work will thus answer three questions: The first one concerns the feasibility of mFCS experiments in living cells using an SLM for excitation and an EMCCD camera for detection. Are the spatial and temporal resolution adequate to measure the dynamics of HSF1 and how can the sensitivity of the system be classified compared to a classical FCS setup?

The topic of the second question deals with the dynamics of HSF1: In what way is it affected by heat shock? On what time scale does the binding to DNA take place and can it be assessed by mFCS? Are the interactions spatially homogeneous and which effect does the modification in the chromatin structure that occurs upon heat shock [56] have on the dynamics?

The last question is about the possibility to use a CMOS-SPAD detector for mFCS detection. How performant is it compared to the EMCCD camera and are measurements in living cells possible?

In order to answer these questions, this work is structured as follows: In chapter 2 the experimental methods are presented. The mFCS setup is introduced and the multi-confocal excitation via an SLM and the multiplexed detection with a EMCCD camera are explained. Subsequently, the data acquisition and processing methods are described. In addition, the protocol for cell culture is given.

Chapter 3 reveals the characteristics and performances of the mFCS technique, which will be compared to classical FCS experiments. In addition, the temporal and spatial resolution of the mFCS technique is analyzed and its strong points as well as its limitations will be pointed out.

Chapter 4 gives an overview over the heat shock response in eukaryotic cells, the structure and function of the transcription factor HSF1 and its deletion mutants. As a control, the dynamics of inert eGFP in living HELA cells will be analyzed in chapter 5. In the following, the impact of a heat shock on the dynamics of HSF1 will be studied. In order to clarify the role of the HSF1 domains, the dynamics of deletion mutants will be discussed.

In chapter 6 the possibility of using a new CMOS-SPAD camera as a detector for mFCS will be explored. After introducing the data processing, its performances will be assessed in control measurements in solution. The feasibility of measure-

ments on live cells is shown on HELA cells expressing the inert eGFP molecule. Chapter 7 closes this work with a conclusion.

2. Experimental methods

2.1. The experimental setup

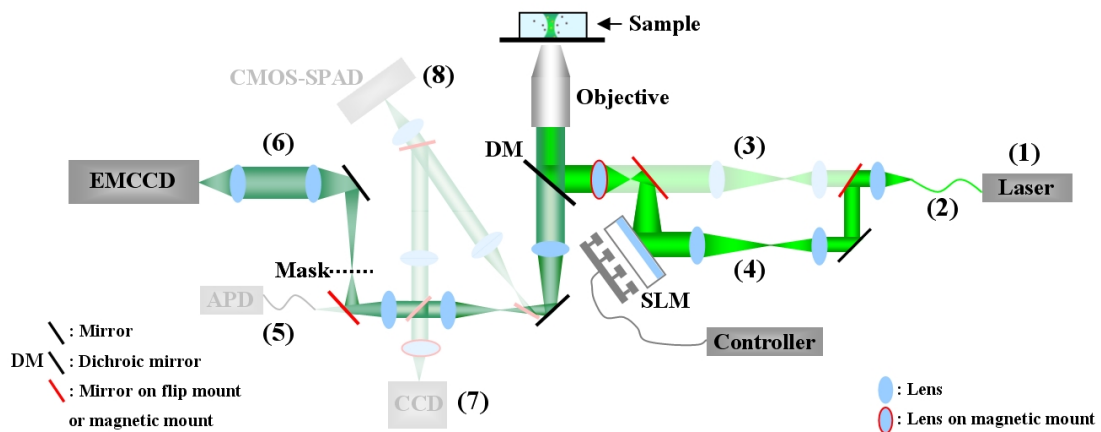


Figure 2.1.: Scheme of the mFCS setup. The highlighted pathway shows the excitation beam passing via an SLM in order to create several excitation volumes simultaneously and the parallel detection on an EMCCD camera. The non-highlighted pathway shows an alternative direct excitation pathway and further possibilities for detection pathways that lead to an APD for classical FCS, to a CMOS-SPAD camera or to a CCD camera for wide field imaging.

The mFCS setup (depicted in figure 2.1) is homebuilt and based on an inverted microscope stand (Olympus IX70, Olympus, Hamburg, Germany). A solid state laser (1) emitting up to 20mW of 488nm continuous wave light is used as excitation source (85-BCD-020, CVI Melles Griot, Albuquerque, NM). In order to get a spatially clean wavefront, the laser is coupled into a single mode fiber (2). The mFCS setup offers two different excitation and four detection pathways that can be switched by inserting or removing mirrors and lenses on flip or magnetic mounts.

The excitation pathway highlighted in figure 2.1 (4) is used to create multiple excitation volumes: The laser beam is expanded to the size of the active area of an SLM (LCOS-SLM X10468-01, Hamamatsu Photonics K. K., Hamamatsu City, Japan). Since the SLM only diffracts horizontally polarized light, the beam is guided through a half wave plate and a polarizer (not shown in figure 2.1). It then falls on the SLM, where its phase is modulated according to a phase map (see section 2.2) and focused in a plane that is optically conjugate to the microscope object plane. After being collimated the beam is reflected by a dichroic mirror and sent into a water immersion objective (Plan-apo $\times 60$, NA=1.2, Olympus). The focal length of the SLM has to be chosen in such a way that the width of the parallel light beam fits the pupil diameter of the objective lens. In order to conduct control measurements with a classical FCS excitation, this pathway can be bypassed by flipping two mirrors. In this case the beam passes a telescope before being sent into the objective.

In the following, indicated laser powers for excitation will refer to the power measured at the exit of the single mode fiber (2). For the direct excitation pathway (3), losses cause a difference of a factor 2.5 between this measured value and the excitation power in the sample. When using the SLM-pathway (4) for creating one spot, losses account for a factor 7.5 and multiple spots cause an additional reduction of about 20 % due to light that is not diffracted by the SLM.

After the fluorescent light has passed the dichroic mirror and is spectrally filtered (PH 510 Olympus, not shown in figure 2.1) it is directed to one side port of the microscope for detection. It can be chosen between three detectors for FCS measurements. For control measurements and comparison to classical FCS experiments the signal is directed to a multimode fiber that leads to an Avalanche Photo Diode (APD) (SPCM-AQR-13, Perkin Elmer, Waltham, MA) (5), where the fiber core (diameter $100\ \mu\text{m}$) serves as pinhole for confocal detection. The total magnification on this pathway is $316\times$.

The detection pathway highlighted in figure 2.1 (6) leads to an EMCCD camera (128×128 pixels, iXon+, Andor Technology, Belfast, Northern Ireland), which is the detector used for most mFCS measurements presented in this work. In this case the EMCCD camera pixels ($24\mu\text{m} \times 24\mu\text{m}$) act as pinholes. A mask, necessary for a special camera readout mode (described in section 2.3) can be

2.2. Creation of multiple spots with an SLM

Detector	Total Magnification	Size of the pinhole (μm)	Pinhole size in the object plane (nm)
APD	$316 \times$	$\varnothing 100$	$\varnothing 316$
EMCCD	$79 \times$	$\updownarrow \square 24$	$\updownarrow \square 304$
CCD (used with EMCCD)	$158 \times$	/	/
CMOS-SPAD	$13 \times$	$\varnothing 6.7$	$\varnothing 508$
CCD (used with CMOS-SPAD)	$60 \times$	/	/

Table 2.1.: Overview over the detectors used, the magnification on the respective pathway and the size of the pinhole for FCS detectors.

inserted in a plane optically conjugated to the microscope object plane. The total magnification on the EMCCD camera pathway was set to $79\times$ in order to get the same collection surface as for the $100 \mu\text{m}$ fiber core in the APD pathway. During mFCS experiments it is possible to switch to a CCD camera (Clara, Andor Technology) for wide field cell imaging without changing the alignment on the EMCCD camera pixels, which is rather sensitive to any shift of the laser spot images. This is done by inserting a mirror into the pathway. We refrained from using the front port of the microscope to fix the CCD camera, since it was found that changing between front and side port may alter the alignment on the detector. For wide field imaging an LED (Philips, Luxeon Rebel LXML-PB01-0023) with a main emission wavelength of 470nm is reflected into the microscope by a dichroic mirror (Semrock, LaserMUX LM01-480-25), which transmits the laser beam (not shown).

A second possibility for mFCS detection is to direct the signal to a CMOS-SPAD detector (Megaframe Project, The University of Edinburgh, Scotland). Here the SPADs (diameter $6.7 \mu\text{m}$) act as individual pinholes for confocal detection. The magnification in the CMOS-SPAD pathway is $13\times$. In this pathway as well, a mirror can be inserted during measurements to switch to the CCD camera for cell imaging.

2.2. Creation of multiple spots with an SLM

A liquid crystal on silicon SLM (LCOS-SLM) of 800×600 pixel (pixel size: $20 \mu\text{m}$) is used to create the desired number of diffraction limited spots in the

sample. The SLM consists of a layer of parallel aligned nematic liquid crystal (see figure 2.2) which has birefringent properties. The refractive index experienced by light traveling through this material depends on its relative orientation to the optical axis of the molecules in the layer (schematically depicted by $n_1 \neq n_2$ in figure 2.2). The SLM allows to modify the orientation of the molecules and thus the refractive index of the liquid crystal in every pixel by applying a voltage via a CMOS backplane [57, 58]. Since a difference in the refractive index implicates a change in the phase speed, the phase of the incoming wavefront can thus be modified in such a way that it focalizes (after reflection on a dielectric mirror) at a finite distance to the SLM in a user defined number of spots in the desired geometry.

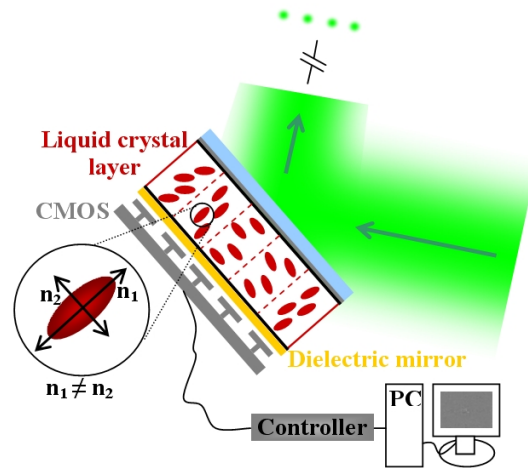


Figure 2.2.: Schematics of the SLM consisting of a layer of parallel aligned nematic liquid crystal, which has birefringent properties. The orientation of the molecules in the layer (and thus the refractive index of the material and the phase of an incident wavefront) can be changed in every pixel by applying a voltage via a CMOS backplane in order to get the desired spot geometry [57, 58].

There are several approaches to calculate the phase map that has to be applied to the SLM in order to get the desired result. Here, the so-called spherical wave and superposition approach as described in [59] is used, since it is efficient in terms of laser power and has a small computational time. The algorithm is based on the principle that each spot is the result of a converging spherical wave. The phase function can be found by back propagating and superposing the spherical

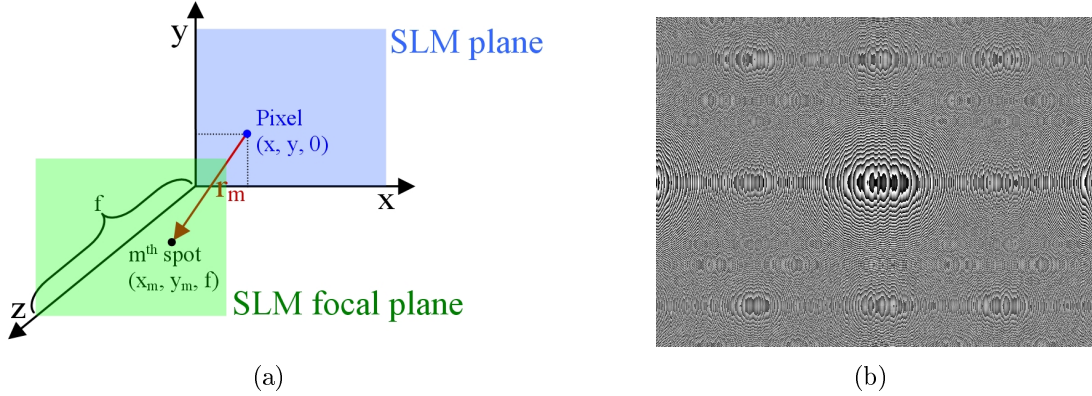


Figure 2.3.: Schematics illustrating the geometric relation between one pixel of the SLM and the m^{th} spot in the SLM focal plane (a). Example for a phase function applied to the SLM in order to generate five spots on a line (b).

wavefronts in the plane of the SLM. Since the SLM allows to control the phase, but not the amplitude of the incoming wavefront, the latter is not taken into account. The phase function is given by

$$\Phi(x, y) = \arg \left(\sum_m a_m \frac{\exp \left[-i \frac{2\pi}{\lambda} r_m(x, y) + \theta_m \right]}{r_m(x, y)} \right) \quad (2.1)$$

where a_m is an amplitude factor of the m^{th} spot, which is set to the reciprocal value of the obliquity factor for this work. As illustrated in figure 2.3(a), $r_m(x, y) = \sqrt{(x - x_m)^2 + (y - y_m)^2 + f^2}$ is the distance between the pixel with coordinates (x, y) on the SLM and the m^{th} spot in the focal plane of the SLM. The focal plane is located at a distance of 364 mm from the SLM for all measurements presented in this work. For each spot, a random phase θ_m between 0 and 2π is added to the phase function in order to avoid the occurrence of unwanted interference effects that manifest in “ghost” spots, which would partly consume the laser power and could also lead to additional photobleaching in the sample. Figure 2.3(b) is an example for a phase map applied to the SLM in order to generate five spots in a line.

When using the above described algorithm for the calculation of the phase map, the resulting spot intensities are often not uniform. In an extreme case, the intensities may differ by about 40%. However, when applying a correction for

crosstalk between the spots and for a background caused by non-diffracted light that is reflected by the SLM (see section 2.6.2), mFCS measurements are not affected by the differences in the spot intensities.

2.3. The EMCCD camera as a detector for FCS

An EMCCD camera with 128×128 pixels (pixel size: $24\mu m \times 24\mu m$) is used as a detector for parallel multi-spot detection. As in the EMCCD camera, charges are multiplied before readout, the signal-to-noise ratio can be considerably increased compared to conventional CCD cameras. Thanks to its high sensitivity, its pixels act as single photon detectors and play, as schematically depicted in figure 2.4 (a), the role of pinholes for confocal detection. However, the crucial point when using a EMCCD camera for FCS detection is the time resolution, which depends on the readout rate of the camera chip.

The experiments presented in this work have been done with the EMCCD camera operated in a frame transfer mode. In this mode the acquired image, or rather the charges corresponding to this image, are shifted from the image section of the camera chip to a storage section ([60], see figure 2.4 (b)). The storage section has the same size as the image section and is shielded with a mask. Once the charges are in the storage section a new image can already be acquired. From the storage section charges are first shifted vertically line after line into a readout register and then horizontally into a multiplication register where amplification takes place. The speed with which images can be acquired depends on the number of pixels that have to be read out and their position on the chip. Therefore, several readout modes exist that reduce the readout time and allow to achieve a higher time resolution.

Table A.1 in the appendix gives some examples for time resolutions that can be expected for reading a certain pixel configuration in different readout modes. In the following, the focus is set on the Crop (Full vertical Binning) FvB mode, since all experiments with the EMCCD camera presented in this work have been done using this specific readout mode.

In the Crop FvB mode, charges coming from the same column are binned verti-

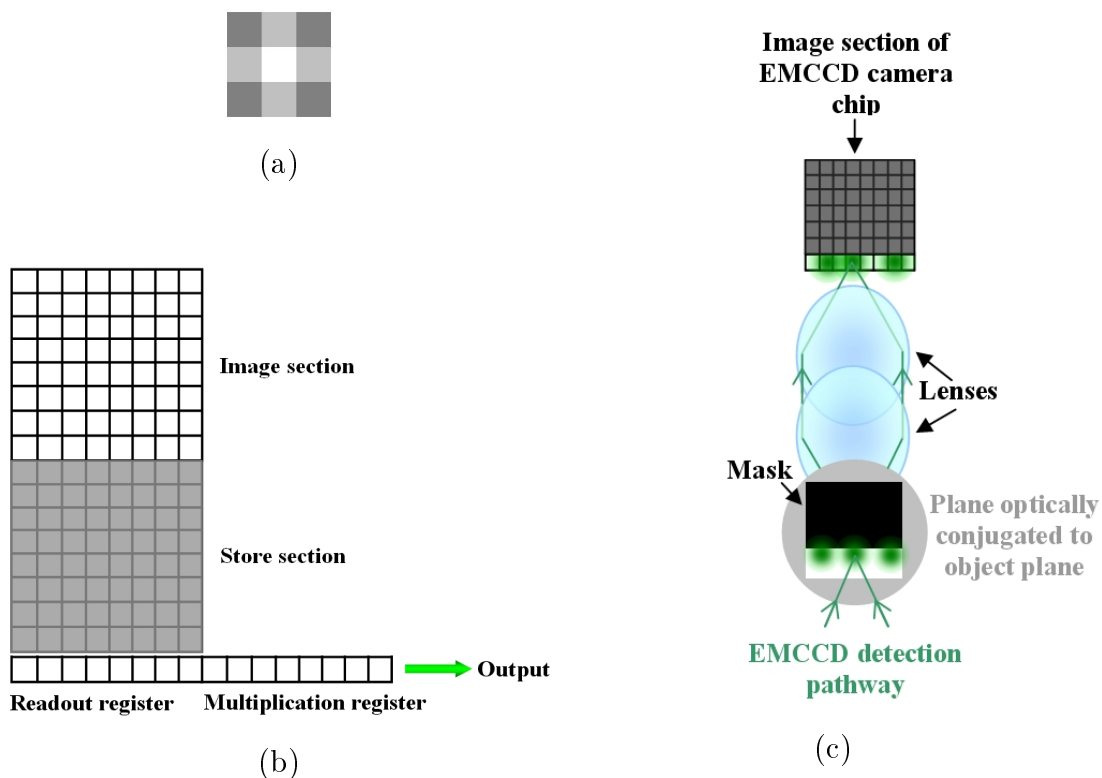


Figure 2.4.: Schematic representation of an EMCCD camera pixel playing the role of a pinhole for confocal detection (a). Schematics illustrating the functioning of an EMCCD camera in the frame transfer mode according to [60] (b). Scheme of the mask in the EMCCD detection pathway shielding the upper part of the EMCCD camera chip (c).

cally into the readout register. Thus, only one value per column has to be read out. The fluorescence signal is focused on pixels in the last line of the EMCCD camera chip, while a razor edge masks all other lines (figure 2.4 (c)). The mask is necessary in order to prevent out of focus light to deteriorate the signal. In this configuration, a frame rate of 70 kHz can be achieved, the price to pay is that the spot geometry is confined to one single row.

The EMCCD camera has been operated with an electron multiplying gain of 300 and a vertical shift speed of $0.25\mu\text{s}$. In order to enable an offset correction in the post processing of the acquired data (see section 2.6) the first five pixels of the last row have been masked as well.

2.4. Temperature control in the sample

For measurements in living cells, the temperature in the cell environment has to be controlled. Therefore, cells were cultured directly in a culture dish with a heatable (ITO coated) underside surface (Delta T, Bioptechs, Butler, PA). In addition, a heated lid (Delta T, Bioptechs, Butler, PA) and an objective heater (Bioptechs, Butler, PA) have been used to avoid non-uniform temperature distributions within the sample.

2.5. Data acquisition

In order to pilot the SLM, the EMCCD camera, the CCD camera, the laser shutter and the microscope stage comfortably during experiments on living cells, an interface in MATLAB (MathWorks, Natick, MA) has been developed for mFCS data acquisition and processing (figure 2.6). The Andor software development kit is used to access the two cameras via MATLAB.

mFCS measurements have been conducted with five spots focused on the bottom row of the EMCCD camera chip. The precise alignment of the laser spots on the EMCCD camera pixels is very important since any misalignment may alter the shape of the detection volume. Therefore, calibrations are performed in dye solution before measurements in cells and the correct position of the mask is checked (figure 2.5(a)). Once the spot positions are chosen and the corresponding phasemap is applied to the SLM, an automatic alignment procedure is performed. The first step consists in finding the spot center by three-point Gaussian fits and adjusting the phasemap applied to the SLM in order to center the spot on the nearest pixel. Afterwards, an iterative procedure adjusts the spots precisely on the pixels. Before and after passing a culture dish for measurements in cells, the correct alignment of the spots on the camera pixels is controlled with the help of a dye solution.

Each mFCS acquisition consists of the recording of a kinetic series of 700,000 images, which takes 10 seconds. In order to be able to continue directly with the next acquisition and not to lose time saving the images, the data is spooled to the hard drive. A series of five acquisitions and one offset acquisition with the

laser blocked is recorded automatically. During the post processing the acquisitions are corrected for the offset and the five acquisitions serve to calculate the mean and the standard errors for an autocorrelation function (see section 2.6). Prior to the measurements in cells the positions of the spots are marked on the CCD camera with the help of a dye solution. When passing the cells under the microscope, wide field images are taken on the CCD camera in order to find cells presenting a level of fluorescence compatible with FCS(see figure 2.5(b)). Wide field fluorescence excitation is performed using an LED (see section 2.1). Once an appropriate cell is found, its position is adjusted so that the spots are positioned in interesting locations within the cell. Afterwards, the detection path is switched to the EMCCD camera and one mFCS measurement, consisting of the five acquisitions and one offset recording is done. Then the position is slightly shifted and a second mFCS measurement is performed on the same cell. The position of the microscope stage can be marked, if the same cell shall be observed later on. Switching from EMCCD to CCD camera pathway requires only to move a mirror out of the pathway, so that the sensitive alignment of the spots on the EMCCD camera pixels is not altered.

2.6. Data processing

2.6.1. Correction for offset and drift

As the data acquisition, the data processing is performed using MATLAB. The upper left graph in figure 2.7 shows the intensity distribution on the entire last line averaged over the first 10,000 images of an acquisition (black) and the corresponding offset (red). The shape of the offset intensity profile on the last line is always identical, but its level varies from acquisition to acquisition. Therefore, the first five pixels of the last line are masked for all measurements. The measured intensity level in this masked region is averaged over the five pixels and over all 700,000 images and serves as reference point to adjust the offset level to the respective acquisition (upper right graph in figure 2.7).

An additional correction is performed for crosstalk between adjacent spots and for background effects due to non-diffracted light that is reflected by the SLM.

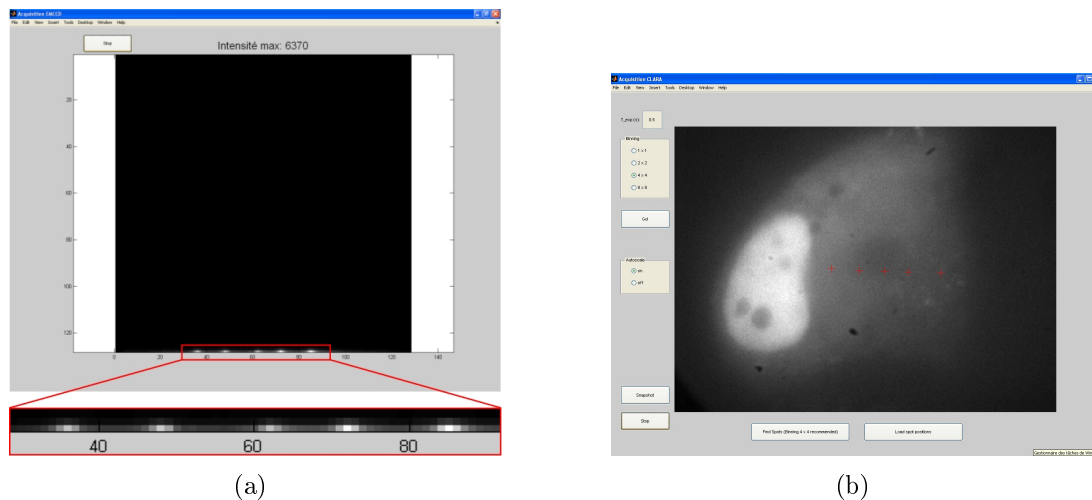


Figure 2.5.: Full image acquisition on the EMCCD camera which shows five laser spots aligned on pixels in the bottom line of the camera. A mask is shielding all lines above in order to prevent out of focus light from falling on the unused part of the chip (a). Wide field acquisition on the CCD camera in order to find FCS compatible cells and to place the spots in interesting locations within the cell (b).

This correction is discussed in section 2.6.2.

The signal from the pixels that serve as single photon detectors are extracted as a function of time. This is done for the five acquisitions and the corresponding offset measurement that has been adjusted beforehand. The level of the signal in acquisition and offset is usually drifting during the measurement time of 10 seconds. To correct for this drift, the acquisition time trace and the corresponding offset time trace are fitted with a 6th order polynomial. The fit of the offset trace (red curve in the lower right graph in figure 2.7) is then subtracted from the acquisition time trace (black curve). Afterwards, the resulting time trace is divided by the polynomial fit of the acquisition in order to eliminate drifts caused by the electronics or photobleaching effects (lower left graph in figure 2.7). The corrected time trace is finally used to calculate an autocorrelation function.

The five consecutive acquisitions yield five autocorrelation functions, which are used to calculate a mean autocorrelation function with standard errors of the mean. In this way a weighted fit can be performed. The fit models that have been used are described in section 2.6.3.

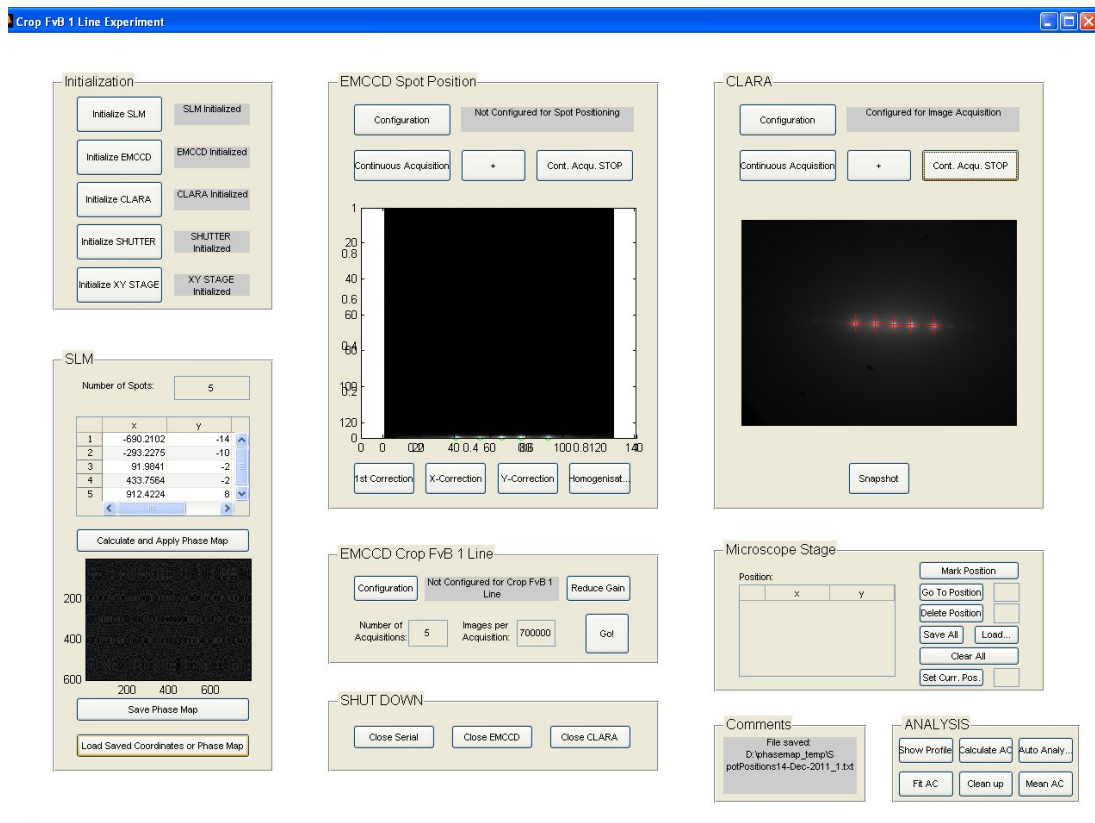


Figure 2.6.: Screenshot of the graphical user interface developed in MATLAB to pilot the mFCS setup. It allows to comfortably access SLM, EMCCD camera, CCD camera and microscope stage during an experiment.

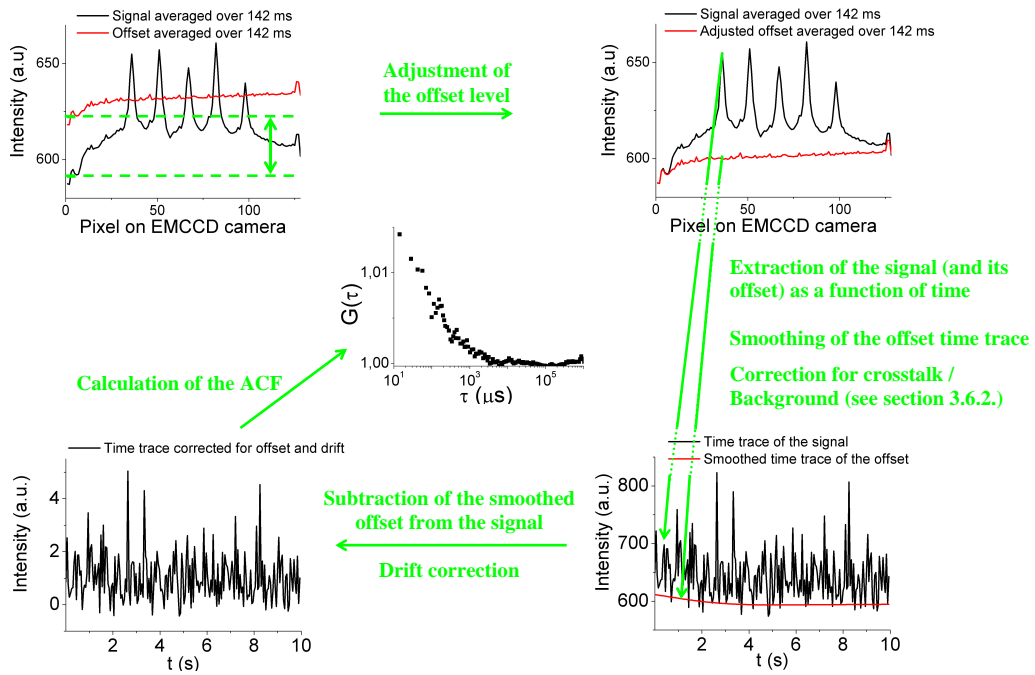


Figure 2.7.: Graphics describing the data post processing. The level of the offset is adjusted to the respective acquisition. Then the time trace of the signal on the interesting pixels is extracted from the acquisition and the corresponding offset. To correct for drifts, acquisition and offset are fitted by a 6th order polynomial and the offset fit is subtracted from the acquisition time trace. The result is divided by the polynomial fit of the acquisition and then used to calculate the autocorrelation function (ACF).

2.6.2. Correction for crosstalk and background

The spots in an mFCS experiment are typically spaced approximately 3 - 4 μm apart from each other. The black line in figure 2.8 shows the intensity profile on the last line of the EMCCD camera averaged over the first 10,000 images of an acquisition and corrected for the offset contribution. The intensity distribution of the fluorescence signal has a Lorentzian shape, with side wings that extend to some pixels distance (dashed light green line in figure 2.8). This implies that the signal measured on an EMCCD pixel on which one spot is aligned, does include the contributions from side wings of the other spots. The crosstalk contributions correspond to uncorrelated photons, which increase the estimated number of molecules in the multi spot measurement compared to a single spot measurement. This effect causes an important problem since the intensity distribution and the distance between the spots are usually not uniform. As the size of the contributions depends on these two factors, the spots are not affected in the same way by this crosstalk.

To correct for this effect, the first 10,000 frames of each acquisition are averaged to yield an intensity profile on the last line of the EMCCD camera. After correction for the offset, the profile is fitted with a multi peak Lorentzian function

$$L(x) = \left(\sum_{i=1}^n A_i \frac{p}{(x - x_i)^2 + p^2} \right) + c \quad (2.2)$$

(light green line in figure 2.8) where n is the number of spots, A_i an amplitude factor, p the half width of the peaks and x_i the position of the peak maximum. A pure Lorentzian distribution describes the peaks well in vicinity to the maxima, but a constant c (dark green line in figure 2.8) has to be added in order to reach a reasonably good fit for the pixels in between the spots. This constant factor accounts for the unfocused background that occurs due to non-diffracted light reflected by the SLM when creating multiple spots.

In order to eliminate the artifactual increase in the number of molecules for a given spot m , the side wing contributions of all other spots and the constant background

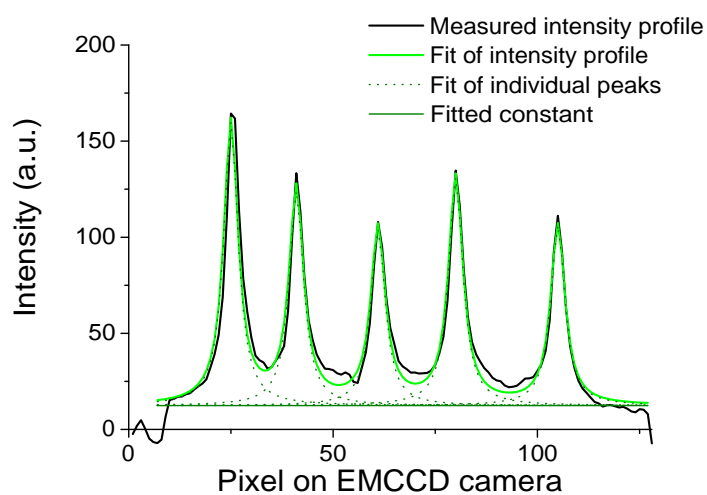


Figure 2.8.: Intensity profile on the last line of the EMCCD camera averaged over the first 10,000 images of an acquisition and corrected for the offset contribution (black line). The fit (light green line) is the sum of Lorentzian peaks (dashed light green line) and a constant background (dark green line). It is used to correct for an artifactual increase in the number of molecules caused by crosstalk between the spots and non-diffracted light reflected by the SLM.

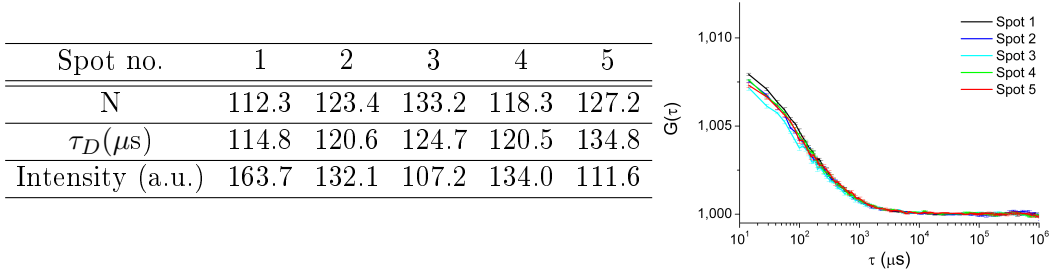


Figure 2.9.: Autocorrelation functions resulting from an mFCS experiment with five spots in a Dextran-Rhodamine Green solution without correction for crosstalk and background. The corresponding fit parameters N and τ_D are given in the adjacent table, as well as the corresponding spot intensities. N is correlated to the spot intensities.

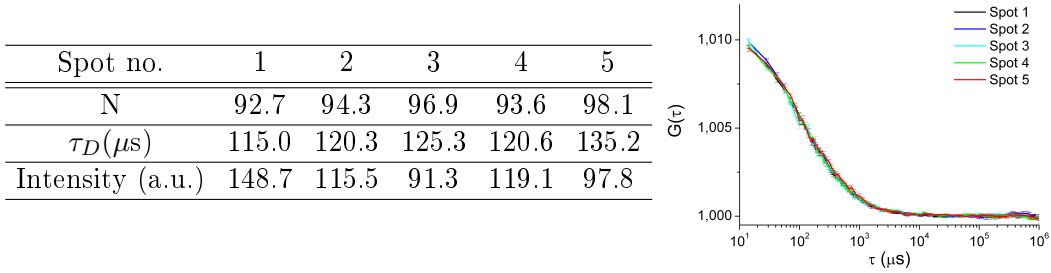


Figure 2.10.: Result of the same mFCS experiment as shown in figure 2.9 with the correction for crosstalk and background done in the post-processing of the data. N is almost uniform for all five spots and practically independent of the corresponding spot intensity.

on the pixel of spot m is subtracted from its time trace before calculating the autocorrelation function. The intensity to be subtracted is

$$L(x_m) = \left(\sum_{i=1, i \neq m}^n A_i \frac{p}{(x_m - x_i)^2 + p^2} \right) + c. \quad (2.3)$$

This correction is done for every spot in multi-spot experiments.

Figure 2.9 shows the autocorrelation functions resulting from an mFCS experiment with five spots in a Dextran-Rhodamine Green solution without correction. The corresponding fit parameters N and τ_D are given in the adjacent table, as well

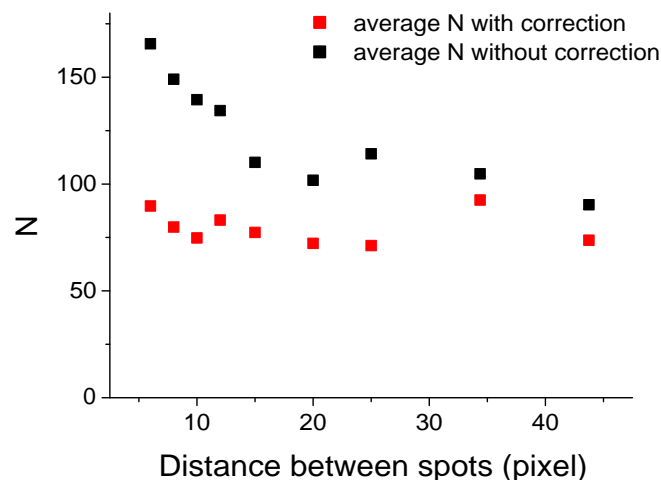


Figure 2.11.: Estimated number of molecules for five spots by varying the distances in between the spots in a Dextran-Rhodamine Green solution. If no correction for crosstalk and background is done (black squares) N increases with decreasing distance. The correction keeps N stable over a wide range of distances.

as the corresponding spot intensities. It can be seen that the measured number of molecules differ from each other and are correlated to the spot intensities. The lower the spot intensity, the higher is the number of molecules and vice versa. The reason is that the ratio of uncorrelated background photons and the signal is higher for low spot intensities than for high ones.

Applying the correction for crosstalk and background yields the autocorrelation functions shown in figure 2.10. The estimated number of molecules is very similar for the five spots and globally smaller after the correction.

An experiment that will be presented in section 3.5 shows that the corrected average number of molecules in multi-spot experiments is not significantly different from the number obtained in a single spot experiment.

Since the crosstalk between the spots increases with decreasing distances, another important question concerns the range of distances for which the correction is effective. Therefore, five spots with varying distances have been created in a Dextran-Rhodamine Green solution and are detected on the EMCCD camera. The estimated number of molecules for the corrected (red squares) and non-

corrected case (black squares) is averaged over all accessible spots (for distances larger than 25 pixels, the two outermost spots are located outside the field of view of the camera) and shown in figure 2.11. It can be seen that the artifactual increase in the estimated number of molecules gets more important with decreasing distances, which is expected. In contrast, when correcting for crosstalk and background the number of molecules is stable over a wide range of distances.

2.6.3. Fit models

The choice of a mathematical model that is adapted to describe the biological or physical situation is crucial for FCS experiments. Several different fit models have been used throughout this work in order to account for different conditions.

Model for measurements in dye solutions

To fit autocorrelation functions measured in Dextran-Rhodamine solutions, it was assumed that one species is freely diffusing in three dimensions. Since the temporal resolution of the APD is $0.2\mu s$, triplet relaxation had to be taken into account. The autocorrelation function in this case yields [61]

$$G(\tau) = 1 + \frac{\left(1 + \frac{T_{eq}}{1-T_{eq}} e^{-\frac{\tau}{\tau_T}}\right)}{N \left(1 + \frac{\tau}{\tau_D}\right) \sqrt{1 + \frac{\tau}{S^2 \tau_D}}} \quad (2.4)$$

where T_{eq} is the triplet fraction, τ_T the triplet relaxation time and N the average number of molecules in the observation volume. $\tau_D = \frac{\omega_r^2}{4D}$ is the diffusion time across the observation volume with ω_r being the radial elongation of the observation volume and D being the diffusion constant of the molecule. The structural parameter $S = \frac{\omega_z}{\omega_r}$ is the ratio of the axial ω_z to the radial elongation of the observation volume, which is assumed to have the shape of a three-dimensional Gaussian.

The temporal resolution for measurements with the EMCCD camera is $14\mu s$. Since the triplet dynamics is faster than this, it had not to be taken into account for EMCCD measurements. In this case equation 2.4 has been used with T_{eq} fixed to 0.

For measurements in solutions, the structure parameter S can normally be found without any problem and yields a value around 5. However, the dependence of the autocorrelation function on S is weak, so that the parameter cannot be reliably determined in the presence of noise. When fitting individual autocorrelation functions from measurements in cells, a freely varying S often results in an aberrant value. In order to avoid poor estimates of the other fit parameters in cell measurements and to treat the calibration measurements with equal measure, S was fixed to 5 for all fit results presented in this work.

Measurements in Dextran-Rhodamine Green solutions with detection on the APD have been fitted with equation 2.4 in Origin (OriginLab, Northampton, MA), using a Levenberg-Marquardt algorithm and a fitting range from $0.4\mu\text{s}$ to 800 ms. Measurements in Dextran-Rhodamine Green solutions with detection on the EMCCD camera have been fitted in MATLAB using the *fminsearch* function and thus employing the Nelder-Mead simplex algorithm as described in [62]. The fitting procedure using the *fminsearch* function was easier to implement and gives to a large extent the same results as the Levenberg-Marquardt algorithm. Data has been fitted in the time range from $14\mu\text{s}$ to 800 ms. In both cases, an instrumental weighting has been applied. It attributes a weight $\omega_i = \frac{1}{\sigma_i^2}$ to every measured point i , where σ_i is the size of the respective error bar [63]. The latter corresponds to the standard error of the mean of a set of five acquisitions. In that way, data points with large uncertainties are not as much considered in the fit as data points with small ones.

Model for measurements in living cells

To describe the results from measurements in cells, a model developed by Michelman-Ribeiro et al. [64] has been used. This model not only accounts for diffusion, but also for the binding and unbinding to an immobile substrate such as DNA with association and dissociation rate k_{on}^* and k_{off} , where k_{on}^* incorporates the concentration of free binding sites. Our data can be associated to the reaction dominant regime, which is a simplified model that is valid if the molecule diffuses much faster than it associates to the substrate ($\tau_D \ll \frac{1}{k_{on}^*}$). In this case, the autocorrelation yields:

$$\tilde{G}(\tau) = 1 + \frac{1}{N} \left(F_{eq} \frac{1}{\left(1 + \frac{\tau}{\tau_D}\right) \sqrt{1 + \frac{\tau}{S^2 \tau_D}}} + (1 - F_{eq}) e^{-\frac{\tau}{\tau_{off}}} \right) \quad (2.5)$$

Besides N , τ_D and S , there are two additional adjustable parameters namely $F_{eq} = \frac{k_{off}}{k_{off} + k_{on}^*}$, the fraction of free molecules at equilibrium and $\tau_{off} = k_{off}^{-1}$, the residence time. Since all measurements in cells have been done using the EMCCD camera as detector and thus with a time resolution of $14\mu s$, triplet dynamics has not to be taken into account.

In the autocorrelation functions calculated from measurements in cells, an artificial oscillation appears at long lag times of approximately 1s. The origin of this oscillation could not be determined without a doubt, however, we believe that it is due to the electronics of the EMCCD camera. The smaller the signal-to-noise ratio in a measurement, the more pronounced this artifact appears. For measurements in Dextran-Rhodamine solutions, the effect of the oscillation on the quality of the fit is negligible for the range of concentrations used. Since the count rate per molecule is about 1.7 times smaller for eGFP than for Dextran-Rhodamine Green and the concentrations measured in cells are comparatively high, the oscillations have to be taken into account in order to get a fit of good quality. Therefore, it was assumed that the detected intensity $I(t)$ is modulated with amplitude A and period T . With $F(t)$ being the intensity that would be detected without the existence of the artifact, $I(t)$ can be written as $I(t) = F(t) \left(1 + A \cos\left(\frac{2\pi t}{T} + \phi\right)\right)$. Assuming that there is no correlation between the fluctuation of $F(t)$ and the oscillation, the autocorrelation function of the measured signal is

$$G(\tau) = \tilde{G}(\tau) \left(1 + B \cos\left(\frac{2\pi\tau}{T}\right)\right) \quad (2.6)$$

where $B = \frac{A^2}{2}$ and $\tilde{G}(\tau)$ is the autocorrelation of $F(t)$. Data was fitted to this model in MATLAB using the Levenberg-Marquardt algorithm, which was found to be better adapted as the *fminsearch* function to perform a fit with additional free parameters. As for measurements in Dextran-Rhodamine Green solution the fitting range was set from $14\mu s$ to 800ms and an instrumental weighting has been applied.

As the period of the oscillation happens to be close to the residence time τ_{off} , one could ask if B and τ_{off} are independent from each other. A statistical analysis showed only a weak correlation between B and τ_{off} and confirms thus the validity of the parameter τ_{off} (see section A.2).

With a typical number of 1500 individual autocorrelation curves per measuring day, data processing (calculation of the autocorrelation functions and fitting) “by hand” would be very time-consuming, if not impossible. Therefore, the data analysis was automated and batch processed.

2.7. Dyes

Most calibration experiments and alignment tests were done using a solution of Dextran-Rhodamine Green 10kDa (Life Technologies, Grand Island, NY). The molecules were diluted in a buffer solution with pH 8.2 (in order to prevent aggregation) to concentrations in the range of 50nM to 1100nM without further purification. These molecules were chosen, because of their relatively large molecular weight, which makes their dynamics easily compatible with the time resolution of the EMCCD camera ($14\mu s$).

In addition, we used Rhodamine 6G (Radiant Dyes, Wermelskirchen, Germany) and Sulforhodamine G (Radiant Dyes, Wermelskirchen, Germany) diluted in pure water to a concentration of 500nM and 25nM respectively. Purified recombinant eGFP protein (Clontech, Mountain View, CA) was diluted in a buffer solution of pH 8.

In the experiments a droplet of the dye solution was disposed either in a perfusion chamber (Molecular Probes, Life Technologies, Carlsbad, CA) fixed on a heatable cell culture dish (Delta T, Bioprotechs, Butler, PA) or in a chambered coverglass (Lab-Tek, Thermo Fisher Scientific, Waltham, MA) in order to prevent evaporation.

2.8. Cell culture

Two different cell lines have been used to study the heat shock response, Human brain glioblastoma U87 cells and HELA cells. U87 cells and HELA-eGFP cells were cultured in Dulbecco's modified Eagle's medium (DMEM, PAA, Pasing, Austria), complemented with 10% fetal calf serum, 2% L-glutamine (4mM), 100 units per ml penicillin and 100 μ g/ml streptomycin (Gibco, life Technologies, Carlsbad, CA). In the case of U87 cells, 1% of non essential amino acids was added. Cells were grown at 37° in a 5 % CO_2 atmosphere.

Cells expressing HSF1-eGFP and HSF1-eGFP deletion mutants have been grown by Gaëtan Herbomel, PhD student at the Institut Albert Bonniot in Grenoble. The creation of the plasmid constructs for human HSF1-eGFP and the deletion mutants, the transfection, the establishing of stable cell lines as well as the silencing of endogeneous HSF1 are his work and therefore not described here. For the interested reader, these descriptions can be found in his PhD thesis.

During the two days preceding an experiment, the cells were grown in a heatable culture dish (Delta T, Bioptechs, Butler, PA). Just before the measurements the culture medium was replaced by DMEM without phenol red enriched with 1% fetal calf serum, 2% L-glutamine (4mM) and 10mM Hepes.

Under the microscope, cells were kept at 37°C and heat shock was performed at 43°C for one hour using the heating system described in section 2.4.

3. Characteristics and performances of the mFCS technique

3.1. Spatial resolution for the different excitation and detection pathways

In order to characterize the performance of the FCS system with an SLM for excitation and an EMCCD camera for detection, autocorrelation functions were measured for the different combinations of excitation and detection pathways. Figure 3.1 shows the result for the four possible combinations. When using the SLM for excitation, only one central spot was created. All measurements were done in the same Dextran-Rhodamine Green solution and the laser power was adjusted to yield the same value in the sample for both, the direct excitation pathway and the SLM excitation pathway, which implies more losses (see section 2.1).

The first eye catching difference between APD and EMCCD detection is the time resolution that is worse for detection on the EMCCD camera. As a consequence triplet dynamics can not be assessed when using the EMCCD camera.

When switching from the direct to the SLM excitation pathway, an increase in the number of molecules N is observed, which indicates an increased effective volume. From the increase in diffusion time τ_D , a radial enlargement of the observation volume can be concluded, since $\tau_D = \frac{\omega^2}{4D}$. This enlargement of the effective volume can be explained by the distortion of the wavefront by the SLM.

The use of the EMCCD camera detection pathway implies another enlargement

excitation	→	detection	N	$\tau_D(\mu\text{s})$	$\omega_r/\omega_r^{\text{direct}\rightarrow\text{APD}}$
direct pathway	→	APD	40.2	62.6	1.00
SLM pathway	→	APD	49.2	73.9	1.09
direct pathway	→	EMCCD	63.2	86.9	1.18
SLM pathway	→	EMCCD	92.0	114.6	1.35

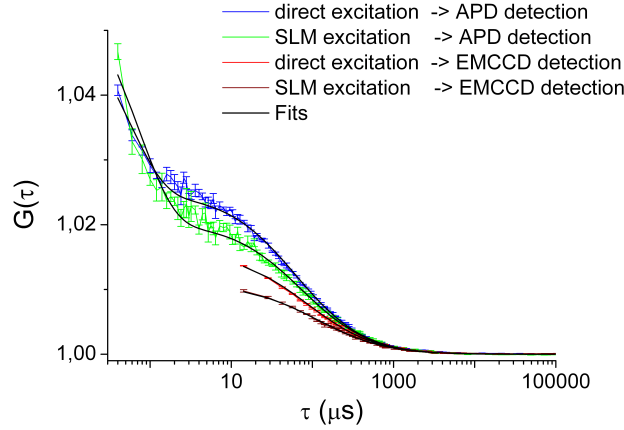


Figure 3.1.: Autocorrelation functions measured with the different combinations of excitation and detection pathways (blue, green, red, purple) and the estimated number of molecules and diffusion times that result from the fits (black). In addition, the radial elongation of the observation volume ω_r , which is normalized to its value for direct excitation and detection on the APD, is given. When using the SLM for excitation one central spot was created. Measurements were done in the same Dextran-Rhodamine Green solution and the laser power was adjusted to yield the same value in the sample in the four cases.

of the effective volume, compared to the APD detection pathway. The magnifications on the two pathways are adjusted to yield, in combination with the two pinholes of different size and shape (see table 2.1), approximately the same detection volumes. The magnifications, however, are extremely sensitive to the exact position of the lenses on the pathways and can be slightly different from the ideal values. In addition, the different shape of the pinholes (a circle for the multi-mode fiber core and a square for the EMCCD camera pixel) might play a role.

In conclusion, it can be said that the confocal volume does not change dramatically when using one spot created by the SLM for excitation and a pixel of the

EMCCD camera for detection, compared to a classical FCS experiment. The spatial resolution in this case is thus not far from the spatial resolution of a classical FCS system. However, there are differences that will be further analyzed and quantified in the following sections.

3.2. Sensitivity of the EMCCD camera compared to the APD

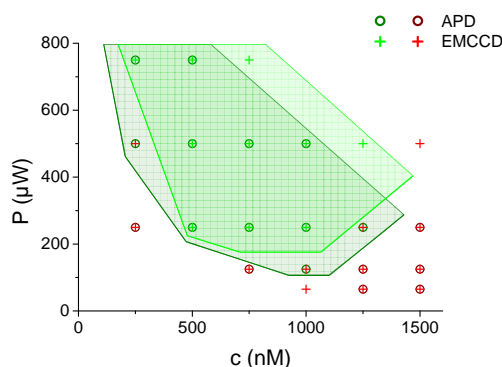


Figure 3.2.: Performance of the APD (circles) and the EMCCD camera (crosses) as a detector for FCS experiments at different distinct excitation powers and fluorophor (Dextran-Rhodamine Green) concentrations. Five spots were created and measurements were done in the central spot with both detectors. Green symbols stand for exploitable, red for non-exploitable results.

An important question concerns the sensitivity of the EMCCD camera as a detector for FCS. Because of the electron multiplication, the EMCCD camera is able to detect single photons. However, its mode of operation implies several sources of noise, which are not present when using an APD for detection. The main sources of noise are the vertical and horizontal shift of the charges before amplification and readout and the amplification process itself.

In order to test its performance, five spots were created by the SLM and the central spot was detected on both, APD and EMCCD camera. Solutions of Dextran-Rhodamine Green with varying concentrations were used and excitation power was adjusted to several distinct values. In order to allow a direct compar-

ison, no correction for crosstalk and background has been done for the EMCCD camera data, since it is impossible to treat the APD data in the same way. Furthermore, all autocorrelation functions were fitted starting from $14\mu\text{s}$ (which is the time resolution of the EMCCD camera). If the resulting autocorrelation functions yielded fits of a good quality, the result was judged exploitable. A “good” fit was defined to yield fit parameters with relative errors that are smaller than 5%. Green symbols in figure 3.2 indicate an exploitable result for the respective fluorophor concentration and excitation power when detecting on the APD (circle) or EMCCD (cross). Red symbols stand for non-exploitable results.

It can be seen that the sensitivity of the EMCCD camera comes close to that of the APD. For low laser powers or low fluorophor concentrations the APD yields a better performance. In contrast, for high count rates using an EMCCD camera for detection may be advantageous since the gain can be adjusted to avoid saturation or damage, which cannot be done with an APD.

In this experiment concentrations and excitation powers were decreased to such an extent that the artifactual oscillation in the EMCCD camera data (see section 2.6.3) is no longer negligible. By taking this artifact into account as done for measurements in cells, the fit for the EMCCD camera data at low count rates could be further improved. However, in order to compare the two detectors directly, the same fit model has been used for both cases.

3.3. Calibration of the observation volume

For all calibrations and alignments of the mFCS setup, an aqueous solution of Dextran-Rhodamine Green has been used. Because of their relatively large molecular weight of 10kDa, the dynamics of these molecules is easily detectable with the time resolution of the EMCCD camera ($14\mu\text{s}$). However, to determine the size of the observation volume, we choose to use a solution of Rhodamine 6G, since its diffusion constant is well documented in literature. Müller et al. [65] found a diffusion constant D of $(414 \pm 5) \frac{\mu\text{m}^2}{\text{s}}$ at $T = 25^\circ\text{C}$ for this molecule by

employing dual-focus FCS. Using the Stokes-Einstein equation

$$D(T) = \frac{k_B T}{6\pi\eta(T)R_H} \quad (3.1)$$

where k_B is the Boltzmann constant, $\eta(T)$ the temperature dependent viscosity of the solvent and R_H the hydrodynamic radius of the molecule, and accounting for the change in water viscosity between $T = 25^\circ C$ and $T = 37^\circ C$ with

$$\eta(T) = A * 10^{\frac{B}{T-C}} \quad (3.2)$$

with $A = 2.414 * 10^{-5} Pas$, $B = 247.8K$ and $C = 140K$ [66], a diffusion constant of $(555 \pm 7)\mu^2 s^{-1}$ at $T = 37^\circ C$ is obtained.

By creating one spot with the SLM and detecting the signal on the APD, the diffusion time of Rhodamine 6G was measured at $37^\circ C$. $D = \frac{\omega_r^2}{4\tau_D}$ yields, together with the diffusion constant calculated above and the measured diffusion time of $20\mu s$, a radial width of the observation volume of $\omega_r = (0.211 \pm 0.002)\mu m$.

The diffusion time of Dextran-Rhodamine Green was measured in the same conditions to be $67\mu s$. The diffusion constant of Dextran-Rhodamine Green at $37^\circ C$ is thus $D = (166 \pm 3)\frac{\mu m^2}{s}$.

As already briefly shown in section 3.1, switching from the APD to the EMCCD camera for detection causes a change in the size of the effective volume. In order to quantify these changes, FCS measurements were done in solutions of Dextran-Rhodamine Green within a wide range of concentrations. Therefore one spot was created by the SLM. Figure 3.3 shows the estimated number of molecules (a) and diffusion times (b) for detection on the APD (green squares) and on one pixel of the EMCCD camera (purple squares). The diffusion times are constant over the entire range of concentrations and the measured number of molecules increases linearly with the concentration in both cases. These results show that a large span of concentrations can be measured reliably by using an SLM for excitation and an EMCCD camera for detection.

The slopes of the linear fits to the measured number of molecules for APD and EMCCD detection differ from each other by a factor 1.4 when forced to intersect the origin (green and purple line in figure 3.3(a)). This indicates an enlarged

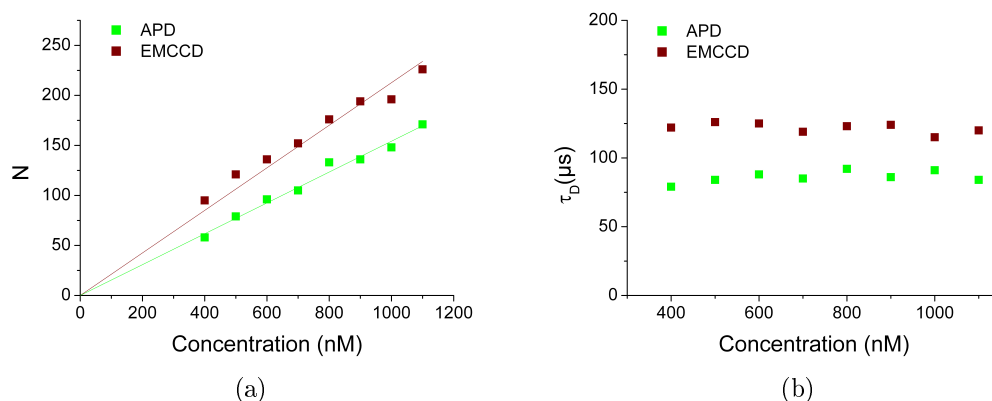


Figure 3.3.: Average number of molecules (a) and diffusion times (b) measured in solutions of Dextran-Rhodamine Green in a range of concentrations from 400nM-1.1 μM . One spot was created by the SLM and detection was performed on the APD (green squares) and on the EMCCD camera (purple squares). A large span of concentrations can be measured reliably with both detectors. The radial size of the observation volume is larger for detection on the EMCCD camera than for APD detection.

effective volume when detecting on the EMCCD camera. It may be caused by several factors: The magnifications on APD and EMCCD detection pathway are adjusted to yield together with the two different pinholes approximately the same detection volumes. However, the circular fiber core has a diameter of 25 μm in the plane of the square EMCCD pixel, the side of which measures 24 μm . This results in a detector area that is increased about 17% for the EMCCD detection pathway. In addition, the EMCCD detection pathway features one supplementary pair of lenses, which may give rise to additional aberrations. Another effect becomes obvious when fitting a linear slope to the estimated number of molecules against the concentration without forcing it to go through the origin: While N tends towards zero for a zero concentration in case of APD detection, it has a nonzero value for detection on the EMCCD. This effect can be considered as an artificial increase in the number of molecules, caused by a background of uncorrelated photons on the EMCCD camera.

The diffusion times found for EMCCD detection are 1.4 times larger than the values measured with APD detection (figure 3.3(b)). This indicates a lateral

enlargement of the observation volume when using the EMCCD camera for detection. Taking the radial size of the volume for APD detection and the difference in the diffusion times between APD and EMCCD detection into account and assuming a Gaussian volume, the lateral width of the volume for SLM excitation and EMCCD detection can be calculated to be $(0.251 \pm 0.002)\mu\text{m}$. The fits to the autocorrelation functions detected on both, APD and EMCCD camera yield generally the same structure parameter S , which is the ratio of the axial to the radial elongation of the observation volume. Therefore S has been fixed to 5 for the fits throughout this work.

3.4. Spots out of the optical axis

In an mFCS experiment spots are inevitably created outside the center of the field of view. Therefore, it is essential to investigate if the size and the shape of the excitation volume change when it is moved away from the optical axis. To accomplish this, one spot was created by the SLM in a Dextran-Rhodamine Green solution. The spot was then successively moved away from the optical axis in steps of $2.5\mu\text{m}$. After another measurement at the center, the observation volume was then shifted away in the opposite direction. While doing so, the EMCCD camera stayed fixed, so that different pixels were used for detection. The resulting number of molecules (black squares) and diffusion times (red squares) are given in figure 3.4. In a second measurement the spot was moved away from the optical axes in one direction with the EMCCD camera moving accordingly in order to eliminate possible effects related to the detection on different pixels (red and black crosses in figure 3.4).

In general, N and τ_D tend to increase when moving the observation volume away from the center, which indicates a lateral enlargement of the volume. This can be explained by optical aberrations getting more important with increasing angles. The measurements presented in this work were done with the spots at a distance of maximal $8\mu\text{m}$ to the optical axis. In this region, the effect is small compared to other sources of variations.

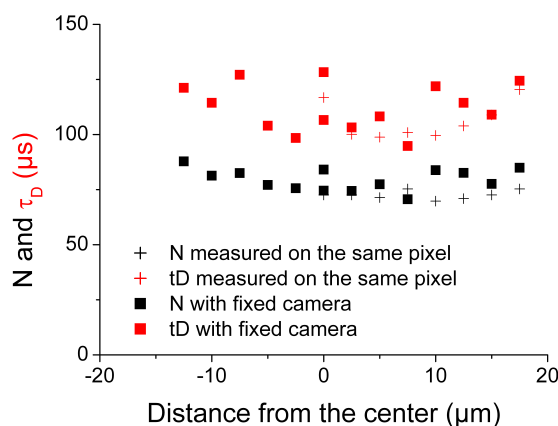


Figure 3.4.: Average number of molecules (black) and diffusion times (red) estimated from FCS experiments in a Dextran-Rhodamine Green solution. One spot was created by the SLM and shifted away from the optical axis in steps of $2.5\mu\text{m}$. In one case, different pixels of the EMCCD camera were used for detection (squares), in the other case, the camera was moved to detect the signal always on the same pixel.

3.5. Comparison of single and multiple spot measurements

Another important question is if the creation of multiple spots does alter the size and shape of the observation volumes. Figure 3.5 shows the average number of molecules (a) and diffusion times (b) estimated from FCS measurements with five spots in comparison to single spot measurements. The experiments were done in Dextran-Rhodamine Green solutions with varying concentrations. In one case, a single spot was created by the SLM and detected on the EMCCD camera (purple squares). In the second case, measurements were done in five spots simultaneously. The orange squares in figure 3.5 exemplarily depict the results for the middle spot.

It can be seen that the number of molecules measured for a given concentration is higher in the multi-spot measurement than in the single spot case. However, the diffusion times do not differ significantly, so that a radial elongation of the volumes can be excluded. As described in section 2.6.2, background and crosstalk

3.5. Comparison of single and multiple spot measurements

effects artificially increase the estimated number of molecules in measurements with multiple spots. After a correction for these effects (section 2.6.2), the average number of molecules estimated from mFCS measurements are close to that of single spot measurements (red circles). This shows that crosstalk and background effects, which only modify the average fluorescence signal compared to its fluctuations, are responsible for the higher number of molecules and that they can be corrected for. The size and shape of the observation volumes however do not change significantly when creating multiple spots, as the diffusion time is not affected by crosstalk.

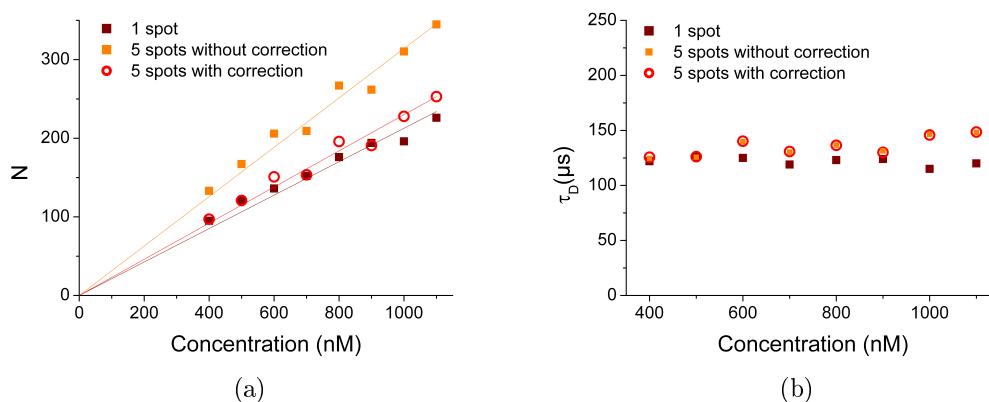


Figure 3.5.: Average number of molecules (a) and diffusion times (b) estimated from FCS measurements in a single spot (purple squares) and in the central spot of five spots (orange squares). Experiments were done in solutions of Dextran-Rhodamine Green with varying concentrations and detection was performed on the EMCCD camera. While the number of molecules is increased in the multi-spot case, the diffusion times do not differ significantly and thus indicate no radial enlargement of the observation volumes compared to the single spot case. The apparent increase in the number of molecules is due to crosstalk and background effects and can be corrected (red circles).

3.6. Control measurements in eGFP solution

Measurements in living cells were conducted on cells expressing the eGFP protein or the human HSF1-eGFP protein. These measurements were done at 37°C and 43°C respectively. Therefore, temperature induced changes in the eGFP characteristics might influence the results. FCS measurements were done on eGFP in aqueous solution in order to investigate its temperature dependent behavior.

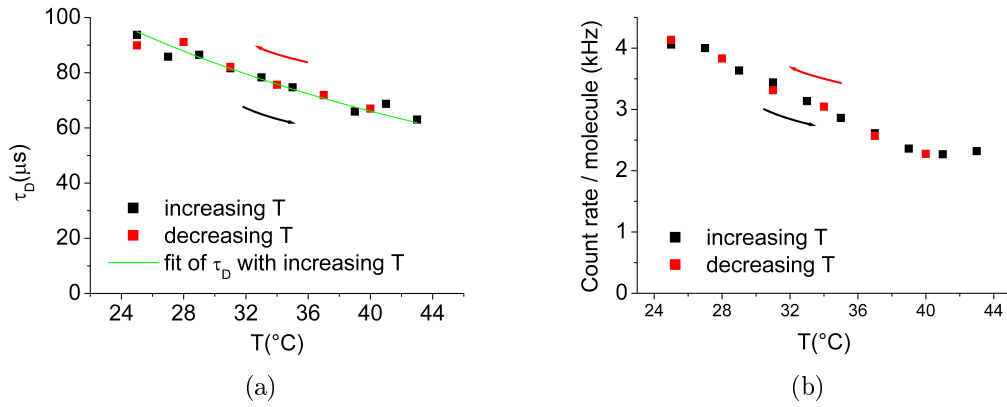


Figure 3.6.: Diffusion times (a) and count rates per molecule (b) estimated from FCS measurements in an aqueous solution of eGFP. A single spot was created with the SLM and detection was performed on the APD. Measurements were done at distinct temperature steps increasing (red squares) and decreasing (black squares) the temperature in the sample. The diffusion times measured with increasing temperature were fitted to a model (green line) in (a).

One spot was created by the SLM and detected on the APD. FCS measurements were done at several distinct temperatures going from 25°C to 43°C and as a control, from 40°C to 25°C. Figure 3.6 shows the diffusion times estimated from the fits to the autocorrelation functions (a) and the count rate per molecule (b). As expected, the diffusion times decrease with increasing temperature, since the water viscosity is decreasing.

In order to verify that only the change in the viscosity of the solvent and not a conformational change of the eGFP molecule is responsible for the variation in the diffusion time, $\tau_D(T) = \frac{\omega_r^2}{4D(T)}$ was fitted using equation 3.1 and equation 3.2. The hydrodynamic radius R_H was kept as the only free parameter. The green

line in figure 3.6(a) shows the fit to the data points measured with increasing temperatures. This fit gives an output parameter $R_H = (2.09 \pm 0.04)\text{nm}$ that is not far from published values [67]. Therefore, an effect other than the change in the solvent viscosity can be excluded within the measured temperature range.

With a lateral width of the observation volume of $\omega_r = (0.211 \pm 0.002)\mu\text{m}$, the diffusion constant is calculated to be in the range of $(119 \pm 2)\frac{\mu\text{m}^2}{\text{s}}$ at 25°C to $(177 \pm 4)\frac{\mu\text{m}^2}{\text{s}}$ at 43°C . These values are about 14 % larger and thus in reasonably good agreement with published values after correction for the different temperatures [33, 67].

The molecular brightness of eGFP is clearly decreasing with increasing temperature (figure 3.6(b)). Between 37°C and 43°C however, only a slight decrease of about 10% can be observed, which should not affect the measurements in living cells.

4. Biological background

4.1. The heat shock response in eukaryotic cells

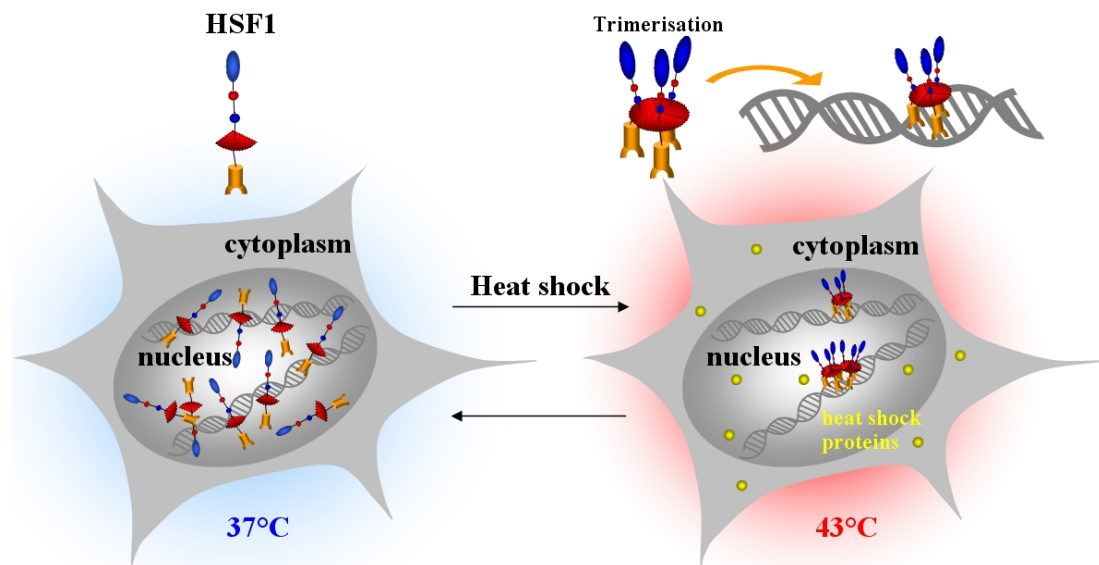


Figure 4.1.: Schematics depicting the heat shock response in eukaryotic cells. At a physiological temperature HSF1 is an inactive monomer in the nucleus. When the temperature raises above the physiological level, HSF1 is activated, trimerizes, is phosphorylated and binds to heat shock elements (HSEs) on the DNA. The expression and thus the concentration of heat shock proteins (molecular chaperones that counteract the deleterious effects of heat) is increased.

Cells have the ability to withstand (to a certain extent) a variety of stressors that they may encounter during their life cycle. One example is a shift in temperature to a few degrees above the physiological temperature of the organism. Since such a temperature shift is easily applicable to cultured cells under a microscope, the heat shock is a convenient model for studying the cellular response to stressful

conditions.

In a cell experiencing a heat shock, a process is launched to prevent damages due to the increased temperature. The transcription factor “heat shock factor 1” (HSF1) plays a key role in the heat shock response in eukaryotic cells [49]. The physiological temperature for the human cell lines used in this work is 37°C . At this temperature, HSF1 exists in an inactive (negatively regulated [68, 69]) monomeric form in the nucleus [70] as depicted on the left side in figure 4.1.

After an increase in temperature to 43°C , HSF1 is activated, trimerizes [49, 50], is phosphorylated [51] and binds to specific DNA sequences, the so-called heat shock elements (HSEs) on the DNA (as depicted on the right side in figure 4.1), which are located in the promoter sequences near heat shock protein genes [52–54]. As a consequence, the expression and thus the concentration of heat shock proteins (hsps) is increased [71]. At the same time, other transcriptional activity in the cell is globally reduced [72–74]. Hsps are molecular chaperones that counteract the deleterious effects of heat by supporting other cellular proteins in correct folding and thus preventing their degeneration [75]. Typically, a cell responds to heat shock within some minutes [76]. The knowledge about how the cell “senses” stress and induces a stress response is not yet exhaustive [69], but it has been suggested that the increase in the concentration of denaturated proteins, which goes along with a stressful condition, may trigger the stress response [77, 78].

In human cells, HSF1 does not only trigger the expression of hsps, but it also binds to specific satellite III repeats on the chromosome 9, where it accumulates [79]. These accumulations, which are called nuclear stress bodies (nSBs), go along with the heat shock response [80], but their exact function is not yet completely clear [81]. In cells expressing HSF1-eGFP, the nSBs manifest as bright spots in a wide field image (figure 5.4). The size of the nSBs increases with duration and intensity of the thermal stress and their formation is reversible [49, 82].

The time the cell needs to resume its normal functioning, when the temperature is back at a physiological level, depends on duration and intensity of the prior heat shock [83]. When a second heat shock is applied after the cell has recovered, nSBs are formed in the same positions as in the first one [82].

4.2. The structure of heat shock factor 1 (HSF1) and the deletion mutants

4.2.1. HSF1

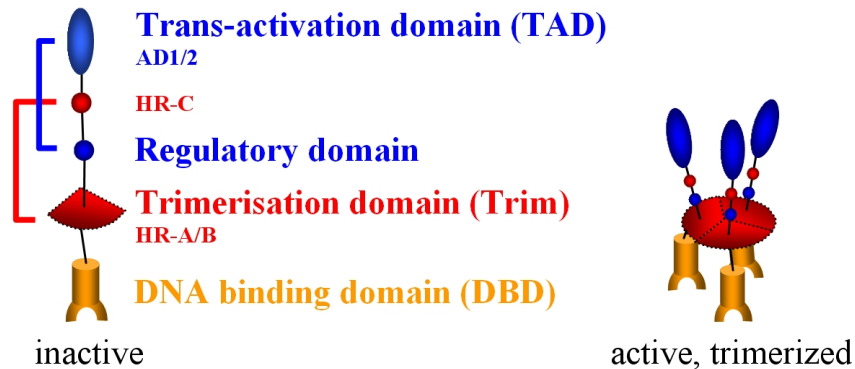


Figure 4.2.: Structure of the transcription factor heat shock factor 1 (HSF1) [68, 69]. In physiological conditions HSF1 is monomeric and inactive (left). Under stressful conditions it is activated and trimerizes (right).

Figure 4.2 depicts the structure of HSF1 [68, 69], which consists of several domains. The **DNA binding domain (DBD)** binds to the HSEs on the DNA, which are composed of inverted repeats of the sequence nGAAn (n can be any nucleotide) [52–54]. A functional HSE seems to contain at least three repeats of this sequence [52]. It has been shown that the formation of HSF1 trimers is necessary to bind with high affinity to the DNA [84, 85].

Trimerization occurs via a three-stranded coiled-coil configuration [85–87] in the **trimerization domain (Trim)**. The Trim domain consists of two subdomains, HR-A and HR-B, featuring hydrophobic heptad repeats. The HR-A domain is capable of forming trimers, while the HR-B domain seems to stabilize the complex [87]. In order to keep HSF1 under physiological conditions monomeric, the HR-C region, which also consists of hydrophobic heptad repeats, interacts with the HR-A/B region [69, 88].

The **trans-activation domain (TAD)** consists of two activation domains, AD1 and AD2 [89, 90]. Since these subdomains differ in their structure, it has been proposed that each of them might activate transcription by means of its own

mechanism [89]. In the inactive HSF1, the TAD domain is inhibited by the **regulatory domain** [89, 90].

4.2.2. The deletion mutants

Cells expressing HSF1-eGFP and HSF1-eGFP deletion mutants have been grown by Gaëtan Herbomel, PhD student at the Institut Albert Bonniot in Grenoble. mFCS experiments were done on the deletion mutants in order to investigate the impact of a missing or mutated domain on the HSF1 dynamics in heat-shocked cells.

In the Δ Trim mutant, the Trim domain is deleted (figure 4.3(a)). In the K80Q mutant, the lysine K80, which is located in the DBD domain and crucial for binding to the DNA, has been replaced by glutamine [91] (b). The Δ DBD mutant in contrast lacks the entire DBD domain (c) and in the Δ AD2 mutant the AD2 domain has been deleted from the TAD domain (d).

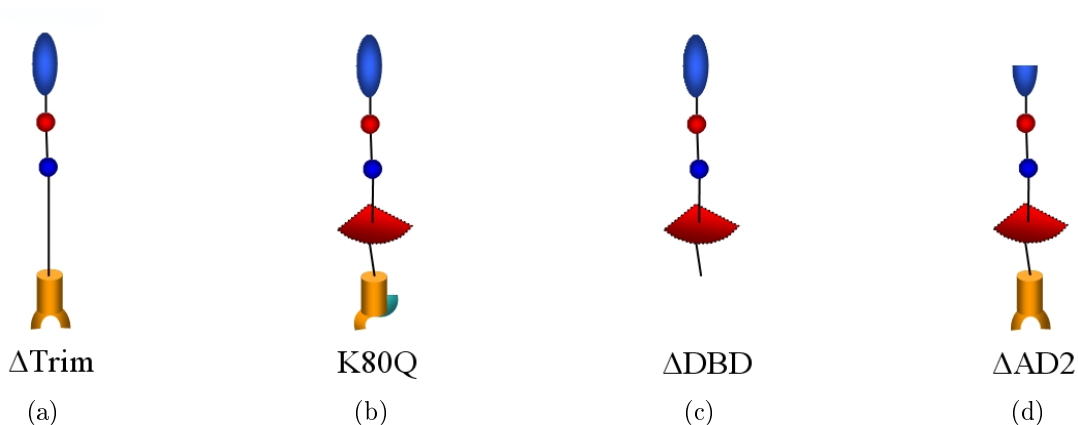


Figure 4.3.: Schematics of the HSF1 deletion mutants. In the Δ Trim (a), the Δ DBD (c) and the Δ AD2 mutant (d), the Trim, DBD and AD2 domain have been deleted respectively. In the K80Q mutant (b) the lysine K80 has been replaced by glutamine [91].

In order to investigate the characteristics of HSF1-K80Q-eGFP and HSF1- Δ AD2-eGFP, the endogenous HSF1 in the cells expressing these deletion mutants was silenced using small interfering RNA (siRNA [92, 93]). Thus, interactions with endogenous HSF1 could be excluded.

5. Measurements in living cells

5.1. Protocol for measurements in living cells

In a typical day of measurements, experiments were conducted on three culture dishes. In each culture dish, mFCS was done on five cells before heat shock at 37°C and on the same heat-shocked cells at 43°C . Before the insertion and after the removal of each culture dish, the exact alignment of the laser spot on the EMCCD camera pixels was verified using a dye solution and employing the alignment procedure as described in section 2.5.

For measurements in living cells, the laser power at the exit of the single mode fiber was always set to $120\mu\text{W}$. This value was found to be the best possible compromise between limiting photobleaching effects and maximal signal-to-noise ratio.

Measurements were first done at 37°C . Five spots on a line were placed in a cell, preferentially in the nucleus, but not in a nucleolus. One measurement consisted of five consecutive acquisitions and one offset acquisition of 10 s each (for more details see section 2.5). After slightly shifting the spot positions, a second measurement was done in the same cell. The position of the microscope stage was saved in order to be able to measure in the same cell in heat-shocked state.

Heat shock was done for one hour at 43°C under the microscope. In the following, two mFCS measurements were recorded on each of the five cells.

In total, one culture dish stayed for approximately two hours under the microscope.

Autocorrelation functions were fitted either with a pure diffusion model or with the diffusion-interaction model (equation 2.5). For the fit of individual autocorrelation functions, the period of the oscillation T_{osc} was fixed to 1.8s. The criteria

for retaining an autocorrelation function for statistical analysis were that the fit had to yield values that were consistent with the model and that the parameters were non-aberrant (less than a factor 10 from the mean value).

5.2. Control measurements in HELA-eGFP cells

5.2.1. General remarks

In order to investigate if effects apart from the heat shock response influence the measurements in cells at $37^{\circ}C$ and $43^{\circ}C$, control measurements were done in HELA cells expressing an inactive eGFP molecule. mFCS measurements were conducted on cells in three culture dishes. In two of them, measurements were first done at $37^{\circ}C$ and afterwards on heat-shocked cells at $43^{\circ}C$. In the third one in contrast, measurements were first done on heat-shocked cells at $43^{\circ}C$ and subsequently at $37^{\circ}C$ in order to identify potentially irreversible experimental artifacts.

In 280 out of 300 measurements, the spot was located inside the cell and resulted in an exploitable autocorrelation function. Figure 5.1 shows an example for the location of the five spots in a HELA-eGFP cell and the resulting five individual autocorrelation functions.

5.2.2. Dynamics of an inactive eGFP molecule at $37^{\circ}C$ and during heat shock

All exploitable autocorrelation functions were fitted with a simple diffusion model (equation 2.5 with $F_{eq} = 1$). In table 5.1 the mean values for the fit parameters N and τ_D and the corresponding standard deviations (SDs) are shown for the two temperatures. An ANOVA test revealed no significant influence of the temperature, the localization of the spots (nucleus or cytoplasm) or the order of the temperature change on the fit parameters N and τ_D . The overall value for τ_D varies broadly (as reported in [94, 95]) with a median of $422\mu s$. With a lateral width of the observation volume of $(0.251 \pm 0.002)\mu m$, the median diffusion constant (\pm its median absolute deviation (MAD)) for the inactive eGFP molecule

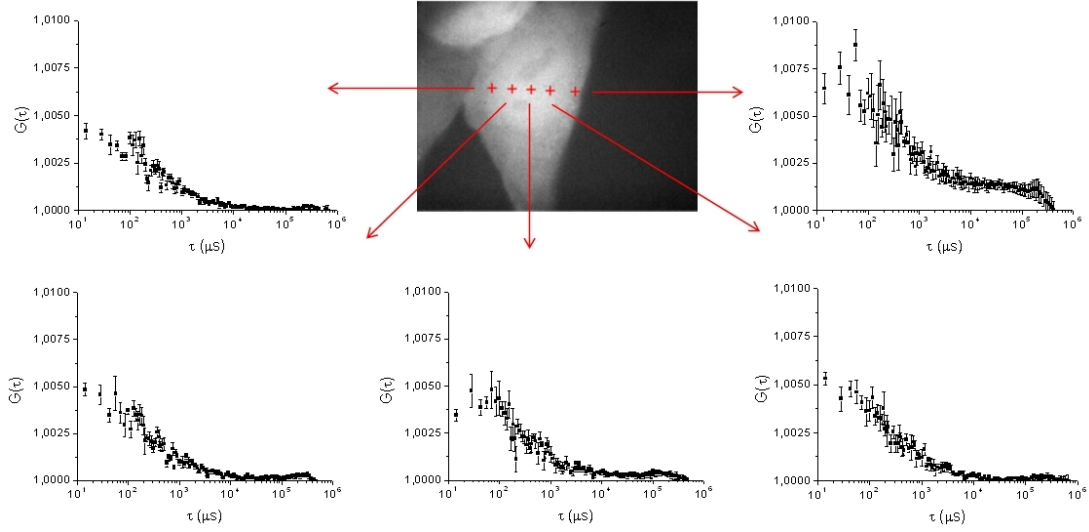


Figure 5.1.: An example for five individual autocorrelation functions measured in one HELA-eGFP cell. Spot 1-4 (from the left) are located in the nucleus, spot 5 in the cytoplasm.

in a HELA cell is found to be $(37 \pm 16) \mu\text{m}^2\text{s}^{-1}$. The diffusion constant for eGFP in the nucleus and in the cytoplasm of HELA cells is thus about four times lower than the diffusion time of eGFP measured in aqueous solution (cf. section 3.6). This result is in good agreement with experiments done by Seksek et al. [96], who found a similar ratio between diffusion constants of FITC-dextran and Ficoll molecules of different sizes in water and in the nucleus and cytoplasm of MDCK epithelial cells.

Parameter	Mean parameter \pm SD		p
	37°C (143 ACFs)	43°C (137 ACFs)	
N	267 ± 120	259 ± 113	○
$\tau_D(\mu\text{s})$	495 ± 383	534 ± 469	○
Intensity/Molecule (a.u.)	94 ± 36	77 ± 23	***

Table 5.1.: Mean fit parameters and intensity per molecule for 280 autocorrelation functions measured in HELA-eGFP cells and fitted with a simple diffusion model. The temperature has no significant influence on N and τ_D , but the intensity per molecule decreases with increasing temperature. Significance levels: ***: $p < 0.001$, **: $0.001 < p < 0.01$, *: $0.01 < p < 0.05$, ○: $0.05 < p$

The negligible influence of the temperature on the dynamics and the concentration of eGFP in HELA-eGFP cells is depicted in figure 5.2. It shows the mean over a subgroup of 38 autocorrelation functions measured in the nuclei of five cells at 37°C (blue) and 43°C (red) and the corresponding fit parameters N and τ_D .

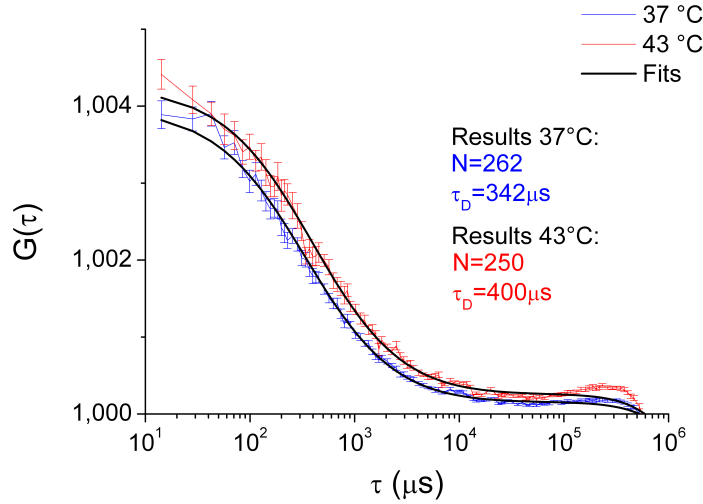


Figure 5.2.: Mean over a subgroup of 38 autocorrelation functions measured in five spots located in the nuclei of 5 HELA-eGFP cells at 37°C (blue) and 43°C (red). There is no significant change in the concentration and dynamics of eGFP when a heat shock is applied.

The only parameter changing with the temperature is the measured intensity per molecule. Its mean value (\pm its standard deviation (SD)) decreases from (94 ± 36) (a.u.) at 37°C to (77 ± 23) (a.u.) at 43°C , which can be explained by a decrease of brightness of the eGFP molecule with increasing temperature (see section 3.6).

For fits to the data obtained from cells expressing HSF1-eGFP, a diffusion-interaction model (equation 2.5 with F_{eq} and τ_{off} varying freely) was used, since the simple diffusion model did not give satisfactory results. In order to treat all cases with equal measure and to be able to compare eGFP and HSF1-eGFP dynamics directly, the autocorrelation functions obtained from HELA-eGFP cells were additionally also fitted with the diffusion-interaction model. The reduced χ^2

parameter, which is an indicator for the quality of the fit, did not change significantly. On the contrary, the fit parameters F_{eq} and τ_{off} did not converge towards reasonable values in more than 30% of the cases, whereas the simple diffusion model holds. This indicates that the parameters F_{eq} and τ_{off} are poorly defined in this kind of problem, in contrast to measurements in cells expressing HSF1-eGFP, where the diffusion-interaction model usually yields reasonable values (see section 5.3). However, also with this model we could conclude that N and τ_D are independent of the temperature as it is the case for the simple diffusion model. Since the fit parameter τ_{off} deviates a part of the behavior at long lag times from the parameter τ_D , the value of the latter is roughly reduced by half compared to the simple diffusion model. These results will be further discussed in section 5.3.

5.2.3. Influence of chromatin structure modifications during heat shock

Histones are cellular proteins, which contain positively charged amino acids and are one of the main component of the chromatin [97]. It has been shown that the accessibility of chromatin depends on the acetylation level of the histones [97–100]. Görisch et al. [98] observed that areas in the chromatin get less compact upon acetylation since Dextran can diffuse into regions that were inaccessible to them before. As a heat shock implicates the deacetylation of histones [56], one could assume that the resulting structural change in the chromatin restricts the protein mobility in the cell.

However, the mean diffusion time of inert eGFP molecules does hardly change during heat shock (see chapter 5.2.2). In solution, an increase in the mobility of eGFP molecules with increasing temperature could be observed due to a decrease of the solvent viscosity (see section 3.6). Therefore, one could reason that the slowdown caused by the structural change in the chromatin during heat shock in HELA-eGFP cells is to a large extent counterbalanced by viscosity effects.

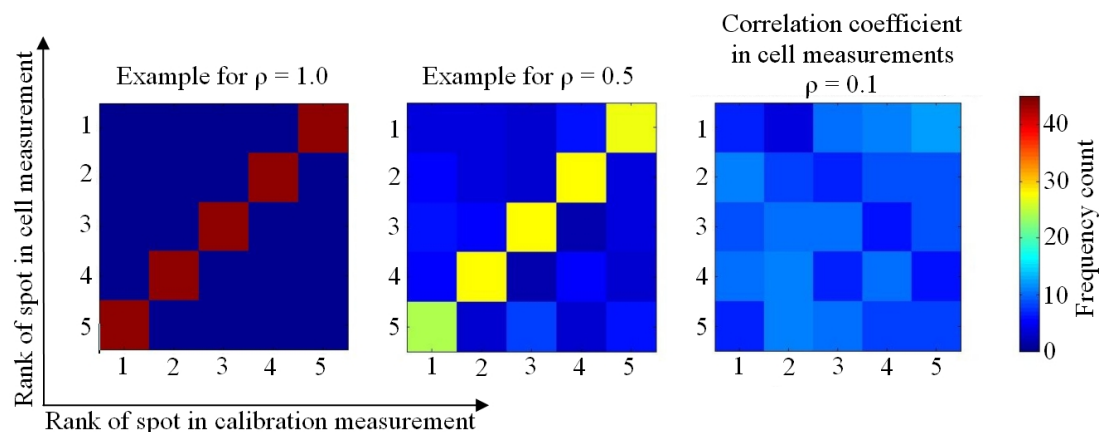


Figure 5.3.: Color maps depicting the relation between the diffusion time in a spot measured in cell measurements and in the corresponding calibration measurement in solution. The left color map is to show what a perfect correlation between the diffusion times would look like. The color map in the middle is an example for a dependence with a correlation coefficient of $\rho = 0.5$. The right color map shows that there is almost no correlation in the 44 measurements that have been analyzed.

5.2.4. Correlation between diffusion times measured in calibration and cell measurements

Even when a measurement in solution is corrected for crosstalk and background effects, the diffusion times measured in the five spots are usually slightly different (see section 2.6.2). It is interesting to verify whether the diffusion times measured in the calibration measurements in solution (before and after passing a culture dish) are correlated to the diffusion times measured in the cells. In order to check this possibility, the five spots were ranked according to their diffusion time in 44 measurements in HELA-eGFP cells and in the corresponding calibration measurement in solution. To find the degree of correlation between the two data sets, the Pearson product-moment coefficient ρ was calculated. ρ is defined as the ratio of the covariance of the two data sets to the product of their standard deviations. In order to visualize a potential correlation, the frequency of the encountered combination of ranks was depicted in a color map (figure 5.3). The left and middle color map illustrate what a perfect correlation and a dependence with a correlation coefficient of $\rho = 0.5$ would look like. The color map on the

right shows the frequency count of the encountered combination of ranks in the 44 measurements. There is almost no correlation between the rank of a spot in the calibration measurement and its rank in a measurement in cells. The correlation coefficient ρ yields 0.1. This shows that the intracellular variability of the diffusion time is clearly larger than a potential intrinsic variability in the spots and thus no additional correction is needed.

5.3. HSF1-eGFP in the heat shock response

5.3.1. General remarks

The dynamic behavior of the full length HSF1-eGFP in the heat shock response was studied in two different human cell lines: Human brain glioblastoma U87 and HELA cells. The results obtained with the two cell lines are in good agreement. Consequently, results presented in this section stem from the measurements in U87-HSF1-eGFP cells that were studied more extensively (674 autocorrelation functions (ACFs) in total). The results obtained on HELA-HSF1-eGFP cells (293 ACFs) will be presented in comparison to the experiments on HSF1 deletion mutants, which have been done exclusively on HELA cells.

Measurements in U87-HSF1-eGFP cells were conducted on 12 culture dishes according to the protocol described in section 5.1. The presence of nSBs, which manifest themselves as bright spots in the wide field image (see image 5.4 (b)), served as control for a successful heat shock. In the measuring campaign on U87-HSF1-eGFP cells, 330 ACF measured at $37^{\circ}C$ and 344 ACFs measured in heat-shocked cells at $43^{\circ}C$ were retained. Since HSF1-eGFP is nuclear, only spots located in the nucleus were taken into account. No spots were set in nSBs.

Autocorrelation functions were fitted with the diffusion-interaction model (equation 2.5), since a pure diffusion model did not give satisfactory results. In contrast to measurements in HELA-eGFP cells, more than 90% of the autocorrelation functions could be fitted properly with the diffusion-interaction model.

In contrast to the inactive eGFP molecule, the impact of the heat shock on the dynamics and concentration of HSF1-eGFP complexes is drastic. In order to

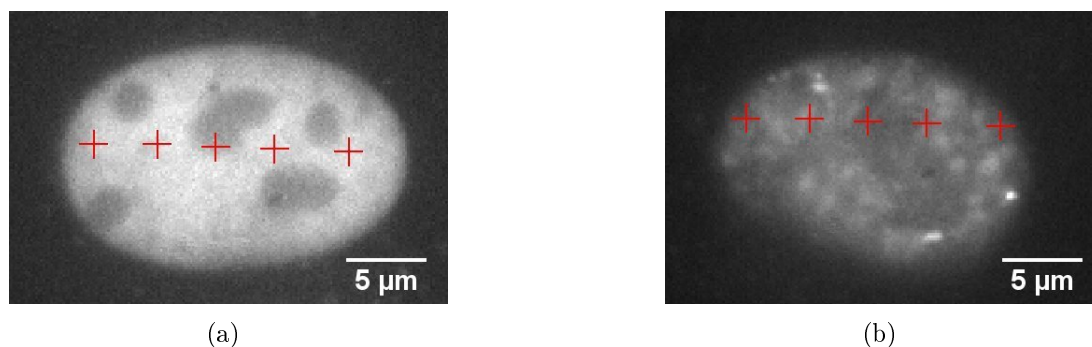


Figure 5.4.: An example for a wide field image of an U87-HSF1-eGFP cell in a non heat-shocked (a) and heat-shocked state (b) with the position of the five observation volumes. During heat shock nSBs are formed and can be seen as bright spots in the cell.

illustrate the effect, figure 5.5 shows the mean over a subset of 36 autocorrelation functions at 37°C (blue) and 31 autocorrelation functions at 43°C (red).

5.3.2. Changes in concentration and brightness of HSF1-eGFP

As exemplarily illustrated in figure 5.5 (a), the number of HSF1 complexes measured in heat-shocked cells is clearly lower than in non-heat-shocked cells. The mean value calculated over the whole set of data drops from 471 at 37°C to 233 at 43°C with a standard deviation of 209 and 155 respectively. Three processes may be responsible for this observation: Relocalization of HSF1-eGFP complexes in nSBs or binding to HSEs, trimerization of the HSF1-eGFP complexes and photobleaching.

At the same time the mean fluorescence intensity per spot decreases by a factor 2, which may in turn be attributed to the formation of nSBs and binding to HSEs, a drop in the molecular brightness of the eGFP molecule due to the temperature change and photobleaching effects. Since HSF1-eGFP is supposed to trimerize upon heat shock, one could expect a pronounced increase in the measured intensity per HSF1 complex. However, it practically stays unchanged between 37°C and 43°C . There are two possible explanations for this observation: Pho-

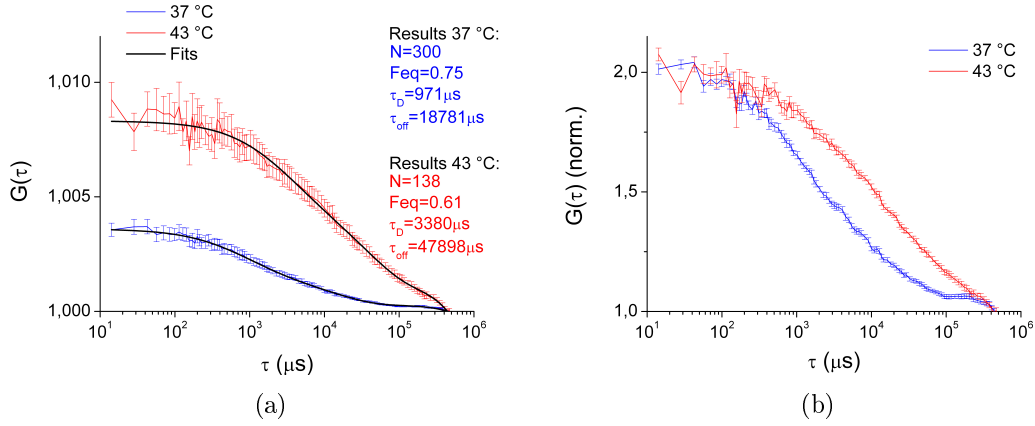


Figure 5.5.: Mean over a subset 36 autocorrelation functions at 37°C (blue) and 31 autocorrelation functions at 43°C (red) in U87-HSF1-eGFP cells (a). The mean over the same autocorrelation functions, normalized beforehand, in order to show the difference in the dynamics of the HSF1 complex (b).

photobleaching effects and the trimerization of HSF1-eGFP with endogenous HSF1. These findings are in contrast to measurements in HELA-eGFP cells, where the molecular brightness decreases about 20% (see section 5.2.2). Therefore, it stands to reason that some loss due to the temperature change and photobleaching is compensated by the gain in molecular brightness due to trimerization.

In order to clarify the role of photobleaching, relocalization in nSBs and binding to HSEs in the concentration drop, the mean normalized intensity in 45 spots was tracked over the two series of five acquisitions at 37°C and 43°C (black squares in figure 5.6). The same was done in 43 spots in HELA-eGFP cells for comparison (green squares).

In HELA-eGFP cells, the intensity decreases monotonously between the first and last acquisition at 37°C (no. 1 - no. 10) and between the first and last acquisition at 43°C (no. 11 - no. 20) due to photobleaching. The small drop between the last acquisition at 37°C (no. 10) and the first acquisition at 43°C (no. 11) can be explained by a decrease in brightness of the eGFP molecule due to the temperature change.

In U87-HSF1-eGFP cells in contrast, the intensity drop between the two temperatures is more pronounced and can be attributed to the relocalization of the

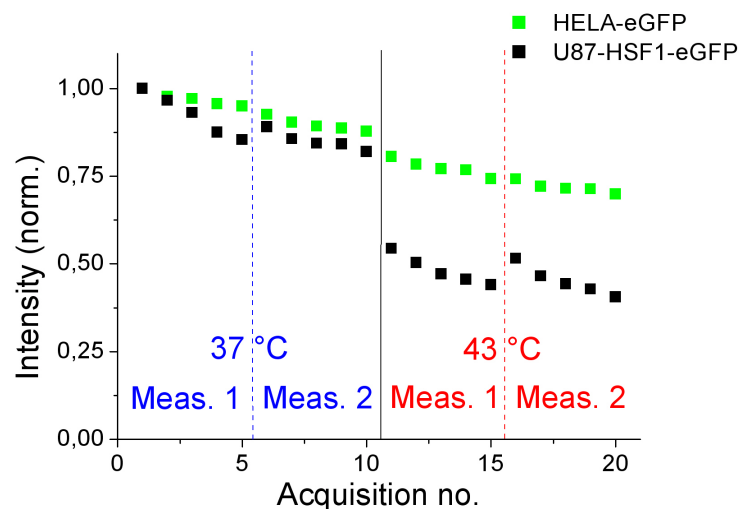


Figure 5.6.: Mean normalized intensity in 45 spots in the two series of five acquisitions at 37°C and at 43°C for U87-HSF1-eGFP cells (black squares) and for HELA-eGFP cells (green squares).

HSF1-eGFP complexes in nSBs and binding to HSEs. The photobleaching effects that become visible in the course of the acquisitions at 37°C and 43°C yield information about the mobility of the HSF1-eGFP complexes and will be discussed in the next paragraph.

5.3.3. Changes in the dynamics of HSF1-eGFP

Long time dynamics

In addition to the photobleaching effect that manifests itself as a monotonous decrease in the intensity during a measurement (figure 5.6), one observes a partial recovery of the intensity in between the measurements for HSF1-eGFP. The bleaching and the recovery is more pronounced for the measurements at 43°C . For the inactive eGFP in HELA cells this effect does not exist. There are two possible explanations: Firstly, there could be compartmentalization that locally confines the bleached HSF1-eGFP complexes. With the shift of the observation volume molecules in a new, prior unbleached compartment start to get photobleached. In order to explain the differences between the two temperatures, the

compartmentalization would have to be more pronounced at 43°C . Secondly, a weakly mobile species in U87-HSF1-eGFP cells could be photobleached locally. After the shift of the observation volumes in between the two measurements, one observes fresh, unbleached complexes that are bleached during the second measurement in turn. A more important fraction of the weakly mobile complexes at 43°C would explain the differences between the two temperatures. The lower bound for the residence time of these complexes can be estimated from the acquisition timing and would be about 1s. This time is too long to be accessible by FCS and could be exploited by FRAP measurements.

However, the heat shock also causes an important change in the dynamics that falls in the measuring range of FCS. In order to illustrate this fact, figure 5.5 (b) shows the mean over a subset of 36 autocorrelation functions at 37°C (blue) and 31 autocorrelation functions at 43°C (red) that have been normalized beforehand. It can be clearly seen that the dynamics of HSF1-eGFP is slowed down in heat-shocked cells.

Statistical analysis of the short time dynamics

Table 5.2 shows the fit parameters F_{eq} (the fraction of free complexes at equilibrium), τ_D and τ_{off} (the residence time) averaged over all 330 and 340 autocorrelation functions measured at 37°C and during heat shock at 43°C respectively. The parameters τ_D and τ_{off} feature large standard deviations, which reflect the broad dispersion of these values. Even so, all fit parameters are clearly affected by heat shock. A t-test on the parameters measured at 37°C and at 43°C shows a significant difference between the two temperatures. The fraction of free complexes F_{eq} is decreased upon heat shock, while the diffusion time τ_D and the residence time τ_{off} are increased. These results are not surprising, since HSF1 is supposed to be trimerized and interacting with DNA during heat shock.

In order to gain more insight into the dynamics of these interactions, the diffusion coefficient $D = \frac{\omega_r^2}{4D}$, the association rate $k_{on}^* = k_{off} \frac{1-F_{eq}}{F_{eq}}$ and the dissociation rate $k_{off} = \tau_{off}^{-1}$ have been calculated for every measurement. Because of the broad dispersion of the values, their median (and median absolute deviation (MAD)), which are expected to be more robust than the mean, will be considered in the

U87-HSF1-eGFP			
Parameter	Mean parameter \pm SD		p
	37°C (330 ACFs)	43°C (344 ACFs)	
F_{eq}	0.71 \pm 0.13	0.55 \pm 0.15	***
$\tau_D(\mu s)$	956 \pm 630	2788 \pm 2335	***
$\tau_{off}(\mu s)$	31971 \pm 47734	48638 \pm 48896	***
Parameter	Median parameter \pm MAD		p
	37°C (330 ACFs)	43°C (340 ACFs)	
$D(\mu m^2 s^{-1})$	18 \pm 7	7 \pm 4	***
$k_{on}^*(s^{-1})$	22 \pm 16	23 \pm 14	o
$k_{off}(s^{-1})$	65 \pm 33	30 \pm 15	***
Parameter	Mean variation coefficient \pm SD (43 cells)		p
	37°C	43°C	
VC_D	0.62 \pm 0.26	0.98 \pm 0.50	***
$VC_{k_{on}^*}$	0.88 \pm 0.30	0.93 \pm 0.41	o
$VC_{k_{off}}$	0.59 \pm 0.22	0.59 \pm 0.22	o

Table 5.2.: Mean F_{eq} , τ_D , τ_{off} , median D , k_{on}^* , k_{off} and variation coefficient for D , k_{on}^* and k_{off} for measurements in U87-HSF1-eGFP cells. Significance levels: ***: $p < 0.001$, **: $0.001 < p < 0.01$, *: $0.01 < p < 0.05$, o: $0.05 < p$

further analysis (see table 5.2).

For comparison, the corresponding values for measurements in HELA cells expressing inactive eGFP are given in table 5.3. As already deduced from the fits with a simple diffusion model, the dynamics of eGFP in the HELA cell is not affected by heat shock. $D_{HELA-eGFP}$ is larger than $D_{U87-HSF1-eGFP}$, which is, given the difference in size and shape of eGFP and HSF1-eGFP, not surprising. $D_{HELA-eGFP}$ calculated from the HELA-eGFP data fitted with the diffusion-interaction model is also larger than the values obtained by fitting with the simple diffusion model (section 5.2.2). This is expected since τ_{off} deviates a part of the behavior at long lag times. k_{off} measured in HELA-eGFP cells is much larger than k_{on}^* , which points towards a dynamics that is dominated by diffusion. This could explain why about 30 % of the HELA-eGFP data could not be properly fitted with the diffusion-interaction model.

The Stoke's radii of the inactive monomeric HSF1 and the active HSF1 trimer in heat-shocked cells have been determined by Sistonen et al. [101] in gel filtration

HELA-eGFP			
Parameter	Mean parameter \pm SD		p
	37°C (105 ACFs)	43°C (98 ACFs)	
F_{eq}	0.82 \pm 0.14	0.79 \pm 0.16	o
$\tau_D(\mu s)$	242 \pm 154	245 \pm 164	o
$\tau_{off}(\mu s)$	7009 \pm 7849	6001 \pm 5789	o
Parameter	Median parameter \pm MAD		p
	37°C (105 AC functions)	43°C (98 AC functions)	
$D(\mu m^2 s^{-1})$	315 \pm 139	337 \pm 137	o
$k_{on}^*(s^{-1})$	46 \pm 41	49 \pm 44	o
$k_{off}(s^{-1})$	247 \pm 160	237 \pm 135	o
Parameter	Mean variation coefficient \pm SD (15 cells)		p
	37°C	43°C	
VC_D	0.56 \pm 0.15	0.59 \pm 0.21	o
$VC_{k_{on}^*}$	1.33 \pm 0.33	1.42 \pm 0.44	o
$VC_{k_{off}}$	0.94 \pm 0.40	0.80 \pm 0.23	o

Table 5.3.: Mean F_{eq} , τ_D , τ_{off} , median D , k_{on}^* , k_{off} and variation coefficients for D , k_{on}^* and k_{off} for measurements in HELA-eGFP cells. Significance levels: ***: $p < 0.001$, **: $0.001 < p < 0.01$, *: $0.01 < p < 0.05$, o: $0.05 < p$

experiments and yield $4.5nm$ for the monomeric inactive form and $6.5nm$ for the active trimer. The diffusion constant for HSF1-eGFP can be calculated using these values and the cell viscosity derived from the measurements in HELA-eGFP cells. The latter depends on the diffusion constant of eGFP in the cell and the eGFP hydrodynamic radius of $(2.09 \pm 0.04)nm$, estimated in section 3.6. With $D_{HELA-eGFP} = (37 \pm 16)\mu m^2 s^{-1}$ (median value \pm MAD, found with the simple diffusion model in section 5.2.2), $D_{U87-HSF1-eGFP}$ should yield $(17 \pm 8)\mu m^2 s^{-1}$ and $(12 \pm 5)\mu m^2 s^{-1}$ at $37^\circ C$ and $43^\circ C$ respectively.

In the non-heat-shocked cells, the theoretical and measured value for $D_{U87-HSF1-eGFP}$ are in good agreement ($(17 \pm 8)\mu m^2 s^{-1}$ vs. $(18 \pm 7)\mu m^2 s^{-1}$). In the heat-shocked cells in contrast, the theoretical value of $(12 \pm 5)\mu m^2 s^{-1}$, which is solely based on the hydrodynamic radius of the active trimer, is larger than the measured diffusion constant of $(7 \pm 4)\mu m^2 s^{-1}$. The actual slowdown to $(7 \pm 4)\mu m^2 s^{-1}$ could indicate the presence of interactions in the heat-shocked cell that decelerate the diffusion but are not directly measurable by FCS. This is the case for dynamics

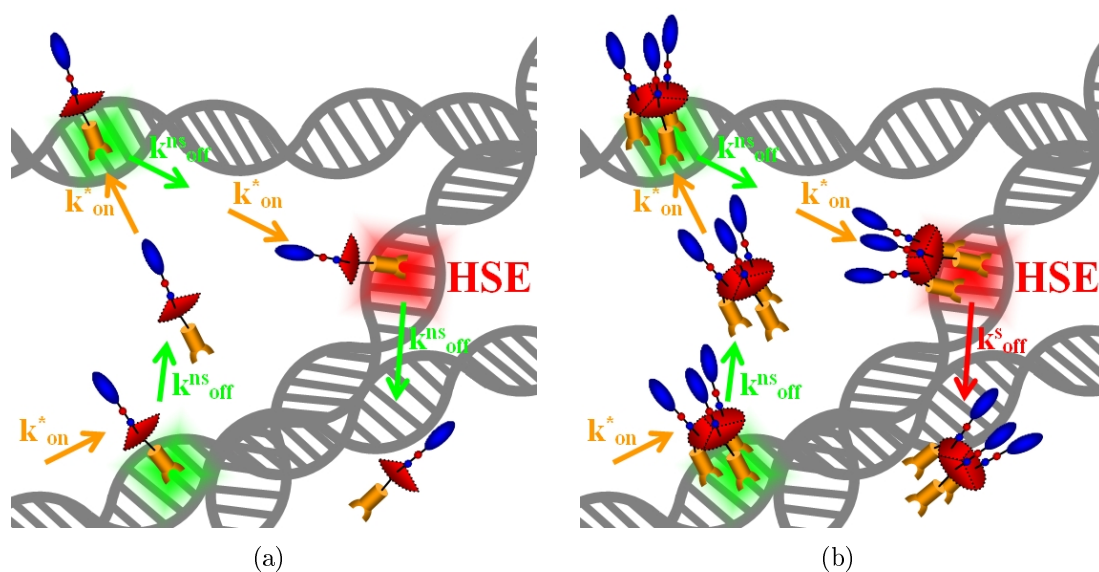


Figure 5.7.: Schematics illustrating the hypothetical diffusion and interaction of HSF1 with non-specific and specific binding sites [102–107]. In a non-heat-shocked state the inactive HSF1 monomer is non-specifically interacting with all binding sites with k_{on}^* and k_{off}^{ns} , no matter if they are specific (red) or non-specific (green) (a). Upon heat shock, the active HSF1 trimer is diffusing and interacting non-specifically with non-specific binding sites (k_{on}^* and k_{off}^{ns}) (green), but will bind with high affinity to encountered HSEs (red) with k_{on}^* and k_{off}^s (b).

on large time scales ($>1s$) the presence of which has been shortly discussed in section 5.3.3.

It has been suggested that the dynamics of a transcription factor is governed by diffusion through the nucleus and stochastic non-specific interactions, until it encounters a specific binding site [102–107]. It is thus possible that the measured k_{on}^* and k_{off} values at $37^\circ C$ are related to these non-specific interactions. Even though HSF1 is in an inactive monomeric state at $37^\circ C$ and not trimerized, which would be essential for high affinity binding to HSEs [84, 85], it is probably capable of non-specific binding. Figure 5.7(a) illustrates the diffusion and interaction of inactive HSF1 with non-specific binding sites (green). The unspecific k_{on}^* and k_{off} values are $(22 \pm 16)\mu m^2 s^{-1}$ and $(65 \pm 33)\mu m^2 s^{-1}$ respectively. If HSF1 encounters a specific binding site (red), it probably cannot bind to it with high affinity [84, 85] and the interaction stays purely unspecific.

When the cell suffers a heat shock and HSF1 is trimerized, the complex is still diffusing and interacting non-specifically with $k_{on}^* = (23 \pm 14) \mu m^2 s^{-1}$ (figure 5.7(b)), but as soon as it encounters a HSE, the interaction becomes specific and HSF1 binds with high affinity. The effect of this specific interaction on the dynamics is partly incorporated in D (as discussed above) as well as in k_{off} , which is significantly decreased upon heat shock and yields $(30 \pm 15) \mu m^2 s^{-1}$. Vukojević et al. [108] found a specific k_{off} value of $0.1 s^{-1}$ and non-specific k_{off} value of $325 s^{-1}$ for a synthetic Hox transcription factor by high resolution fluorescence imaging and FCS. These results support the hypothesis that our k_{off} incorporates both, specific and non-specific interactions, since it is in between the two values.

As k_{on}^* is twice as large for inert eGFP as for HSF1-eGFP, one could conclude that this constant is limited by the diffusion of the complex, which is much faster for eGFP than for HSF1-eGFP. But why is k_{on}^* for HSF1-GFP not changed by heat shock, since D is slowed down by HSF1 getting trimerized (to a theoretical value of $D = (12.0 \pm 0.5) \mu m^2 s^{-1}$)? A possible explanation is that the slowdown of the complex is counterbalanced by an increased number of free binding sites $[S]$, since $k_{on}^* = [S]k_{on}$.

Intracellular inhomogeneity of specific interactions

The number of HSEs in the genome is, compared to the number of unspecific binding sites, very limited [55, 102]. It is therefore interesting to study the spatial homogeneity of the parameters incorporating a part of the specific interactions of HSF1 within a given cell in a non-heat-shocked and heat-shocked state. Since the mFCS technique allows simultaneous measurements in different locations within the same cell, it is perfectly adapted to address this question .

In order to quantify the spatial variations of the parameters D , k_{on}^* and k_{off} , their variation coefficients (VCs)

$$VC = \frac{SD_{given\ cell}}{Mean_{given\ cell}} \quad (5.1)$$

were calculated for each cell at $37^\circ C$ and $43^\circ C$, where $SD_{given\ cell}$ is the standard deviation of the measured parameters in different spots within in a given cell and $Mean_{given\ cell}$ their mean value. Since we did for each temperature two

measurements with five spots in each cell, the VC was calculated from up to ten values. The mean VCs, averaged over the same 43 cells for both temperatures, are given in table 5.2. The same calculations were also done for 15 HELA-eGFP cells (see table 5.3). Since the measurements before and during heat shock were done in the same cells, a paired t-test was used in order to determine if the VCs are significantly different between $37^{\circ}C$ and $43^{\circ}C$.

In HELA-eGFP cells, the VC of none of the parameters changed upon heat shock, which was expected since none of the parameters is affected by the temperature change. The fact that the spatial homogeneity of the diffusion constant in a given cell does not change between $37^{\circ}C$ and $43^{\circ}C$ is a hint that the change in chromatin structure that goes along with heat shock (see section 5.2.3) does not lead to a larger inhomogeneity in the spatial diffusion of eGFP. Since the HSF1-eGFP complex is larger than the inert eGFP molecule, one cannot be sure that its diffusion is not influenced by the change in chromatin structure as well. However, measurements on a deletion mutant presented in the next section indicate that the structural change has no impact on the spatial homogeneity of the diffusion of the HSF1 complex.

For U87-HSF1-eGFP cells, the VC of the diffusion constant D (VC_D) is significantly increased upon heat shock. We believe that D measured during heat shock includes a part of specific interactions of HSF1-eGFP with a very limited number of HSE and that the change in chromatin structure does not cause a difference in the spatial homogeneity of the diffusion. Because of this the increased variability of D is likely to be caused by a spatially heterogeneous distribution of the HSEs. Accordingly, the VC of the parameter k_{on}^* ($VC_{k_{on}^*}$), which is not affected by heat shock, does not change between $37^{\circ}C$ and $43^{\circ}C$. However, it remains an open question why the VC of k_{off} ($VC_{k_{off}}$), which according to our hypothesis contains part of the specific interactions, does not change upon heat shock.

5.4. HSF1-eGFP deletion mutants in the heat shock response

In order to investigate the impact of the individual HSF1 domains on the dynamics of HSF1 at 37°C and upon heat shock at 43°C , mFCS experiments were done on the deletion mutants presented in section 4.2.2. For these measurements, the same statistical analysis as for U87-HSF1-eGFP cells was employed.

5.4.1. Control measurements in HELA-HSF1-eGFP and HELA-HSF1-eGFP siRNA cells

HSF1-eGFP dynamics was extensively studied in U87 cells. Additionally, experiments on full-length HSF1 were conducted in HELA cells, to get a reference for the measurements on HSF1 deletion mutants (exclusively done in HELA cells) within the same cell line. The corresponding results for HELA-HSF1-eGFP can be found in table 5.4. In order to clarify the characteristics of HSF1-K80Q-eGFP, endogenous HSF1 had to be silenced (see section 4.2.2). For comparison, the dynamics of full-length HSF1-eGFP was also measured in HELA cells with silenced endogenous HSF1, referred to as HELA-HSF1-eGFP siRNA. The results are given in table 5.5. As for U87-HSF1-eGFP, HELA-HSF1-eGFP and HELA-HSF1-eGFP siRNA are nuclear before and during heat shock and form nSBs in response to the stress. This can be seen in the exemplary wide field image of the corresponding cells before and during HS, given in figure 5.8(a) and (b).

Figure 5.9(a) and (b) show the mean autocorrelation functions (normalized beforehand) of HELA-HSF1-eGFP and HELA-HSF1-eGFP siRNA for 37°C (blue) and 43°C (red). Here as well no visible difference to the dynamics of U87-HSF1-eGFP can be found: The dynamics is slowed down and the number of complexes is decreased upon heat shock (data not shown), no matter whether endogenous HSF1 is silenced, or not.

As can be seen in table 5.4 and 5.5, the means of the three fit parameters F_{eq} , τ_D and τ_{off} are very similar to the ones discussed in the previous section for U87-HSF1-eGFP. They are clearly affected by heat shock, except for one case: The τ_{off} value of HELA-HSF1-eGFP siRNA. However, since the standard devia-

HELA-HSF1-eGFP

Parameter	Mean parameter \pm SD		p
	37°C (176 ACFs)	43°C (117 ACFs)	
F_{eq}	0.75 \pm 0.08	0.61 \pm 0.12	***
$\tau_D(\mu s)$	1188 \pm 447	2195 \pm 1499	***
$\tau_{off}(\mu s)$	33399 \pm 33940	48462 \pm 35591	***
Parameter	Median parameter \pm MAD		p
	37°C (176 ACFs)	43°C (117 ACFs)	
$D(\mu m^2 s^{-1})$	14 \pm 3	9 \pm 4	o
$k_{on}^*(s^{-1})$	16 \pm 8	17 \pm 8	o
$k_{off}(s^{-1})$	47 \pm 18	25 \pm 8	*
Parameter	Mean variation coefficient \pm SD (17 cells)		p
	37°C	43°C	
VC_D	0.44 \pm 0.23	0.70 \pm 0.40	*
$VC_{k_{on}^*}$	0.79 \pm 0.37	0.80 \pm 0.54	o
$VC_{k_{off}}$	0.53 \pm 0.18	0.60 \pm 0.47	o

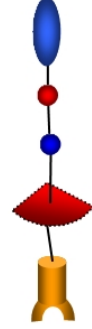
Table 5.4.: Mean F_{eq} , τ_D , τ_{off} , median D , k_{on}^* , k_{off} and variation coefficients for D , k_{on}^* and k_{off} for measurements in HELA-HSF1-eGFP cells. Significance levels: ***: $p < 0.001$, **: $0.001 < p < 0.01$, *: $0.01 < p < 0.05$, o: $0.05 < p$

tion of this parameter during heat shock is more than 5-fold the mean value, one could suppose that this mean value is not very well defined because of its broad dispersion.

Concerning the median values for D , k_{on}^* and k_{off} , HELA-HSF1-eGFP siRNA is similar to U87-HSF1-eGFP. HELA-HSF1-eGFP shows qualitatively the same behavior, but the values are globally somewhat smaller. Although p does not reach the significance level of 0.05 when D at 37°C and 43°C is compared, the value of 0.08 indicates a difference between the two groups.

The VCs of D are significantly increased upon heat shock for HELA-HSF1-eGFP and HELA-HSF1-eGFP siRNA and indicate a larger heterogeneity of diffusion and therefore a non-uniform distribution of HSEs throughout the genome as discussed for U87-HSF1-eGFP in the previous section. The VCs of the remaining two parameters do not change upon heat shock and are also comparable to the ones found for U87-HSF1-eGFP.

In conclusion it can be said that U87-HSF1-eGFP, HELA-HSF1-eGFP and HELA-



HELA-HSF1-eGFP siRNA			
Parameter	Mean parameter \pm SD		p
	37°C (138 ACFs)	43°C (120 ACFs)	
F_{eq}	0.71 \pm 0.11	0.56 \pm 0.15	***
$\tau_D(\mu s)$	965 \pm 604	3161 \pm 2388	***
$\tau_{off}(\mu s)$	22388 \pm 34013	185530 \pm 1172900	o
Parameter	Median parameter \pm MAD		p
	37°C (138 ACFs)	43°C (120 ACFs)	
$D(\mu m^2 s^{-1})$	19 \pm 8	6 \pm 2	***
$k_{on}^*(s^{-1})$	29 \pm 19	17 \pm 10	o
$k_{off}(s^{-1})$	76 \pm 36	19 \pm 7	***
Parameter	Mean variation coefficient \pm SD (14 cells)		p
	37°C	43°C	
VC_D	0.49 \pm 0.24	0.90 \pm 0.34	**
$VC_{k_{on}^*}$	1.00 \pm 0.41	1.07 \pm 0.53	o
$VC_{k_{off}}$	0.54 \pm 0.16	0.63 \pm 0.26	o

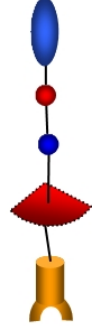
Table 5.5.: Mean F_{eq} , τ_D , τ_{off} , median D , k_{on}^* , k_{off} and variation coefficients for D , k_{on}^* and k_{off} for measurements in HELA-HSF1-eGFP siRNA cells. Significance levels: ***: $p < 0.001$, **: $0.001 < p < 0.01$, *: $0.01 < p < 0.05$, o: $0.05 < p$

HSF1-eGFP siRNA show similar dynamics, even if the changes upon heat shock are less pronounced for HELA-HSF1-eGFP. The analysis and discussion on the dynamics of HSF1-eGFP based on measurements in U87 cells given in the previous section apply therefore also for HSF1-eGFP dynamics in HELA cells.

5.4.2. HELA-HSF1- Δ Trim-eGFP

It has been shown that the formation of HSF1 trimers is needed to bind to DNA with high affinity [84, 85]. It is therefore interesting to investigate the effects that deletion of the trimerization domain has on the HSF1 dynamics and to check if they are consistent with the hypothesis proposed in the previous section.

In contrast to HSF1-eGFP, HSF1- Δ Trim-eGFP is not only found in the nucleus, but also in the cytoplasm. In addition, it does not form nSBs in response to thermal stress as can be seen in the wide field image 5.8(c). The comparison of the mean normalized autocorrelation functions measured at 37°C and 42°C



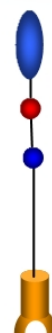
does not show any difference in the dynamics before and during heat shock (see figure 5.9(c)). In contrast, the detailed statistical analysis of the fit parameters reveals some subtleties.

HELA-HSF1- Δ Trim-eGFP

Parameter	Mean parameter \pm SD		p
	37°C (132 ACFs)	43°C (132 ACFs)	
F_{eq}	0.80 \pm 0.12	0.76 \pm 0.14	*
$\tau_D(\mu s)$	855 \pm 359	1001 \pm 806	o
$\tau_{off}(\mu s)$	21418 \pm 36058	28611 \pm 56075	o
Parameter	Median parameter \pm MAD		p
	37°C (132 ACFs)	43°C (132 ACFs)	
$D(\mu m^2 s^{-1})$	19 \pm 5	18 \pm 6	o
$k_{on}^*(s^{-1})$	20 \pm 15	19 \pm 13	o
$k_{off}(s^{-1})$	90 \pm 39	72 \pm 35	**
Parameter	Mean variation coefficient \pm SD (20 cells)		p
	37°C	43°C	
VC_D	0.45 \pm 0.25	0.59 \pm 0.30	o
$VC_{k_{on}^*}$	0.93 \pm 0.42	1.18 \pm 0.43	*
$VC_{k_{off}}$	0.56 \pm 0.28	0.58 \pm 0.19	o

Table 5.6.: Mean F_{eq} , τ_D , τ_{off} , median D , k_{on}^* , k_{off} and variation coefficients for D , k_{on}^* and k_{off} for measurements in HELA-HSF1- Δ Trim-eGFP cells. Significance levels: ***: $p < 0.001$, **: $0.001 < p < 0.01$, *: $0.01 < p < 0.05$, o: $0.05 < p$

A first difference between HSF1- Δ Trim-eGFP and HSF1-eGFP is that the fraction of free complexes F_{eq} before and after heat shock is larger for the deletion mutant. The values are closer to the ones found for the inert eGFP molecule than to the ones found for HSF1-eGFP. Interestingly, F_{eq} is slightly decreased by heat shock, which could indicate an increase in non-specific interactions with increasing temperature. However, even at 43°C, F_{eq} is always larger for HSF1- Δ Trim-eGFP than for HSF1-eGFP. τ_D and τ_{off} do not change upon heat shock, and neither do the median values for D and k_{on}^* , which are similar to the values found for HSF1-eGFP in the inactive state before heat shock. The k_{off} value for HSF1- Δ Trim-eGFP before and during heat shock is clearly larger than for HSF1-eGFP but decreases upon heat shock. These results indicate that the Trim



domain is in fact essential for specific binding to HSEs, since D does not change and k_{off} is always larger than the k_{off} in non-shocked HSF1-eGFP cells. If there would be specific binding as in the case of HSF1-eGFP, it would be partially taken into account in these two parameters. The large k_{off} values furthermore suggest that the Trim domain is also involved in the unspecific binding of the HSF1 monomer, but that the increased temperature facilitates the binding, since k_{off} decreases upon heat shock. Consistently with the absence of specific binding during heat shock, the homogeneity (the VCs) of D and k_{off} do not change significantly. Why the homogeneity of k_{on}^* , which itself does not change between $37^\circ C$ and $43^\circ C$, is affected by heat shock is not clear.

Since the variability of D does not significantly change upon heat shock, the findings on the HSF1- Δ Trim-eGFP deletion mutant support the hypothesis that the structural change in chromatin has no impact on the spatial homogeneity of the HSF1 diffusion.

5.4.3. HELA-HSF1-K80Q-eGFP and - HELA-HSF1-K80Q-eGFP siRNA

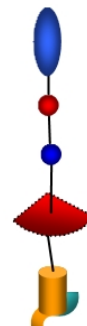
In the HELA-HSF1-K80Q-eGFP deletion mutant, the lysine K80 in the DBD domain has been replaced by glutamine. With this mutation, HSF1 should still be able to trimerize, but should not be able to bind to DNA [91]. HSF1-K80Q-eGFP is nuclear and does not form nSBs during heat shock as can be seen in the wide field image 5.8(d). The mean normalized autocorrelation functions for measurements at $37^\circ C$ and $42^\circ C$, shown in figure 5.9(d), reveal a clear difference in the dynamics before and during heat shock. The results of the statistical analysis of the individual fit parameters for HELA-HSF1-K80Q-eGFP (table 5.7) are not different from the results obtained for the full-length HSF1-eGFP, except for the diffusion, which is somewhat slower than for full-HSF1-eGFP.

A plausible explanation for this findings would be that HSF1-K80Q-eGFP trimerizes with endogenous HSF1 and could thus nevertheless still be bound to DNA during heat shock. In contrast, it has been argued that HSF1 needs to be trimerized in order to bind specifically to HSEs [84, 85]. If one of the HSF1s in the

HELA-HSF1-K80Q-eGFP

Parameter	Mean parameter \pm SD		p
	37°C (136 ACFs)	43°C (131 ACFs)	
F_{eq}	0.70 \pm 0.10	0.62 \pm 0.12	***
τ_D (μs)	1561 \pm 752	2805 \pm 1772	***
τ_{off} (μs)	30028 \pm 21766	49567 \pm 59764	***
Parameter	Median parameter \pm MAD		p
	37°C (136 ACFs)	43°C (131 ACFs)	
D ($\mu m^2 s^{-1}$)	11 \pm 3	7 \pm 2	***
k_{on}^* (s^{-1})	19 \pm 10	18 \pm 10	o
k_{off} (s^{-1})	44 \pm 17	27 \pm 10	***
Parameter	Mean variation coefficient \pm SD (17 cells)		p
	37°C	43°C	
VC_D	0.40 \pm 0.16	0.72 \pm 0.37	**
$VC_{k_{on}^*}$	0.73 \pm 0.19	0.79 \pm 0.34	o
$VC_{k_{off}}$	0.44 \pm 0.1	0.44 \pm 0.18	o

Table 5.7.: Mean F_{eq} , τ_D , τ_{off} , median D , k_{on}^* , k_{off} and variation coefficients for D , k_{on}^* and k_{off} for measurements in HELA-HSF1-K80Q-eGFP cells. Significance levels: ***: $p < 0.001$, **: $0.001 < p < 0.01$, *: $0.01 < p < 0.05$, o: $0.05 < p$



trimer has no DNA binding ability, such a complex should bind with a lower affinity to HSEs, than a trimer composed of three full-length HSF1s.

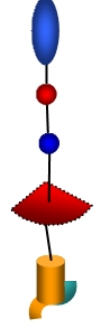
In order to clarify the role of endogenous HSF1 in the HELA-HSF1-K80Q-eGFP cell, it was silenced (HELA-HSF1-K80Q-eGFP siRNA). The silencing of the endogenous HSF1 does of course not change the fact that the mutant is nuclear and does not form nSBs upon heat shock (image 5.8(e)). The mean normalized autocorrelation function at 37°C and 42°C still shows differences in the HSF1-K80Q-eGFP dynamics before and after heat shock (figure 5.9(e)), which is further investigated in the statistical analysis (see table 5.8).

The fit parameters F_{eq} and τ_D are significantly changed by heat shock. In the case of τ_{off} , the t-test yields a p-value of 0.057, which is just above the significance level. The median diffusion constant D at 37°C is, as in measurements without siRNA, lower than for the full-length HSF1 and it decreases upon heat shock. However, the decrease is not significant, which is quite astonishing, considering the median values and the autocorrelation functions in figure 5.9(e). In con-

5.4. HSF1-eGFP deletion mutants in the heat shock response

HELA-HSF1-K80Q-eGFP siRNA			
Parameter	Mean parameter \pm SD		p
	37°C (149 ACFs)	43°C (146 ACFs)	
F_{eq}	0.67 \pm 0.11	0.54 \pm 0.13	***
$\tau_D(\mu s)$	1610 \pm 757	2623 \pm 1643	***
$\tau_{off}(\mu s)$	37153 \pm 57521	47902 \pm 36403	o
Parameter	Median parameter \pm MAD		p
	37°C (149 ACFs)	43°C (146 ACFs)	
$D(\mu m^2 s^{-1})$	11 \pm 3	7 \pm 3	o
$k_{on}^*(s^{-1})$	19 \pm 11	22 \pm 14	**
$k_{off}(s^{-1})$	40 \pm 15	26 \pm 10	***
Parameter	Mean variation coefficient \pm SD (16 cells)		p
	37°C	43°C	
VC_D	0.44 \pm 0.23	0.90 \pm 0.39	***
$VC_{k_{on}^*}$	0.63 \pm 0.19	0.84 \pm 0.35	*
$VC_{k_{off}}$	0.40 \pm 0.13	0.53 \pm 0.18	o

Table 5.8.: Mean F_{eq} , τ_D , τ_{off} , median D , k_{on}^* , k_{off} and variation coefficients for D , k_{on}^* and k_{off} for measurements in HELA-HSF1-K80Q-eGFP siRNA cells. Significance levels: ***: $p < 0.001$, **: $0.001 < p < 0.01$, *: $0.01 < p < 0.05$, o: $0.05 < p$



trast, the spatial inhomogeneity (the VC) of D is clearly increased by heat shock and indicates that this factor incorporates, even with the K80 mutation, specific binding on heterogeneously distributed HSEs. The median k_{off} value before and during heat shock is practically the same as for full-length HSF1. Interestingly, the median k_{on}^* value does increase upon heat shock, which could be related to an increase of spatial inhomogeneity of this factor during heat shock. In conclusion, it can be said that even if HSF1-K80Q-eGFP should theoretically be deprived of its DNA binding ability, it shows nonspecific and, after heat shock, specific interactions. In contrast, it does not form nSBs during heat shock. The silencing of endogenous HSF1 in the cell has no influence on the HSF1-K80Q-eGFP dynamics.

5.4.4. HELA-HSF1- Δ DBD-eGFP

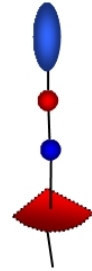
Since the mutation of lysine K80 in the DBD domain does not seem to keep HSF1 from binding DNA specifically and non-specifically, the next step is to query the role of the whole DNA binding domain. As HSF1-K80Q-eGFP, HSF1- Δ DBD-eGFP is nuclear and no formation of nSBs could be observed during heat shock (see figure 5.8(f)). For this deletion mutant too, the mean normalized autocorrelation functions for HSF1- Δ DBD-eGFP show a clear difference between the dynamics in the heat-shocked and non-heat-shocked cell (see figure 5.9(f)).

HELA-HSF1- Δ DBD-eGFP

Parameter	Mean parameter \pm SD		p
	37°C (113 ACFs)	43°C (87 ACFs)	
F_{eq}	0.73 ± 0.13	0.67 ± 0.15	**
$\tau_D(\mu s)$	1227 ± 1119	2453 ± 1597	***
$\tau_{off}(\mu s)$	27082 ± 59804	55777 ± 77421	**
Parameter	Median parameter \pm MAD		p
	37°C (113 ACFs)	43°C (87 ACFs)	
$D(\mu m^2 s^{-1})$	18 ± 10	8 ± 4	***
$k_{on}^*(s^{-1})$	28 ± 20	15 ± 11	**
$k_{off}(s^{-1})$	81 ± 32	32 ± 15	***
Parameter	Mean variation coefficient \pm SD (17 cells)		p
	37°C	43°C	
VC_D	0.70 ± 0.20	0.82 ± 0.54	o
$VC_{k_{on}^*}$	0.97 ± 0.34	0.95 ± 0.38	o
$VC_{k_{off}}$	0.57 ± 0.29	0.50 ± 0.26	o

Table 5.9.: Mean F_{eq} , τ_D , τ_{off} , median D , k_{on}^* , k_{off} and variation coefficients for D , k_{on}^* and k_{off} for measurements in HELA-HSF1- Δ DBD-eGFP cells. Significance levels: ***: $p < 0.001$, **: $0.001 < p < 0.01$, *: $0.01 < p < 0.05$, o: $0.05 < p$

The statistical analysis of the individual fit parameters shows that even here F_{eq} , τ_D and τ_{off} are quite similar to the values measured for full-length HSF1. Moreover, all three parameters are significantly changed by the heat shock. The same holds for the median D . In the non-shocked cell, k_{on}^* and k_{off} are larger than for full-length HSF1, which could indicate more transient non-specific interactions. The k_{on}^* for HSF1- Δ DBD-eGFP is slightly smaller in the heat-shocked



cell than for full-length HSF1 whereas k_{off} has the same value. While all three parameters, D , k_{on}^* and k_{off} change during heat shock, their spatial homogeneity does not change. Since D and k_{off} , the two values incorporating a part of the specific interactions during heat shock, are comparable to the ones found for full-length HSF1, one would expect D to show a more pronounced spatial variability at $43^\circ C$. The mean VC_D is larger after than during heat shock (0.82 ± 0.54 vs. 0.70 ± 0.20), though the difference is not significant. It is worthwhile to mention that trimerization with endogenous HSF1 and thus indirect binding to DNA upon heat shock cannot be excluded, since endogenous HSF1 has not been silenced. As discussed for HSF1-K80Q-eGFP, the affinity for specific binding sites should, compared to full-length HSF1, be reduced, since at most two functional DBD domains are available in the trimer. The k_{on}^* constant after heat-shock, which is smaller than the one for full-length HSF1, supports this assumption. In contrast, k_{off} , which has the same value during heat shock as full-length HSF1, contradicts this hypothesis.

5.4.5. HELA-HSF1- Δ AD2-eGFP siRNA

The HSF1- Δ AD2-eGFP mutant was studied in order to investigate if the trans-activation domain influences the dynamics of HSF1. With a deleted AD2 domain, HSF1 should not be able to interact with other proteins involved in the transcription process (as for example coactivators [109, 110] or chromatin remodelers [69, 111]), which could slow down the dynamics of HSF1. An intriguing question is whether some of these proteins are assisting HSF1 in DNA binding.

In contrast to all other deletion mutants discussed, HSF1- Δ AD2-eGFP forms nSBs in response to thermal stress (see figure 5.8(g)). The mean normalized autocorrelation functions (figure 5.9(g)) show distinct dynamics at $37^\circ C$ and $43^\circ C$. These findings indicate that the AD2 subdomain is at least not substantially involved in the dynamics change of HSF1 during heat shock.

The detailed analysis shows that the fraction of free complexes does, in contrast to the other two fit parameters, not change upon heat shock. The median diffusion constant before heat shock is clearly larger than for full length HSF1. The k_{on}^* constant, which is assumed to be limited by diffusion, is at $37^\circ C$ also slightly

HELA-HSF1- Δ AD2-eGFP

Parameter	Mean parameter \pm SD		p
	37°C (123 ACFs)	43°C (84 ACFs)	
F_{eq}	0.75 \pm 0.16	0.72 \pm 0.12	o
τ_D (μ s)	798 \pm 639	1663 \pm 839	***
τ_{off} (μ s)	23764 \pm 43506	35729 \pm 39687	*
Parameter	Median parameter \pm MAD		p
	37°C (123 ACFs)	43°C (84 ACFs)	
D (μ m ² s ⁻¹)	25 \pm 12	10 \pm 2	***
k_{on}^* (s ⁻¹)	24 \pm 21	18 \pm 14	*
k_{off} (s ⁻¹)	97 \pm 62	53 \pm 25	***
Parameter	Mean variation coefficient \pm SD (9 cells)		p
	37°C	43°C	
VC_D	0.62 \pm 0.28	0.67 \pm 0.46	o
$VC_{k_{on}^*}$	1.24 \pm 0.44	0.80 \pm 0.50	**
$VC_{k_{off}}$	0.71 \pm 0.18	0.52 \pm 0.24	*

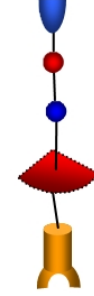


Table 5.10.: Mean F_{eq} , τ_D , τ_{off} , median D , k_{on}^* , k_{off} and variation coefficients for D , k_{on}^* and k_{off} for measurements in HELA-HSF1- Δ AD2-eGFP siRNA cells. Significance levels: ***: $p < 0.001$, **: $0.001 < p < 0.01$, *: $0.01 < p < 0.05$, o: $0.05 < p$

increased compared to the one measured for full length HSF1. This could indicate a slowdown of HSF1 dynamics by proteins binding to the AD2 domain and thus increasing the hydrodynamic radius of full-length HSF1. In the heat-shocked state the diffusion constant and the k_{on}^* value are closer to the ones of full length HSF1, in contrast to k_{off} , which is always larger. Since D and k_{off} do significantly change upon heat shock, but dissociation events are more frequent than for HSF1-eGFP, proteins binding to the AD2 domain might have the function to stabilize the HSF1-DNA bond.

The spatial homogeneity of D , k_{on}^* and k_{off} raises some questions. D incorporating specific interactions with a limited number of HSEs should be less homogeneous at 43°C than at 37°C. In addition, the behavior of the VC for k_{on}^* and k_{off} , which show less variability after heat shock, cannot be explained and should be the subject of further investigations.

5.4.6. Overview over the dynamic properties of HSF1 and the deletion mutants

The basic findings about HSF1 and the deletion mutants are summarized in table 5.11. HSF1-full length eGFP is believed to interact non-specifically with DNA before and during heat shock. There is some evidence that additionally specific binding events occur during heat shock: The measured diffusion constant $D_{meas}^{43^\circ C}$ at $43^\circ C$ is smaller than the value calculated from the hydrodynamic radius of the complex $D_{calc}^{43^\circ C}$ and is thus probably incorporating a part of specific interactions that happen on long time scales. The non-specific binding sites seem to be rare (as stated by Trinklein et al. [55]) and heterogeneously distributed throughout the nucleus, since the variation coefficient of D at $37^\circ C$ ($VC_D^{37^\circ C}$) is significantly smaller than its value at $43^\circ C$ ($VC_D^{43^\circ C}$).

Consistently with prior observations [84, 85], we found that the trimerization of HSF1 is essential for specific DNA binding. In addition, the HSF1- Δ Trim-eGFP deletion mutant does not form nSBs upon heat shock.

Contrary to what could be expected, a mutated or removed DBD domain that inhibits the formation of nSBs, does not seem to be essential for specific binding to DNA.

The AD2 domain is probably not directly involved in the formation of nSBs and specific binding events.

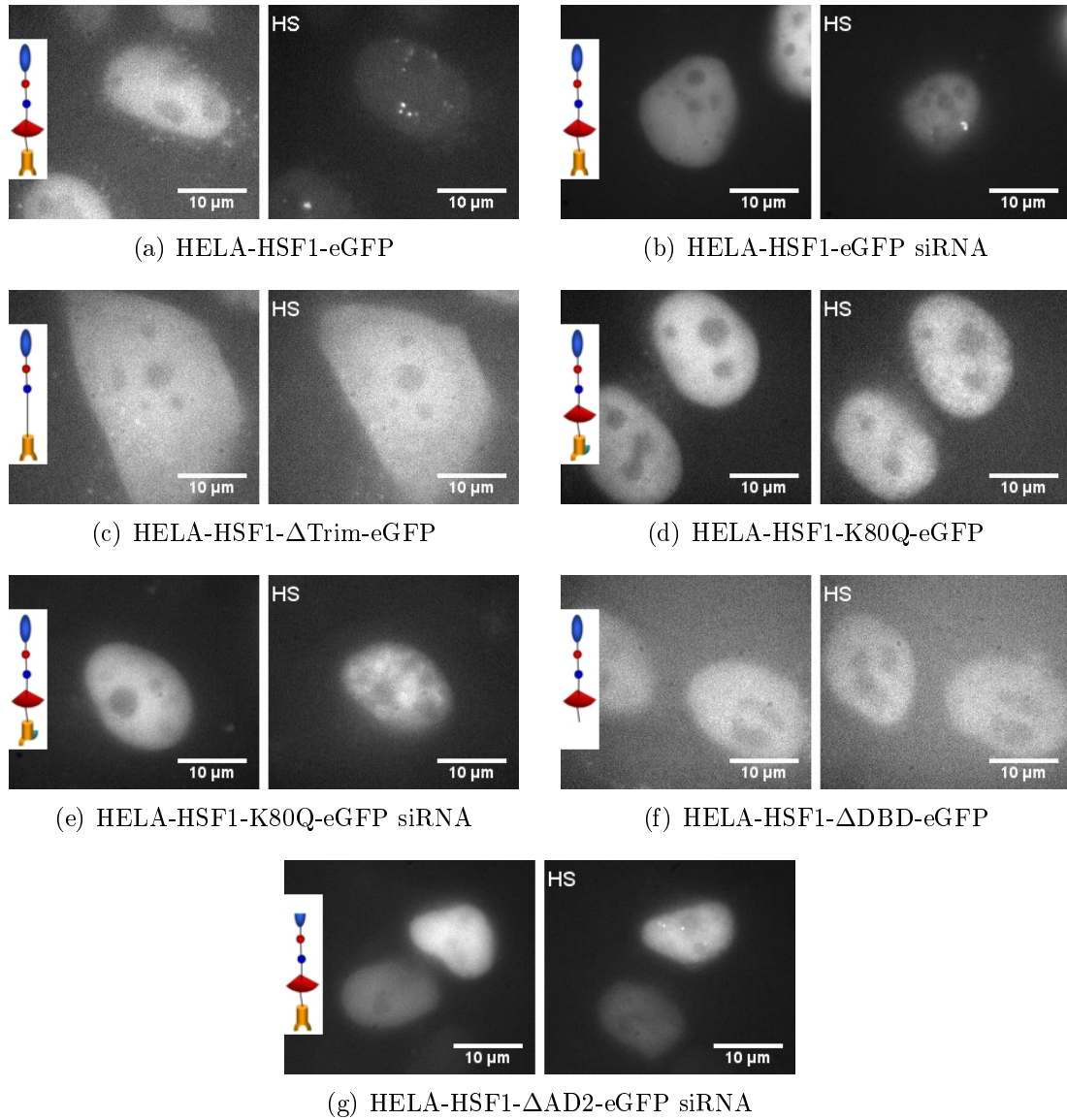


Figure 5.8.: Wide field images of a HELA cell expressing the full-length or mutated HSF1-eGFP before and during heat shock (HS).

5.4. HSF1-eGFP deletion mutants in the heat shock response

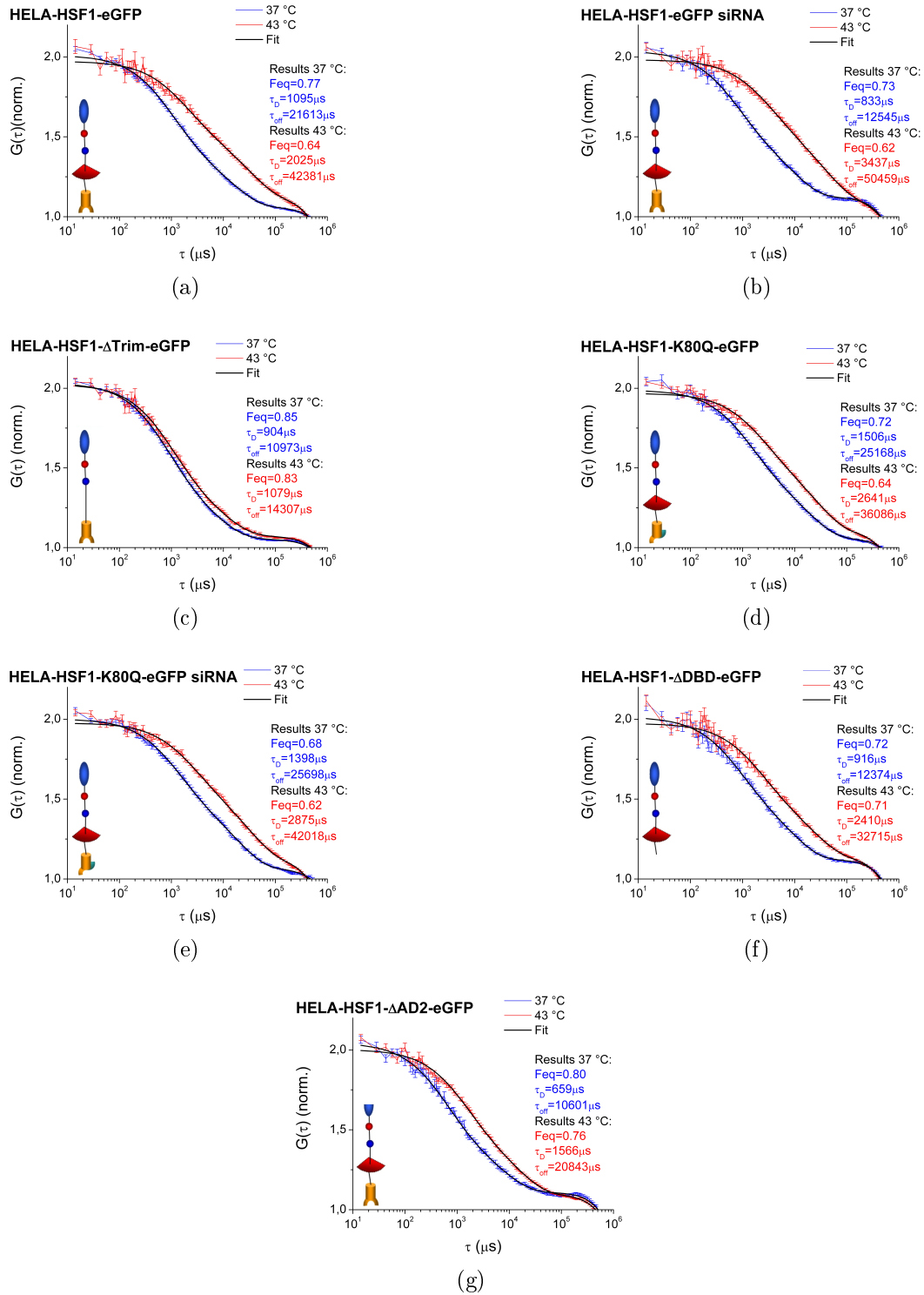


Figure 5.9.: Mean autocorrelation functions for the measurements in HELA cells expressing the full-length or mutated HSF1-eGFP. Errors are standard errors of the mean.

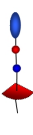
HSF1 deletion mutant	Formation of nSBs upon heat shock	Slowdown of dynamics upon heat shock	Evidence for specific binding to HSEs upon heat shock	Main interpretation
 HSF1-full-length-eGFP	yes	yes	$D_{meas}^{43^\circ C} < D_{calc}^{43^\circ C}$ $VC_D^{37^\circ C} < VC_D^{43^\circ C}$ significantly	Non-specific and upon heat shock additional specific interactions with DNA
 HSF1- Δ Trim-eGFP	no	no	no	Trimerization is essential for specific interactions with DNA
 HSF1-K80Q-eGFP	no	yes	yes	Mutated DBD domain does not inhibit specific interactions with DNA, but the formation of nSBs
 HSF1- Δ DBD-eGFP	no	yes	yes	DBD domain is likely not to be essential for specific binding to DNA, but for the formation of nSBs
 HSF1- Δ AD2-eGFP	yes	yes	no	AD2 domain is likely not to be essential for specific binding and the formation of nSBs

Table 5.11.: Overview over the main results of the statistical analysis for HSF1 and the deletion mutants. Two criteria were considered as evidence for the occurrence of specific binding to HSEs upon heat shock: Firstly, the measured diffusion constant $D_{meas}^{43^\circ C}$ at $43^\circ C$ is smaller than the value calculated from the hydrodynamic radius of the complex $D_{calc}^{43^\circ C}$. Secondly, the variation coefficient of D at $37^\circ C$ ($VC_D^{37^\circ C}$) is significantly smaller than its value at $43^\circ C$ ($VC_D^{43^\circ C}$), which means that the spatial inhomogeneity of D is increased upon heat shock.

6. mFCS experiments with a CMOS-SPAD detector

6.1. The CMOS-SPAD camera as detector for mFCS

A CMOS-SPAD detector developed by our collaborators at the University of Edinburgh (CMOS sensors & systems group) in the European Megaframe project was tested as detector for mFCS. This detector consists of an array of 32×32 single photon avalanche diodes (SPADs), which is implemented in a CMOS imaging process [112].

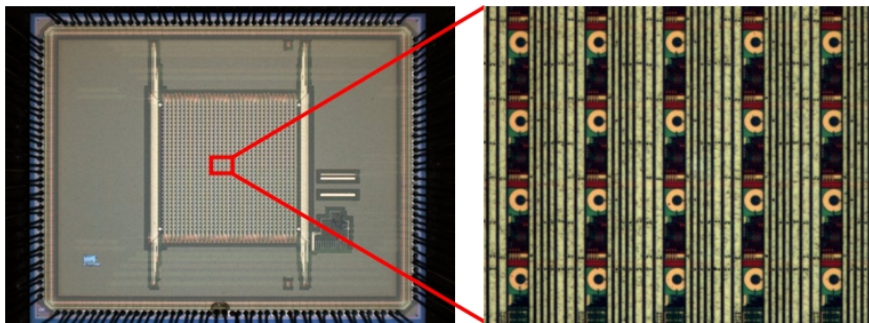


Figure 6.1.: CMOS-SPAD detector consisting of 32×32 single photon avalanche diodes and a sub-image of 4×5 SPADs. Pictures by courtesy of David Tyndall, CMOS Sensors & Systems Group, University of Edinburgh.

In contrast to CCD cameras, the digital parallel readout can achieve a rate of 500kHz, allowing mFCS measurements with a time resolution of $2\mu\text{s}$. The SPADs have a dead time of approximately 50ns and their active area has a diameter of $6.7\mu\text{m}$ [113]. The pixel pitch of $50\mu\text{m}$ results in a minimal spot distance of $3.8\mu\text{m}$

in the microscope object plane, which limits the number of spots that may be placed in one cell. The reverse breakdown voltage of the SPADs is -13.4V and it is operated at an excess bias voltage of 1.2V [114, 115].

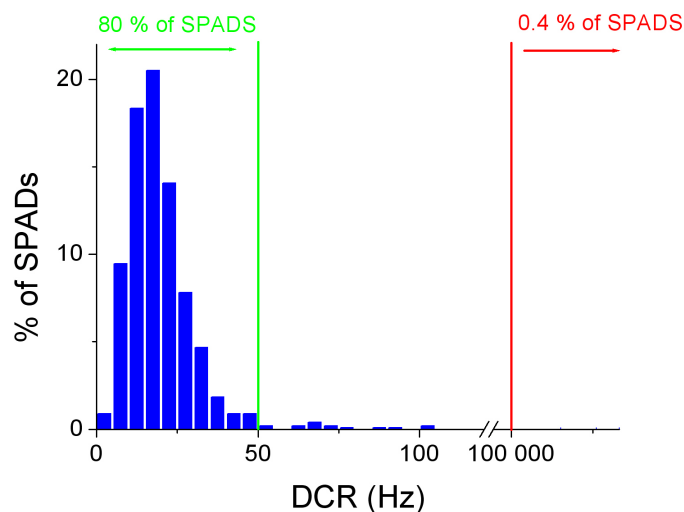


Figure 6.2.: Distribution of the dark count rates (DCRs) of the 32×32 SPADs. 80% of the SPADs have a DCR lower than 50Hz.

Figure 6.2 shows the distribution of the dark count rates (DCRs) measured on the 32×32 SPADs of our chip. 80% of them feature a DCR that is lower than 50Hz. In rare cases (0.4%), a DCR of more than 100 kHz can be found. Since a high DCR would deteriorate the signal, all measurements if not specified otherwise were done on SPADs that have a DCR of less than 50Hz.

At the moment a drawback is still that the data flow, which is transmitted via USB, is limited by the USB bandwidth.

6.2. Data acquisition

As for measurements with the EMCCD camera, the spherical wave and superposition approach (see section 2.2 , [59]) was used to calculate the phase map applied to the SLM in order to get the wanted spot configuration. The SLM and the CMOS-SPAD detector were piloted via a Java application [113] which allows an automatic alignment of the desired spots on the SPADs. The alignment

process is described in detail in [113].

Each FCS acquisition takes 10s and, in order to determine the standard errors, a series of five consecutive acquisitions is recorded in every measurement. In the measurements presented in the following, a 3×3 array of spots was used.

6.3. Data processing

6.3.1. Calculation of the autocorrelation function

The acquired time traces were treated in MATLAB. In contrast to measurements with the EMCCD camera, it is not necessary to do an offset correction when detecting on the CMOS-SPAD array because of the low DCRs. Furthermore, no correction for drift effects was done. For each acquisition, an autocorrelation function was calculated and corrected for crosstalk and background effects as will be discussed in section 6.3.2. The five consecutive acquisitions in one measurement result in five autocorrelation functions, which are averaged to yield one mean autocorrelation function with standard errors of the mean.

Fits were performed in Origin, using the fit models described in section 2.6.3 and applying an instrumental weighting. In the fitting range of $2\mu s$ to $800ms$, triplet relaxation had not to be taken into account.

6.3.2. Correction for crosstalk and background effects

Figure 6.3 shows the intensity profile of the 3×3 spots measured on the CCD camera. Due to the rigid symmetry and the large pixel pitch of the CMOS-SPAD detector, the spots have to be placed on adjacent pixels and are thus regularly spaced with a distance of $3.8\mu m$. As it has already been shown in measurements done on the EMCCD camera (see section 2.6.2), the spots have a Lorentzian shape with side wings that extend to larger distances. Therefore, the signal measured on a given SPAD includes not only the intensity fluctuations in the corresponding observation volume, but also side wing contributions from neighboring spots. These side wing contributions appear as uncorrelated photons in the measurement and artificially increase the estimated number of molecules. A

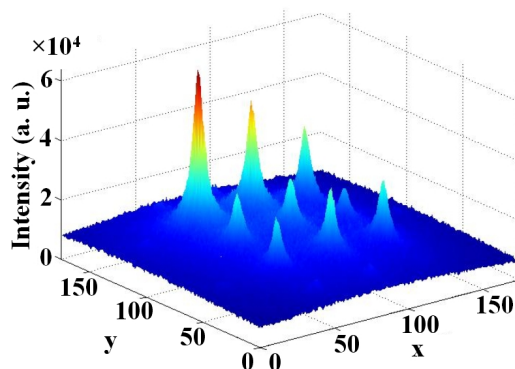


Figure 6.3.: Surface plot of the intensity distribution (recorded with the CCD camera) in and in the vicinity of the 3×3 spots.

constant background has to be added to the Lorentzians in order to model the intensity profile not only near the maxima, but also in between the spots. This constant background occurs due to non-diffracted light reflected by the SLM.

Since the spot intensities are not uniform, the spots are not influenced in the same way by these effects. The consequences are even more important than for measurements with the EMCCD camera, since spots are not only placed on one line, but in two dimensions. In addition, the regular spacing of the spots results in large differences in the spot intensities, due to the algorithm used to calculate the phasemap that is applied to the SLM. Thus, a correction for these effects is essential. However, it is not possible to fit the peaks for each individual measurement (as it is done with the EMCCD camera), since the CMOS-SPAD detector features a large pixel pitch and the spots have consequently to be placed on adjacent SPADs. Therefore, no information from in between the active areas is available that could be used to model the intensity distribution and correct the autocorrelation functions for the unwanted effects.

The following procedure allows nevertheless a reliable correction for the crosstalk and background: In addition to the signal on the nine SPADs on which the spots are focused, the signal on two “dark” SPADs is saved during each measurement. The two dark SPADs are located in the columns left and right of the 3×3 array, in the middle line. In measurements with a low overall count rate (which was the case for the measurements in cells presented below), the signal on a second pair

of dark SPADs (line above and below the 3×3 array, middle column) was saved, since the data flow did not reach the limit of the data transmission via USB. The signal on the dark SPADs is used to determine the constant background due to non-diffracted light that is reflected by the SLM.

An image of the nine spots taken on the CDD camera yields the intensity distribution in the 3×3 spots and in their vicinity (figure 6.4(a)). The constant background on the CCD image is determined by the mean value of the pixels that correspond to the location of the dark SPADs (green or red crosses). The intensity distribution on the CCD camera is fitted with the nine-peak Lorentz function

$$L(x, y) = \left(\sum_{i=1}^9 A_i \frac{p}{(x - x_i)^2 + (y - y_i)^2 + p^2} \right) + c \quad (6.1)$$

where i is the number of the spot, A_i an amplitude factor, p the half width of the peaks, c the constant background and (x_i, y_i) the position of the peak maxima. The fit result is shown in figure 6.4(b). The relative amplitudes of the Lorentzian peaks differ from one measurement to another, since they depend on the spatial distribution of the fluorophor in the studied sample, but the fit allows nevertheless to determine the half width p .

The area of one SPAD corresponds to a circle with a diameter of 4.8 CCD pixels in the plane of the CCD camera (blue circle in figure 6.5). The signal measured on one SPAD is approximated as the average of the sum of the signals in the red framed and in the green framed pixels in figure 6.5. The signal S measured on SPAD m can thus be written as

$$S_m = \frac{1}{2} \left(\sum_{\substack{x_{green} \\ y_{green}}} \sum_{i=1}^9 A_i \frac{p}{(x_{green} - x_i)^2 + (y_{green} - y_i)^2 + p^2} + \sum_{\substack{x_{red} \\ y_{red}}} \sum_{i=1}^9 A_i \frac{p}{(x_{red} - x_i)^2 + (y_{red} - y_i)^2 + p^2} \right) + S_{DS} \quad (6.2)$$

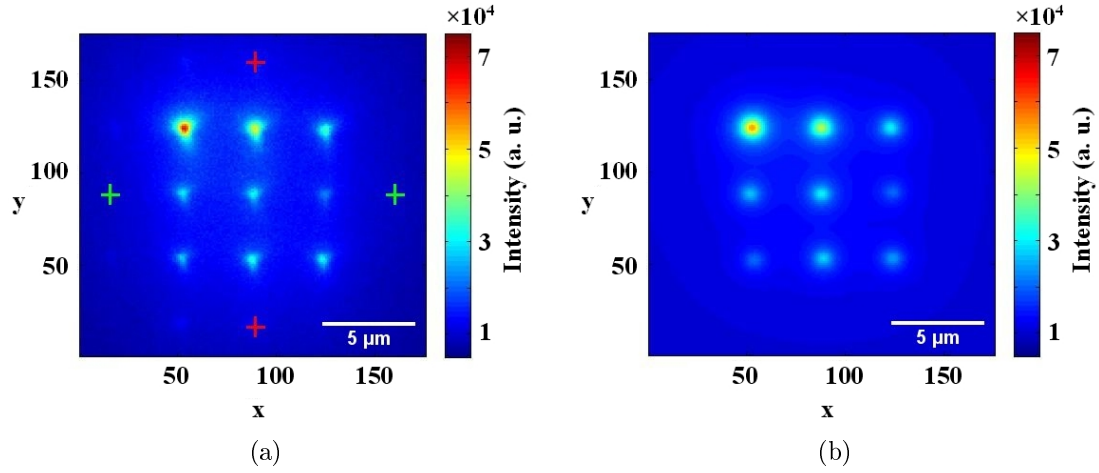


Figure 6.4.: Intensity distribution in a CCD image of the 3×3 spots created in a solution of Dextran-Rhodamine Green. The mean signal on the two (green crosses) or four pixels (green and red crosses) determines the constant background of the CCD image (a). The fit to the measured distribution with a nine-peak Lorentz function (b).

where x_{green} , y_{green} , x_{red} and y_{red} are the coordinates of the pixels in the green or red framed areas for SPAD m . S_{DS} is the mean signal on the dark SPADs that accounts for the constant background. Since p as well as the signals S_m measured on the 9 SPADS and the mean signal on the dark SPADs S_{DS} are known, the Amplitude factors A_i can be calculated.

In order to eliminate crosstalk and background effects, the constant background and the side wing contributions from all other spots have to be subtracted from the signal on a given SPAD m . The fraction that has to be subtracted is thus

$$I_m = \frac{1}{2} \left(\sum_{\substack{x_{green} \\ y_{green}}} \sum_{i=1, i \neq m}^9 A_i \frac{p}{(x_{green} - x_i)^2 + (y_{green} - y_i)^2 + p^2} + \sum_{\substack{x_{red} \\ y_{red}}} \sum_{i=1, i \neq m}^9 A_i \frac{p}{(x_{red} - x_i)^2 + (y_{red} - y_i)^2 + p^2} \right) + S_{DS}. \quad (6.3)$$

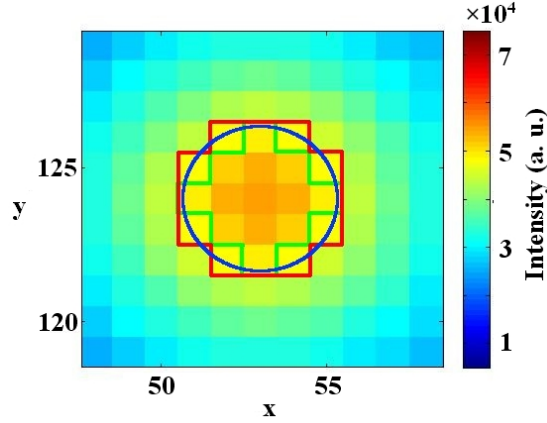


Figure 6.5.: The SPAD detector area (blue circle) in the plane of the CCD camera. The signal measured on a SPAD is approximated as the average of the sum of the signals in the red and green framed pixels.

I_m is used to correct the amplitude of the autocorrelation functions once they are calculated. The corrected autocorrelation function $G_m^{corr}(\tau)$ measured on SPAD m is thus [116–118]

$$G_m^{corr}(\tau) = (G_m^{meas}(\tau) - 1) \frac{1}{\left(1 - \frac{I_m}{S_m}\right)^2} + 1 \quad (6.4)$$

where G_m^{meas} is the autocorrelation function obtained without correction.

6.4. Calibration in solution

In order to estimate the spatial resolution in an FCS experiment using the SLM for excitation and the CMOS-SPAD array for detection, the different combinations of excitation and detection pathways were tested (in analogy to the measurements with the EMCCD camera presented in section 3.1). Figure 6.6 shows the autocorrelation functions measured with all four possible combinations and the resulting fit parameters. When using the SLM for excitation only one central spot was created. All measurements were done in the same Sulforhodamine solution and the laser power was adjusted to be the same in the sample in all cases. Since its time resolution is worse ($2\mu s$ instead of $0.2\mu s$ for the APD), triplet dy-

namics can not be assessed when using the CMOS-SPAD detector.

The enlargement of the effective volume that occurs when switching from the direct to the SLM excitation pathway was already discussed in section 3.1. As the EMCCD camera detection pathway, the CMOS-SPAD detection implies an enlargement of the effective volume. The spatial resolution for the SLM-CMOS-SPAD system is not very far from the one of the classical FCS system. However, it is important to know the exact lateral width of the observation volume in order to be able to calculate absolute diffusion constants.

excitation	→	detection	N	$\tau_D(\mu\text{s})$	$\omega_r/\omega_r^{\text{direct}\rightarrow\text{APD}}$
direct pathway	→	APD	5.1	22.6	1.00
SLM pathway	→	APD	7.7	29.6	1.14
direct pathway	→	CMOS-SPAD	7.8	29.4	1.14
SLM pathway	→	CMOS-SPAD	11.2	37.0	1.28

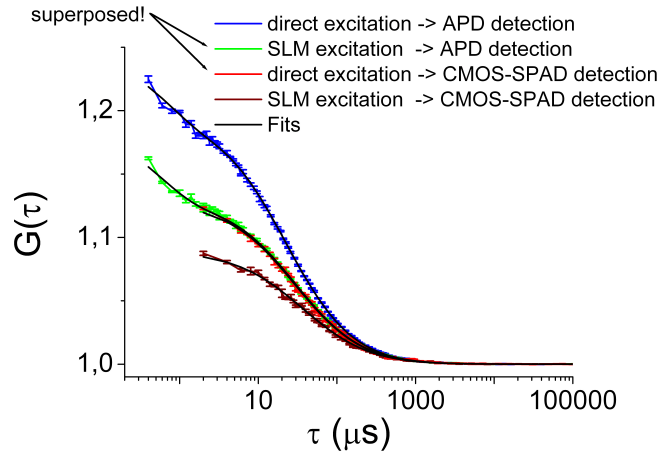


Figure 6.6.: Autocorrelation functions measured for the different combinations of excitation and detection pathways (blue, green, red, purple) and the estimated number of molecules and diffusion times from the fits (black). In addition, the radial elongation of the observation volume ω_r , which is normalized to its value for direct excitation and detection on the APD, is given. When using the SLM for excitation, only one central spot was created. Measurements were done in the same Sulforhodamine solution and the laser power was adjusted to yield the same value in the sample in all four cases.

To determine the latter, FCS measurements were conducted creating one spot by the SLM and detecting on both APD and on a single CMOS-SPAD. The sample

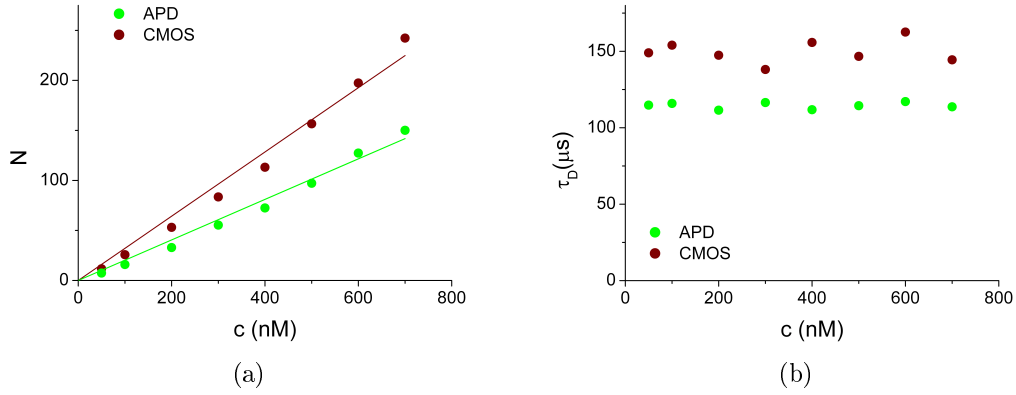


Figure 6.7.: Average number of molecules (a) and diffusion times (b) in solutions of Dextran-Rhodamine Green in a range of concentrations from 50nM-700nM. A single spot was created by the SLM and detected on APD (green circles) and CMOS-SPAD (purple circles). A large span of concentrations can be measured reliably with both detectors. The radial size of the observation volume is larger for detection on the CMOS-SPAD camera than for APD detection.

used is Dextran-Rhodamine Green diluted to concentrations ranging from 50nM up to 700nM. The results in terms of number of molecules N and diffusion times τ_D are given in figure 6.7. Since N rises linearly with the concentration and τ_D stays constant, it can be concluded that the CMOS-SPAD detector is suitable for measuring this large span of concentrations as reliably as the APD.

The slope for the estimated N as a function of the concentration is by a factor 1.6 larger for CMOS-SPAD detection than for APD detection, which indicates an increased effective volume. A possible explanation for this increase is the difference in the APD and CMOS-SPAD detector areas. The fiber core, which serves as pinhole for detection on the APD has a diameter of $4.2\mu\text{m}$ in the plane of the CMOS-SPAD detector. Together with the SPAD diameter of $6.7\mu\text{m}$, this yields a detector area that is by a factor 1.6 larger for CMOS-SPAD detection.

The diffusion times measured with the CMOS-SPAD are 1.3 times larger than the diffusion times measured with the APD, which indicates an enlarged radial observation volume. With the radial size of the observation volume for SLM excitation and APD detection (see section 3.3) and the ratio of the diffusion times, the radial size of the observation volume ω_r is calculated for CMOS-SPAD

detection to be $(0.241 \pm 0.003)\mu m$.

As in the fits to APD and EMCCD data, the fits to autocorrelation functions measured with the CMOS-SPAD yielded in general the value 5 for the structure parameter S . For the reasons discussed in section 2.6.3, it was fixed to 5 for all fits.

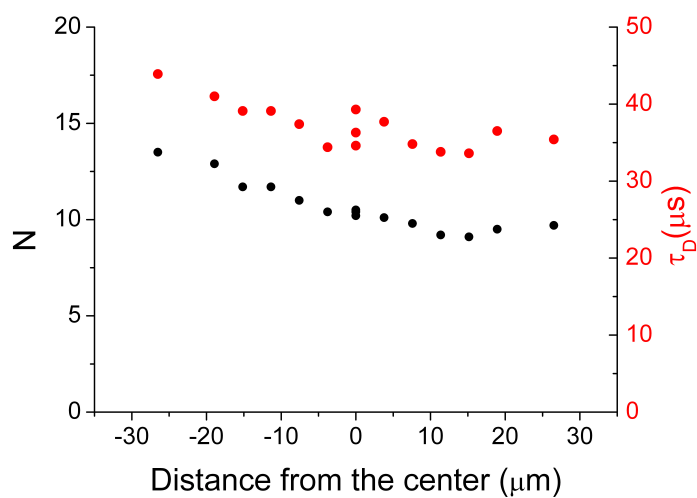


Figure 6.8.: Average number of molecules (black circles) and diffusion times (red circles) estimated from FCS experiments in a Sulforhodamine solution. A single spot was created by the SLM and shifted away from the optical axes in steps of $3.8\mu m$.

In order to check for unwanted effects when creating spots out of the optical axis, a single spot was created by the SLM and shifted away from the optical axis in steps of $3.8\mu m$ in horizontal direction. Detection was performed on the corresponding SPADs. Three out of the thirteen SPADs used featured a DCR larger than 50Hz. As can be seen in figure 6.8, N and τ_D tend to increase for large distances to the center (which can be explained by optical aberrations getting more important with increasing angles), but the effect is clearly more pronounced for shifts to the left. Since the measured number of molecules and diffusion times tend to be minimal about $10\mu m$ to the left of the designated optical axis, the “true” optical center seems to be located there. This may be the result of a small misalignment in the detection path.

The mFCS measurements presented in the following were done in a 3×3 spot configuration on adjacent SPADs with the center spot being located in the optical center. The maximal distance of a given spot to the optical center is $\sqrt{2} * 3.8\mu m$. It can be assumed that shifting the volume in any direction does not cause a more important effect than a shift in the horizontal direction. Therefore, it can be concluded that the effect is negligible for the used configuration of 3×3 spots.

The last test measurement concerns the creation of multiple spots and its impact on the measured parameters. One and 3×3 spots were created in solutions of Dextran-Rhodamine Green solutions with concentrations ranging from 50nM to 700nM and detection was performed on one and nine SPADs respectively. The resulting number of molecules and diffusion times are shown in figure 6.9 (a) and (c).

While the number of molecules found in the most intense of the 3×3 spots is already significantly increased (yellow circles in figure 6.9(a)) compared to the single spot case (purple circles), the effect is dramatic for the central spot (orange circles). This result could be expected, since the middle spot has more nearest neighbors and a lower intensity and is therefore more affected by background and crosstalk effects than the most intense spot. The correction for crosstalk and background shifts the number of molecules for the central spot (red circles in figure 6.9(b)) and the most intense spot (green circles) near the result for the single spot case (purple circles).

The diffusion times measured for a single (purple circles in figure 6.9(c)) and the most intense of 3×3 spots (yellow circles) do not differ and are certainly not changed by the correction (green circles). It can therefore be concluded that creating multiple spots does not alter the size and form of the observation volume and the lateral width ω_r is $(0.241 \pm 0.003)\mu m$ as in the single spot case.

6.5. Measurements in HELA-eGFP cells

Measurements in HELA-eGFP cells have been done in order to show the feasibility of mFCS experiments in living cells with detection on the CMOS-SPAD array.

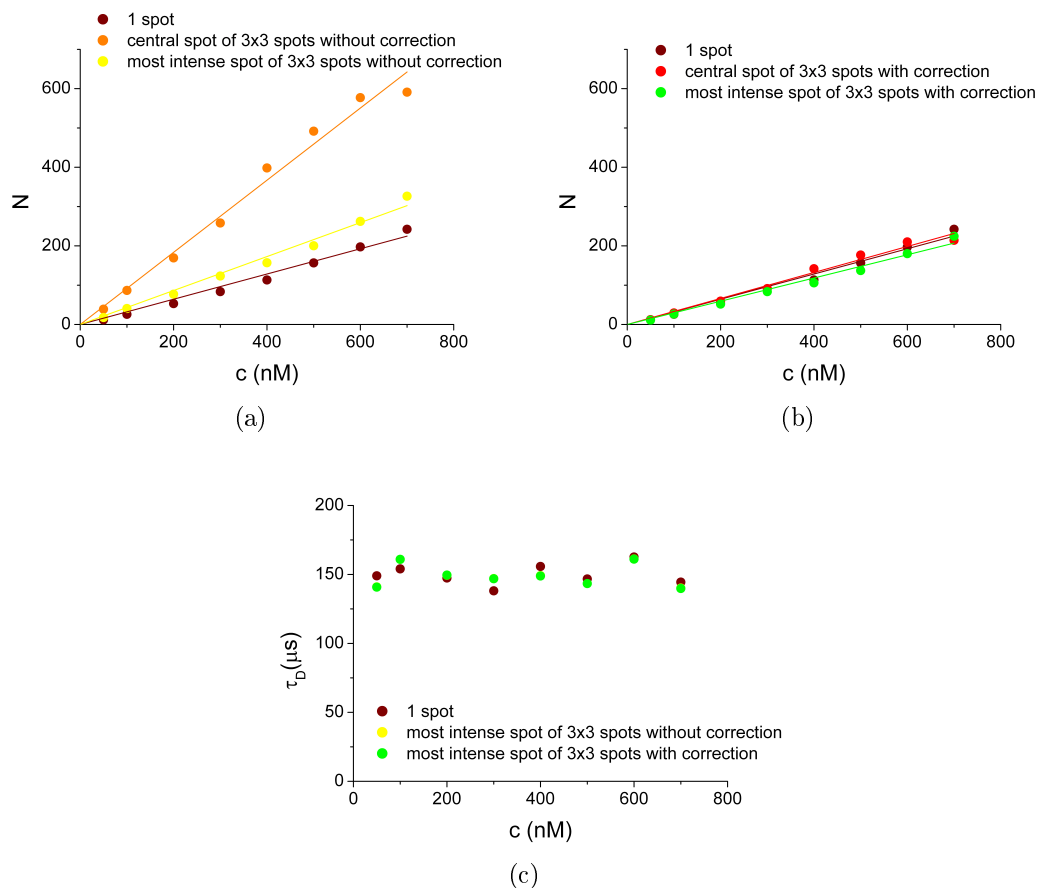


Figure 6.9.: Average number of molecules estimated from FCS measurements in a single spot (purple circles), in the central spot of 3×3 spots (orange circles) and in the most intense spot (yellow circles) (a). Experiments were done in solutions of Dextran-Rhodamine Green with varying concentrations and detection was done with the CMOS-SPAD camera. The apparent increase in the number of molecules is due to crosstalk and background effects and can be corrected for (b). The diffusion times (c) for one (purple circles) and the most intense of 3×3 spots (yellow circles) do not differ and are certainly not changed by the correction (green circles).

Cells were kept at a temperature of 37°C throughout the experiment. An array of 3×3 spots was created by the SLM and placed in the nuclei and cytoplasm of 12 cells.

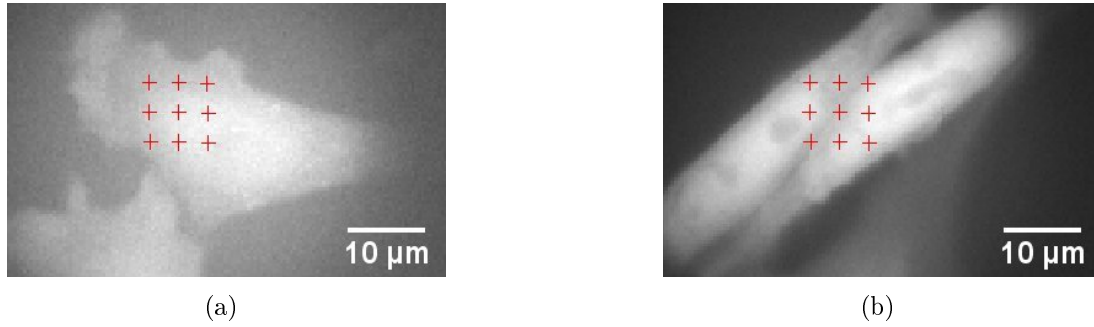


Figure 6.10.: Two examples for the location of the 3×3 spots in the 12 cells that were used to calculate the mean autocorrelation functions in figure 6.11.

Unlike in experiments with the EMCCD camera, the spots were not shifted in the same cell for a second measurement. Figure 6.11 shows the results of these measurements. Out of 96 spots that were placed in the cells, 67 were located in the nuclei and 29 in the cytoplasm.

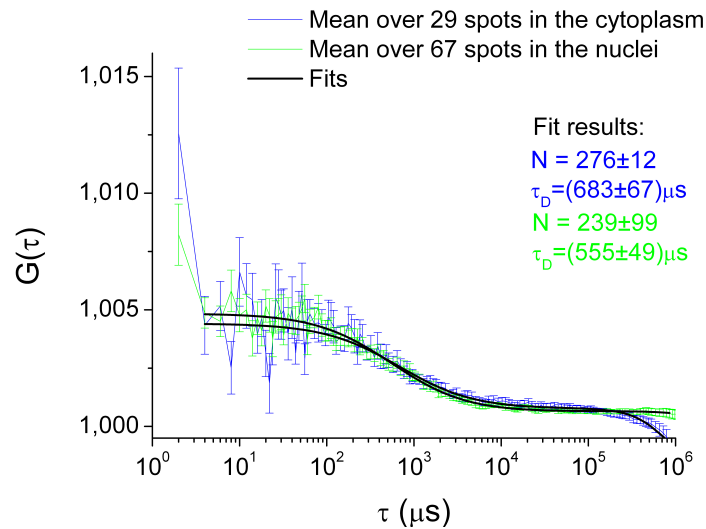


Figure 6.11.: Mean over 67 autocorrelation functions for spots located in the cytoplasm (blue) and 29 autocorrelation functions for spots in the nuclei (green) of 12 HELA-eGFP cells.

The mean autocorrelation functions were fitted with a simple diffusion model (equation 2.5 with $F_{eq} = 1$). The fit yields a diffusion time τ_D of $(555 \pm 49)\mu s$ for measurements in the nuclei. With a lateral width of the observation volume of $(0.241 \pm 0.003)\mu m$ (see section 6.4), a diffusion constant of $(26 \pm 3)\mu m^2 s^{-1}$ for eGFP in the nucleus was calculated. This value is close to published values [94, 119] and not far from the value found with EMCCD detection (section 5.2.2), which is by a factor 1.4 larger.

Notably, the diffusion constant in the cytoplasm ($D = (21 \pm 3)\mu m^2 s^{-1}$) is smaller than in the nucleus, which is surprising, since no difference could be observed between the two constants in the measurements presented in section 5.2.2.

When comparing the mean autocorrelation functions for measurements in HELA-eGFP cells in five spots on a line (and detection on the EMCCD camera) in figure 5.2 and in 3×3 spots (and detection on the CMOS-SPAD camera) in figure 6.11, it becomes obvious that the standard errors of the mean are larger in the latter case. This is mainly due to the increased unfocused background that goes along with the creation of more spots in two dimensions. Therefore, a compromise between the number of spots and the signal-to-noise ratio has to be made. However, the diffusion constant of the inert eGFP molecule in HELA cells could also be successfully measured in 3×3 spots.

7. Conclusion

In this work, a new mFCS technique for simultaneous measurements in several locations within a living cell, has been proposed. With this method we assessed the dynamics of a transcription factor, heat shock factor 1 (HSF1) in heat-shocked and non-heat-shocked cells. Aside from this project, a CMOS-SPAD camera has been tested as an alternative detector for multi-spot experiments in living cells. The first goal of this work was to evaluate the feasibility of mFCS experiments in living cells using an SLM for excitation and an EMCCD camera for detection. Therefore the spatial and temporal resolution of the system and its sensitivity were compared to a classical FCS setup.

The SLM is used for the creation of five independent observation volumes in the sample. Thereby, the applied phase map is calculated with the spherical wave and superposition approach [59]. Parallel detection is performed on the EMCCD camera operated in the Crop FvB readout mode. Consequently a time resolution of $14\mu s$ can be achieved. The price to pay is that the spot geometry is confined to a row. As the spot intensities are not uniform, a correction for crosstalk between neighboring spots and for background caused by non-diffracted light has to be done.

Compared to a classical "one spot" FCS experiment with detection on an APD, the time resolution of the mFCS system is lower ($14\mu s$ vs. $0.2\mu s$). However, it is easily compatible with the dynamics of most cellular proteins. The lateral width of the observation volumes ω_r was found to be $(0.251 \pm 0.002)\mu m$. Hence the spatial resolution of the mFCS system is comparable to a classical FCS system, where ω_r yields $(0.211 \pm 0.002)\mu m$. The sensitivity of the EMCCD camera comes close to that of an APD, even if the APD is slightly more performant for low laser powers or low fluorophor concentrations. For high fluorescence intensities in contrast, the use of an EMCCD camera for detection may be advantageous

since the gain can be adjusted to avoid saturation or damage, which is not feasible with an APD. The working range of the detectors, in terms of fluorophore concentration and excitation power, was estimated from the quality of the fits to the measured autocorrelation functions.

It has to be said that the data acquisition and processing is a relatively complex process. It involves the piloting of the SLM, the EMCCD camera, the CCD camera, the laser shutter, the microscope stage and to make corrections on the time traces before fitting the data. Therefore a graphical user interface has been developed and the measuring protocol and the analysis have been automated to a large extent.

In summary it can be stated that the spatial and temporal resolution of the mFCS system is more than adequate to measure the dynamics of a transcription factor in living cells and that its sensitivity is comparable to a classical FCS system. Even if the spot geometry is confined to a row, the technique allows to gather spatial information from several independent observation volumes. In addition, the multiplexing yields reliable statistical results in a time-saving way.

The second goal of this work was to assess the changes in the dynamics of the transcription factor HSF1 upon heat shock with the SLM-EMCCD mFCS system. Beforehand, control measurements were conducted on HELA cells expressing the inert eGFP molecule. No difference in the concentration and diffusion of inert eGFP in the unstressed (37°C) and stressed cell (43°C) has been found. The change in chromatin structure that goes along with a heat shock [56] does not seem to affect the dynamics of the molecule, possibly because the structural effect is counterbalanced by a decrease in the viscosity of the cellular medium due to the temperature change. In addition, the intracellular homogeneity of the diffusion constant does not change upon heat shock.

The concentration and dynamics of HSF1-eGFP in contrast, is clearly affected by the heat shock. The measured drop in concentration can be attributed to the trimerization of the HSF1-eGFP complexes, the relocalization in nSBs (accumulations on satellite III repeats) and the specific binding to HSEs. Photobleaching effects tracked over several consecutive acquisitions reveal the presence of dynamics at very long time scales, inaccessible to FCS measurements. However, the heat shock also causes important changes in the dynamics that falls in the

measuring range of FCS: A fit with a diffusion-interaction model [64] to the measured autocorrelation functions reveals association and dissociation events before and during heat shock that we interpret as non-specific binding to DNA. The non-specific binding sites seem to be homogeneously distributed throughout the nucleus. Upon heat shock specific interactions occur additionally. These specific interactions appear less homogeneously throughout the nucleus and can thus be interpreted as the specific binding to HSEs, which are rare in the genome [55]. These observations are in agreement with models suggesting that the dynamics of a transcription factor is governed by diffusion through the nucleus and stochastic non-specific interactions, until the encounter of a specific binding site [102–107]. The same results have been obtained in two different human cell lines, U87 and HELA cells.

In order to gain an insight into the role of the distinct domains of HSF1 in the heat shock response, the dynamics of deletion mutants was assessed. Consistently with prior observations [84, 85], we found that the trimerization of HSF1 is necessary for specific DNA binding. The trimerization domain is possibly even involved in the non-specific binding. More surprising results were obtained for HSF1 featuring a mutated [91] or entirely removed DNA binding domain. HSF1 does indeed not form nSBs, but contrary to what could be expected, it does not completely lose the ability to bind DNA specifically. In the case of the mutated DNA binding domain, endogenous HSF1 was silenced so that trimerization with the endogenous complex could be excluded. The deletion of a part of the transactivation domain did not influence the formation of nSBs, but resulted in increased dissociation rates. This raises the question if proteins binding to the transactivation domain may be involved in stabilizing the HSF1 DNA-bond.

The third goal of this work concerned the test of a 32×32 CMOS-SPAD camera as a detector for mFCS. Colyer et al. [47, 48] recently showed the feasibility of measurements in solution, but to my knowledge the SLM-CMOS-SPAD system has never been used for measurements in living cells. In addition, cross-contributions from neighboring spots were an unsolved problem [48]. Compared to the EMCCD camera, the CMOS-SPAD detector allows to achieve a better time resolution ($2\mu s$ vs. $14\mu s$). The spatial resolution in contrast is comparable to the SLM-EMCCD and the classical FCS system, since ω_r yields $(0.241 \pm 0.003)\mu m$. An array of 3×3

spots has been used for CMOS-SPAD measurements. Also here, the spot intensities are not uniform and crosstalk and background effects are more important than for measurements with the EMCCD camera, since more spots are created and not only placed on one line, but in two dimensions. It has been shown in this work that the amplitudes of the autocorrelation functions can be corrected for this effect. One problem remains: The more spots are used for a measurement, the more uncorrelated background occurs and the lower is the signal-to-noise ratio in the measurement.

In order to show the feasibility of mFCS measurements in living cells with detection on the CMOS-SPAD array, the dynamics of inert eGFP in HELA cells has been analyzed in 3×3 spots. The measured diffusion constant is reasonably close to published values [94, 119] and to the one found by EMCCD detection, which is by a factor 1.4 larger.

In my opinion the developed mFCS technique is a very promising approach to analyze various biological problems. One weak point for the time being are the crosstalk and background effects occurring in the measurements. They can be corrected for, but decrease nevertheless the signal-to-noise ratio. It could be worthwhile to test other methods than the spherical wave and superposition approach [59] to calculate the SLM phasemap, in order to decrease the amount of unfocused background and to achieve more uniform spot intensities. One possibility, which has not yet been implemented because it requires extensive modifications in the experimental setup, could be to switch from spherical waves to plane waves and use a weighted Gerchberg-Saxton algorithm [120].

An additional interesting application of the mFCS technique would be to measure flow rates by cross-correlation between the volumes. This possibility has transiently been tested on microbeads in a flow channel (data not shown) and gave encouraging results. As flows in cells are likely to be weak, the distances between the observation volumes would probably have to be decreased. This would certainly increase the side wing contributions from adjacent spots, which could be corrected for with the method proposed in this work. If the signal-to-noise ratio, which should decrease with decreasing distances would be sufficiently high to assess the dynamics of the studied component, is an interesting question.

At the time being a limitation of the SLM-EMCCD system is the confinement

of the spot geometry to a row, in order to be able to use the Crop FvB readout mode. Theoretically it should be possible to place the spots on different lines (but not on exactly the same column), to mask all unused lines and to still use the Crop FvB readout mode in order to keep the high time resolution. Therefore it would be worthwhile to investigate the technical possibilities for masking single rows on the EMCCD camera chip.

Using the SLM-CMOS-SPAD system it is indeed possible to perform detection along two dimensions, but due to the large pixel pitch the number of spots that can be placed in one cell is limited and since adjacent SPADs have to be used, the spot geometry is rigid. Fast CMOS-SPAD detectors with small distances in between the pixels and the possibility of rapid data transmission would therefore constitute a huge advance in mFCS techniques.

As to the biological application studied in this work, it has been seen that the dynamics of HSF1 in the cell includes short-time as well as long-time behavior. Thus, it is interesting to approach the problem with a complementary technique: Fluorescence recovery after photobleaching (FRAP). In contrast to FCS, which takes advantage of small fluctuations of a system in equilibrium, FRAP investigates the diffusion of a fluorescently labeled species in a prior photobleached area in the sample and allows thus to assess dynamics on large time scales.

FRAP experiments on cells expressing HSF1-eGFP and the deletion mutants have been done by our collaborators Gaëtan Herbomel and Catherine Souchier at the Institut Albert Bonniot (IAB) in Grenoble. For comparison, figure 7.1 shows mean mFCS (a) and FRAP curves (b) measured in HELA cells expressing HSF1-eGFP before (blue) and during heat shock (red). Qualitatively the same behavior is observed for the two techniques: The dynamics of HSF1 slows down upon heat shock. However, when fitting the data obtained by FRAP with a diffusion-interaction model [64], analog to the one used for mFCS data (black lines), much smaller diffusion constants are obtained ($D_{FRAP}^{37^{\circ}C} = 3.4$ and $D_{FRAP}^{43^{\circ}C} = 0.37$ vs. $D_{mFCS}^{37^{\circ}C} = 14.4$ and $D_{mFCS}^{43^{\circ}C} = 7.8$). In addition, diffusion does not slow down with the same proportion upon heat shock. While D^{mFCS} is roughly reduced by a factor two, it is almost a factor ten for D^{FRAP} .

The discrepancy between the results obtained with the two complementary techniques raises new, interesting questions that could not be answered before the

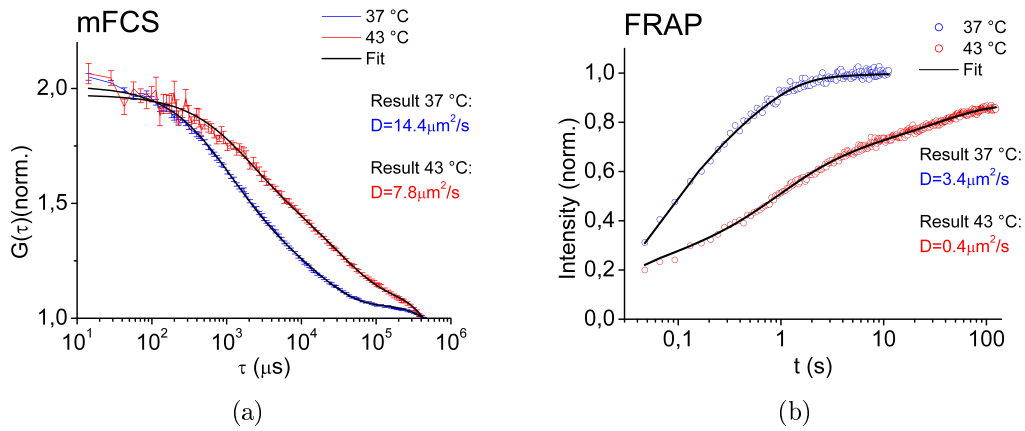


Figure 7.1.: Mean mFCS (a) and FRAP curves (b) measured in HELA-HSF1-eGFP cells before (blue) and during heat shock (red) and fits to the data (black) with a diffusion-interaction model [64]. Much smaller diffusion constants D are obtained when assessing HSF1 dynamics with FRAP. (Please note the different time scales on the abscissae.)

submission of this manuscript. A particularly promising approach to address them, is the new project of the MOTIV team: The combination of mFCS and mFRAP on the same setup. Thus, the covering of a large time range would join the advantages of the mFCS system.

A. Appendix

A.1. Time resolutions for different EMCCD camera readout modes

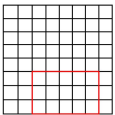
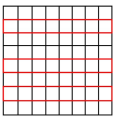
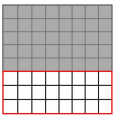
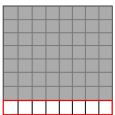
Readout mode		Time resolution
ROI		3 rows at the bottom of the chip: $200\mu s$
Multi-track		3 rows (1 at the upper, 1 at the middle, 1 at the bottom part of the chip): $240\mu s$
Crop		3 rows the bottom of the chip: $100\mu s$
Crop FvB		1 row at the bottom of the chip: $14\mu s$

Table A.1.: Examples for time resolutions that may be achieved for a given pixel configuration and different readout modes of an EMCCD camera.

A.2. Correlation between the fit parameters B and τ_{off}

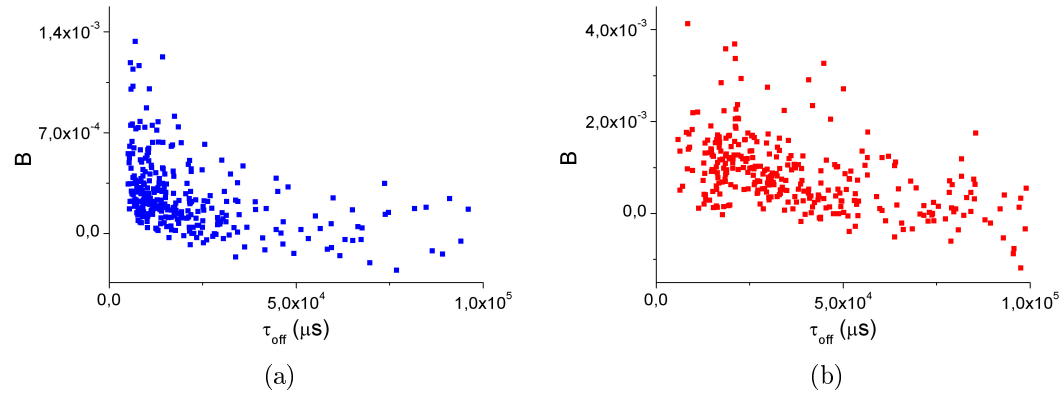


Figure A.1.: Relation between the fit parameters B and τ_{off} for fits to 330 autocorrelation functions measured at 37°C (a) and to 344 autocorrelation functions measured at 43°C (b). There is only a weak correlation between the two fit parameters. The Pearson product-moment coefficient ρ yields -0.3 for fits to autocorrelation functions measured at 37°C and -0.4 for autocorrelation functions measured at 43°C.

B. Partie française

B.1. Introduction

Quand Magde et al. publiaient leurs premiers résultats d'expériences de spectroscopie à corrélation de fluorescence (FCS) en 1972, ils suggéraient que leur méthode pourrait avoir des applications intéressantes en biophysique [1]. Il s'avéra qu'ils avaient vu juste. En particulier, avec la microscopie confocale [2–5], la FCS est devenue un outil puissant pour l'étude de la dynamique des biomolécules marqués avec des colorants.

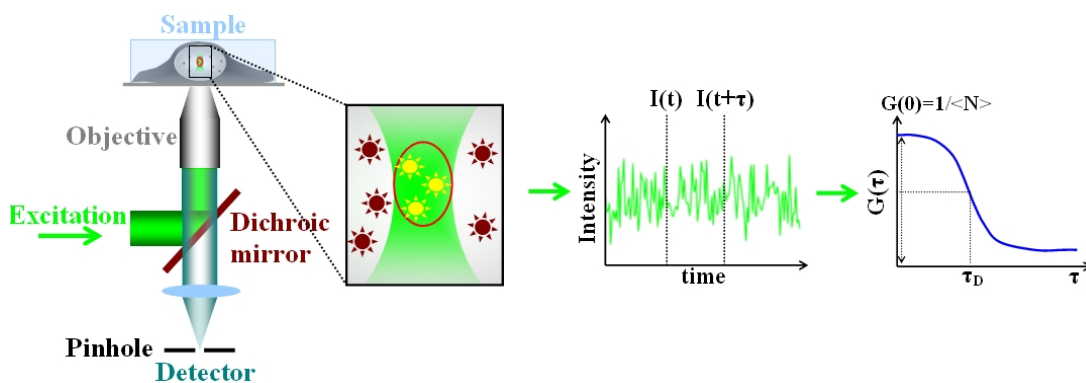


Figure B.1.: Le principe de la technique FCS. Des molécules fluorescentes diffusent à travers le volume d'observation d'un microscope confocale. Des informations concernant leur concentration et leur dynamique peuvent être obtenues en autocorrélant les fluctuations d'intensité résultantes.

La technique est basée sur l'analyse des petites fluctuations d'intensité, causées par l'espèce fluorescente qui diffuse à travers le volume d'observation d'un microscope confocale (comme illustré dans la figure 1.1). Les fluctuations d'intensité observées dépendent de la concentration et de la dynamique des molécules ou

complexes étudiés. L'autocorrélation des fluctuations d'intensité détectées fournit la fonction d'autocorrélation $G(\tau)$, où τ désigne le décalage temporel. En ajustant $G(\tau)$ avec un modèle mathématique, le nombre moyen de particules, N , et le temps de résidence moyen dans le volume d'observation, τ_D , peuvent être trouvés. Si la taille de ce dernier est connue, des valeurs absolues, comme la concentration ou la constante de diffusion de l'espèce étudiée, peuvent être calculées. Puisque la FCS est très sensible et peu invasive [6], elle est bien adaptée à l'étude de la dynamique des biomolécules dans des cellules vivantes. Cependant, la cellule et le noyau cellulaire en particulier, ont une architecture complexe. Ce dernier contient des compartiments distincts [7], comme des nucléoles [8], des compartiments des facteurs d'épissage [9], des corps de Cajal [10] ou des territoires chromosomiques [11, 12], qui introduisent une hétérogénéité dans sa structure et son activité [13]. En plus, beaucoup des composants nucléaires (chromatine, RNA, facteurs de transcription,...) interagissent de façon dynamique [7, 12]. Afin de déduire l'information spatiale et temporelle qui est nécessaire pour arriver à mieux comprendre les mécanismes cellulaires, il est nécessaire d'effectuer des mesures à différents endroits d'une cellule.

Puisque la FCS classique est limitée à un unique volume d'observation, les informations spatiales peuvent seulement être obtenues en mesurant successivement les fonctions d'autocorrélation en des positions différentes. Ce protocole prend du temps et apporte des informations provenant de seulement un volume à la fois. Cependant, des changements spatiaux et temporels rapides peuvent être évalués seulement si des informations provenant des positions différentes sont enregistrées simultanément.

Dans les années passées, plusieurs techniques basées sur la spectroscopie à fluctuation de fluorescence ont été développées à cette fin. Une de celles-ci est la "temporal image correlation spectroscopy", (tICS), qui est basée sur la prise des images dans une série temporelle et l'autocorrélation de piles de pixels [14–17]. Comme la résolution de cette technique est limitée par la vitesse d'acquisition de la caméra, elle est plutôt adaptée à l'évaluation de dynamiques lentes.

Afin de surmonter ce limite, Digman et al. ont développé une méthode dénommée "raster scanning image correlation spectroscopy" (RICS) [18, 19]. Le RICS est basé sur l'emploi d'un microscope à balayage laser [20–23] et donne accès

aux informations spatiales et temporelles dans une gamme important grâce à la corrélation des signaux sur des pixels, des lignes ou des images adjacents [18]. Un désavantage de cette technique est que la région d'intérêt (ROI) doit être assez grande afin d'éviter le sous-échantillonnage, qui peut conduire à une décroissance incomplète de la fonction d'autocorrélation et ainsi à une estimation faussée des paramètres dynamiques [24].

Au lieu d'utiliser un microscope à balayage laser, Capoulade et al. [25] ont illuminés l'échantillon par un feuille de lumière et imagé la section sur une caméra EMCCD. En utilisant cette technique, des informations spatiales et temporelles de toute une section 2D de la cellule sont accessibles [25]. La limite de la méthode est que plus la section analysée est grande, plus la résolution temporelle est petite.

Une technique qui a été adaptée à des problèmes biologiques variés est le scanning FCS (sFCS) (voir par exemple [26–34]). Des informations spatiales et temporelles sont obtenues en balayant l'échantillon avec le laser, normalement sur un cercle [31–34] ou sur une ligne [26–30]. En bougeant le volume d'excitation correspondant les effets de photoblanchiment sont réduits et il n'est pas nécessaire de connaître la position exacte de la cible ce qui est avantageux quand on mesure par exemple des dynamiques dans des membranes [14, 35]. Le désavantage de la technique est qu'un compromis entre la résolution spatio-temporelle et l'extension spatiale doit être fait. En plus, il n'est pas possible d'obtenir des informations indépendamment et simultanément en des endroits différents dans la cellule, puisque seulement un volume d'excitation est utilisé.

Il est donc avantageux de créer plusieurs volumes d'excitation indépendants à la fois. Pour atteindre cet objectif, des microscopes confocaux à spinning disque, combinés avec des caméras CCD ou EMCCD ont été employés [36, 37]. Avec ces dispositifs il est possible de créer un grand nombre des volumes d'excitation simultanés dans l'échantillon. En revanche, la résolution temporelle est toujours limitée par la vitesse d'acquisition de la caméra.

Une approche très prometteuse est la combinaison d'un microscope confocal à spinning disque avec la méthode "time-integrated multipoint moment analysis" (TIMMA), qui donne une résolution temporelle de $20\mu s$ [38]. La technique TIMMA utilise elle aussi une caméra EMCCD pour la détection, mais la dy-

namique de l'espèce fluorescent en question est obtenue grâce à la dépendance de la moyenne et de la variance du signal du temps d'exposition [38]. En conséquence la résolution temporelle est limitée par le plus petit possible temps d'exposition de la caméra et non pas par sa vitesse d'acquisition. Pourtant, l'implémentation de cette méthode est compliquée. Entre autres, le bruit de lecture doit être éliminé en divisant le signal en deux images identiques et en calculant leur covariance et le gain de la caméra EMCCD doit être ajusté en fonction des temps d'exposition croissants afin d'éviter la saturation du détecteur [38].

Une nouvelle technique FCS multi-confocale (ci-dessous dénommée mFCS), qui permet de mesurer la dynamique de composants cellulaires, indépendamment et au même moment en des endroits différents dans une cellule, avec une haute résolution temporelle, est donc intéressante.

La première exigence de la nouvelle technique mFCS est la création de différents volumes d'excitation indépendants. Initialement il était prévu de choisir librement la position des spots, pendant que la cellule est observée lors d'une acquisition plein champ. Pour créer plusieurs spots laser dans la géométrie souhaitée, un modulateur spatial de lumière (SLM) est utilisé. Les SLM sont surtout connus pour leurs applications aux pinces optiques [39–41] et en tant que correcteurs de front d'onde en astronomie [42], mais ils sont également bien adaptés à des expériences FCS. Blancquaert et al. par exemple ont mesuré des flux moléculaires ainsi que la perméabilité d'une membrane phospholipidique par spectroscopie à corrélation croisée de fluorescence dans deux volumes d'observation générés par un SLM [43]. L'idée initiale de choisir librement la géométrie des spots n'a pas été implémentée pour deux raisons: Premièrement un alignement précis de chaque spot sur un pinhole du détecteur est indispensable. La procédure d'alignement prend quelques minutes et n'est donc pas compatible avec des mesures dans des cellules vivantes. Deuxièmement, le prix pour une détection avec une haute résolution temporelle est une géométrie des spots qui est confinée sur une ligne. Malgré tout l'emploi du SLM offre la possibilité d'adapter aisément le nombre des spots et leurs distances au projet ou au type cellulaire avant de commencer des mesures.

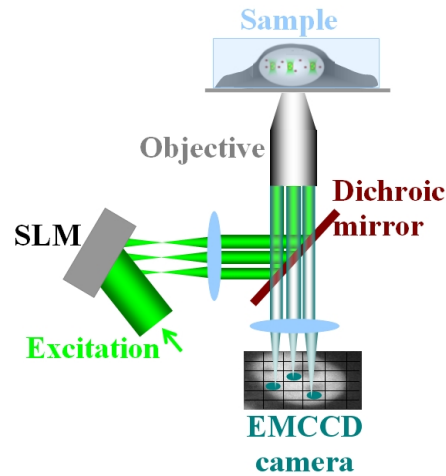


Figure B.2.: Schéma illustrant la technique mFCS initialement prévue. Plusieurs spots laser peuvent être positionnés d’une manière flexible par un SLM dans une géométrie adaptée à la cellule respective. La détection est réalisée sur les pixels d’une caméra EMCCD qui jouent le rôle des pinholes individuels pour la détection confocale.

Le deuxième défi est d’atteindre une détection en parallèle: Le détecteur doit être une matrice des pinholes individuels qui sont sensibles à des photons uniques et assez rapide pour atteindre une résolution temporelle qui est compatible avec la dynamique du composant cellulaire analysé. A cette fin, une caméra EMCCD a été utilisée. Il a déjà été montré que les pixels d’une caméra EMCCD peuvent jouer le rôle des détecteurs des photons uniques individuels pour des expériences FCS [44–46] et qu’une haute résolution temporelle peut être atteinte en utilisant des modes de lecture spéciaux. Burkhardt et al. [44] par exemple ont effectués des expériences FCS avec détection sur une caméra EMCCD dans deux volumes d’excitation dans des colorants en solution et ils ont atteints une résolution temporelle de $20\mu s$. Dans ce travail, un mode de lecture dénommé Crop FvB est utilisé, qui donne une vitesse d’acquisition de 70kHz et donc une résolution temporelle de $14\mu s$.

Les nouvelles caméras “Complementary Metal Oxide Semiconductor-Single Photon Avalanche Diode” (CMOS-SPAD) offrent la possibilité de multiplexer et d’atteindre une sensibilité aux photons uniques avec la résolution temporelle d’une APD. La faisabilité des expériences mFCS utilisant un SLM pour l’excitation et une caméra

CMOS-SPAD pour la détection dans 8 et 64 spots dans une solution a été montrée récemment par Colyer et al. [47, 48]. Cependant à ma connaissance le système SLM-CMOS-SPAD n'a jamais été utilisé pour des mesures dans des cellules vivantes et les contributions croisées des spots voisins posent un problème qui n'a pas encore été résolu jusqu'à maintenant [48]. Ceci est un obstacle important pour des mesures dans des cellules vivantes: Les volumes d'excitation ne peuvent pas être séparés par une grande distance, car ils doivent se situer dans une même cellule. Dans ce travail, une nouvelle caméra CMOS-SPAD a été évaluée en tant que capteur pour des expériences mFCS. Une solution au problème des contributions croisées a été proposée et le dispositif a été testé pour des mesures dans des cellules vivantes.

Le but principal de ce travail est le développement du système mFCS et son application à l'étude de la réponse cellulaire au stress thermique. Antoine Delon et Catherine Souchier ont choisis d'étudier la dynamique d'un facteur de transcription, heat shock factor 1 (HSF1), qui joue un rôle important dans la réponse au choc thermique [49]. Il est connu que, lors d'un choc thermique, HSF1 est activé, trimerisé [49, 50], phosphorylé [51] et lié à des sites de liaison spécifiques de l'ADN [52–54]. Le nombre de ces sites de liaison spécifiques dans le génome est limité [55]. La technique mFCS est ainsi parfaitement adaptée à l'étude de la dynamique de HSF1 puisqu'elle ne donne pas seulement accès à des informations temporelles mais aussi à des informations spatiales. De plus, la quantité de données produite est plus importante qu'en utilisant la technique FCS classique et devrait ainsi permettre d'obtenir des résultats statistiquement significatifs en moins de temps.

Ce travail a pour but de répondre à trois questions: La première concerne la faisabilité des expériences mFCS en cellules vivantes en utilisant un SLM pour l'excitation et une caméra EMCCD pour la détection. Les résolutions spatiale et temporelle, sont-elles adéquates pour l'étude de la dynamique de HSF1 et comment peut-on classer la sensibilité du système par rapport à un montage FCS classique?

Le sujet de la deuxième question traite la dynamique de HSF1: De quelle manière est-elle affectée par le choc thermique? Sur quelle échelle de temps la liaison à l'ADN se déroule-t-elle et est-ce qu'elle peut-être évaluée par mFCS? Les inter-

actions, sont-elles spatialement homogènes et quelle effet la modification de la structure chromatinienne qui apparaît lors d'un choc thermique [56] a-t-elle sur la dynamique?

La dernière question se porte sur la possibilité d'utiliser un capteur CMOS-SPAD pour la détection mFCS. Sa performance est-elle comparable à celle d'une caméra EMCCD et des mesures dans des cellules vivantes sont-elles possibles?

Afin de répondre à ces questions, le travail est structuré comme suit: Les méthodes expérimentales sont présentées dans chapitre 2. Le montage mFCS est introduit et l'excitation multi-confocale via un SLM et la détection multiplexé avec une caméra EMCCD sont expliqués. Par la suite, les méthodes pour l'acquisition et le traitement des données sont décrites. De plus, le protocole pour la culture cellulaire est donnée.

Le chapitre 3 révèle les caractéristiques et les performances de la technique mFCS, qui vont être comparés à des expériences FCS classiques. De plus, la résolution temporelle et spatiale de la technique mFCS est analysée et ses points forts ainsi que ses limites vont être relevés.

Le chapitre 4 introduit la notion de réponse au choc thermique des cellules eucaryotes, de la structure et de la fonction du facteur de transcription HSF1 et des mutants qui ont subi une délétion.

En guise de contrôle, la dynamique de la molécule eGFP inerte dans des cellules HELA vivantes va être analysée dans le chapitre 5. Ensuite l'effet d'un choc thermique sur la dynamique de HSF1 va être étudié. Afin de clarifier le rôle des différents domaines, la dynamique des mutants va être discutée.

Dans le chapitre 6 la possibilité d'utiliser une nouvelle caméra CMOS-SPAD en tant que détecteur pour la mFCS va être explorée. Après la description du traitement des données, ses performances vont être évaluées par des mesures en solution. La faisabilité des mesures dans les cellules vivantes est démontrée à l'aide des cellules HELA qui expriment la molécule eGFP inerte.

Enfin le chapitre 7 ferme ce travail par une conclusion.

B.2. Résumé et conclusion

Dans ce travail une nouvelle technique mFCS pour des mesures simultanées en différents endroits dans une cellule vivante a été proposée. En utilisant cette méthode nous avons évalué la dynamique d'un facteur de transcription, heat shock factor 1 (HSF1), dans des cellules heat-shockées et non-heat-shockées. En plus de ce projet, une caméra CMOS-SPAD a été testée en tant que capteur alternatif pour des expériences avec des spots multiples dans des cellules vivantes. Le premier but de ce travail était d'évaluer la faisabilité des expériences mFCS sur cellules vivantes en utilisant un SLM pour l'excitation et une caméra EMCCD pour la détection. La résolution spatiale et temporelle a donc été comparée à celle d'un montage FCS classique.

Le **chapitre 2** était dédié à la méthodologie expérimentale. Le SLM est utilisé pour la création de cinq volumes d'observation indépendants dans l'échantillon. La carte de phase qui y est appliquée est calculée avec l'approche des ondes sphériques superposés [59]. La détection en parallèle est accomplie avec la caméra EMCCD en mode de lecture Crop FvB. En conséquence une résolution temporelle de $14\mu s$ peut être atteinte. Le prix à payer est que la géométrie des spots est confinée sur une ligne. Puisque les intensités des spots ne sont pas uniformes, une correction des contributions croisées entre des spots avoisinants et du bruit de fond, causé par de la lumière non-diffractée, doit être faite.

L'évaluation de la performance du système mFCS était le sujet du **chapitre 3**. Comparée à une expérience FCS classique avec un seul spot et avec une détection par une APD, la résolution temporelle du système mFCS est dégradée ($14\mu s$ vs. $0.2\mu s$). Néanmoins, elle reste parfaitement compatible avec la dynamique de la plupart des protéines cellulaires. Il a été constaté que la largeur latérale des volumes d'observation ω_r est de $0.251\mu m$. La résolution du système mFCS est donc comparable à un système FCS classique où ω_r est $0.211\mu m$. La sensibilité de la caméra EMCCD est proche de celle d'une APD, même si l'APD est légèrement plus performante pour des puissances faibles ou des concentrations de fluorophore faibles. En revanche, en ce qui concerne les intensités de fluorescence élevées, l'emploi d'une caméra EMCCD en tant que détecteur peut être avantageux, car le gain est susceptible d'être ajusté afin d'éviter la satura-

tion et l'endommagement, ce qui n'est pas possible avec une APD. Le domaine d'application du point de vue de la concentration des fluorophores et de la puissance d'excitation a été estimé sur la base de la qualité des fits des fonctions d'autocorrélation mesurées.

Il doit être dit que l'acquisition et le traitement des données est un processus relativement complexe. Il implique le pilotage du SLM, de la caméra EMCCD, de la caméra CCD, du shutter du laser, de la platine du microscope et aussi les corrections des traces temporelles avant les fits des données mesurés. Afin d'améliorer la facilité d'utilisation une interface utilisateur graphique a été développée et le protocole de mesure et d'analyse des données ont été automatisés très largement. En résumé, on peut dire que la résolution spatiale et temporelle du système mFCS est tout à fait adaptée à la mesure de la dynamique d'un facteur de transcription en cellule vivante et que sa sensibilité est comparable à celle d'un système FCS classique. Même si la géométrie des spots est restreinte à une ligne, la technique permet de recueillir des informations spatiales provenant de plusieurs volumes d'observation indépendants. En plus le multiplexage apporte des résultats statistiquement fiables, d'une façon qui économise du temps.

Le deuxième but de ce travail était d'évaluer les changements de dynamique du facteur de transcription HSF1 lors d'un choc thermique, en utilisant le système mFCS. Après une brève description du contexte biologique dans le **chapitre 4**, l'étude de la dynamique de HSF1 est présentée dans le **chapitre 5**. Des mesures de contrôle sur des cellules HELA exprimant la molécule eGFP inerte ont été faites. Aucune différence en matière de concentration et de diffusion de la eGFP inerte entre les cellules non-stressées ($37^{\circ}C$) et stressées ($43^{\circ}C$) a pu être constatée. Le changement de la structure chromatinienne qui accompagne le choc thermique [56] ne semble pas affecter la dynamique de la molécule, peut-être parce que l'effet structural est compensé par la baisse de viscosité du milieu cellulaire dû au changement de la température. De plus, l'homogénéité intracellulaire de la constante de diffusion ne change pas lors d'un choc thermique.

En revanche la concentration et la dynamique de HSF1-eGFP sont clairement impactées par le choc thermique. La chute de concentration peut être attribuée à la trimerisation des complexes HSF1, la relocalisation dans des "nuclear stress bodies" (nSBs, des accumulations sur des répétitions de satellite III) et la liaison

spécifique à des “heat shock elements” (HSEs, des séquences d’ADN spécifiques). Le suivi de l’effet du photoblanchiment lors d’acquisitions consécutives révèle la présence d’une dynamique qui se déroulent à des temps très longs non accessible à la FCS. Malgré tout le choc thermique cause des changements importants dans la dynamique observable par la FCS: Un fit avec un modèle de diffusion-interaction [64] de la fonction d’autocorrélation révèle des événements d’association et dissociation avant et pendant le choc thermique que nous interprétons comme des liaisons non-spécifiques à l’ADN. Les sites de liaison non-spécifiques semblent être distribués d’une façon homogène à travers le noyau. Lors d’un choc thermique des interactions spécifiques se produisent en sus. Ces interactions spécifiques apparaissent de façon moins homogène et peuvent ainsi être interprétées comme la liaison spécifique à des HSEs qui sont éparses dans le génome [55]. Ces observations sont en accord avec des modèles qui suggèrent que la dynamique d’un facteur de transcription est dominé par la diffusion à travers le noyau et des interactions stochastiques non spécifiques, jusqu’à ce que se produise une rencontre avec une site de liaison spécifique [102–107]. Les mêmes résultats ont été obtenus pour deux lignées cellulaires humaines différentes, des cellules U87 et des cellules HELA.

Afin de comprendre le rôle des différents domaines de HSF1 dans la réponse au stress thermique, la dynamique des mutants qui ont subi une délétion a été analysée. En accord avec des observations antérieurs [84, 85] nous avons trouvé que la trimerisation de HSF1 est indispensable pour la liaison spécifique à l’ADN. Le domaine de trimerisation est peut-être même impliqué dans la liaison non-spécifique. Des résultats plus surprenants ont été obtenus pour HSF1 qui a subi une mutation [91] ou une délétion de la domaine de liaison à l’ADN: HSF1 ne forme effectivement pas de nSBs, mais contrairement à ce qu’on pourrait penser, il ne perd pas complètement la capacité de se lier spécifiquement à l’ADN. Dans le cas d’un domaine de liaison à l’ADN muté, HSF1 endogène a été neutralisé pour pouvoir exclure la trimerisation avec le complexe endogène. La délétion d’une partie du domaine de transactivation n’influence pas la formation des nSBs, mais se traduit par un taux de dissociation plus grand. Cela soulève la question de savoir si des protéines qui se lient au domaine de transactivation pourraient être impliquées dans la stabilisation de la liaison entre HSF1 et ADN.

Le troisième but de ce travail concernait le test d'une 32×32 caméra CMOS-SPAD en tant que détecteur pour la mFCS et constitue le sujet de **chapitre 6**. Colyer et al. [47, 48] ont récemment montré la faisabilité des mesures dans des solutions, mais à ma connaissance le système SLM-CMOS-SPAD n'a jamais été utilisé pour des mesures dans des cellules vivantes. De plus des contributions croisées des spots voisins posaient un problème non résolu [48]. En comparaison avec la caméra EMCCD, le détecteur CMOS-SPAD permet d'atteindre une meilleure résolution temporelle ($2\mu s$ vs. $14\mu s$). La résolution spatiale par contre est comparable à celle du système SLM-EMCCD et du système FCS classique, puisque $\omega_r = 0.241\mu m$. Une grille de 3×3 spots a été utilisée pour les mesures CMOS-SPAD. Dans ce cas là, les intensités des spots ne sont pas uniformes et des effets de contributions croisées et de bruit de fond sont plus importants que pour les mesures avec la caméra EMCCD puisque les spots sont plus nombreux et non placés sur une ligne mais à deux dimensions. Il a été montré dans ce travail que les amplitudes des fonctions d'autocorrélation peuvent être corrigées de ces effets. Il y a cependant une limite à cette technique: Plus le nombre des spots est grand, plus de bruit de fond non-corrélé augmente et plus le rapport signal sur bruit est petit.

Afin de démontrer la faisabilité des mesures mFCS en cellules vivantes avec la détection sur le capteur CMOS-SPAD, la dynamique de molécules eGFP inertes dans des cellules HELA a été analysée avec 3×3 spots. La constante de diffusion mesurée est raisonnablement proche des valeurs publiées [94, 119] et de celle trouvée avec la caméra EMCCD qui est 1.4 fois plus grande.

A mon avis, la technique mFCS est une approche très prometteuse pour l'analyse des problèmes biologiques variés. Un point faible, pour l'instant, sont les effets des contributions croisées et du bruit de fond qui apparaissent dans les mesures. Ils peuvent être corrigés, mais ils réduisent quand même le rapport du signal sur bruit. Il pourrait être intéressant de tester des méthodes autre que l'approche des ondes sphériques superposés [59] pour le calcul de la carte de phase appliquée au SLM, afin de réduire la quantité du bruit de fond et d'atteindre des intensités des spots plus uniformes. Une possibilité qui n'a pas encore été implémentée, parce qu'elle exige des modifications importantes du montage expérimental, pourrait être de passer des ondes sphériques aux ondes planes et d'utiliser un algorithme

de Gerchberg-Saxton pondéré [120].

Une application supplémentaire intéressante de la technique mFCS serait de mesurer des écoulements par corrélations croisées entre les volumes. Cette possibilité a été testée rapidement sur des microbilles dans un microcanal (données n'ont pas été montrés) et les résultats étaient encourageants. Comme les flux dans des cellules risquent d'être faibles, la distance entre les volumes d'observation devrait probablement être diminuée. Cela augmenterait certainement la contribution des ailes des spots voisins, qui pourraient être corrigées avec la méthode proposée dans ce travail. La question de savoir si le rapport signal sur bruit, qui devrait diminuer avec des distances plus petites, reste suffisamment grand pour évaluer la dynamique du composant étudié, est intéressante.

En ce moment la limite du système SLM-EMCCD est le confinement de la géométrie des spots sur une ligne (afin de pouvoir utiliser le mode de lecture Crop FvB). Théoriquement il devrait être possible de placer les spots sur des lignes différentes (mais pas dans les mêmes colonnes), de masquer toutes les lignes qui ne sont pas utilisées et de toujours utiliser le mode Crop FvB afin de maintenir la haute résolution temporelle. Pour faire cela il serait intéressant de tester différentes possibilités techniques pour masquer des lignes isolées sur le chip de la caméra EMCCD.

En utilisant le système SLM-CMOS-SPAD il est effectivement possible de détecter en deux dimensions, mais la grande distance entre les pixels limite le nombre des spots qui peuvent être placés à l'intérieur d'une cellule et la géométrie est contrainte puisque des SPADs voisins doivent être employés. Des détecteurs CMOS-SPAD avec des distances petites entre les pixels et la possibilité de transmettre les données rapidement constitueraient ainsi une grande avancé pour les techniques mFCS.

En ce qui concerne l'application biologique de ce travail, il a été montré que la dynamique de HSF1 dans la cellule implique des temps longs aussi bien que des temps courts. Il est ainsi intéressant d'approcher le problème avec une technique complémentaire: La technique "fluorescence recovery after photobleaching" (FRAP). Contrairement à la FCS qui tire parti des petites fluctuations spontanées d'un système en équilibre, le FRAP est basé sur l'étude du retour de

fluorescence d'une espèce dans une région de l'échantillon qui a initialement été photoblanchie et permet ainsi d'évaluer la dynamique a des temps longs.

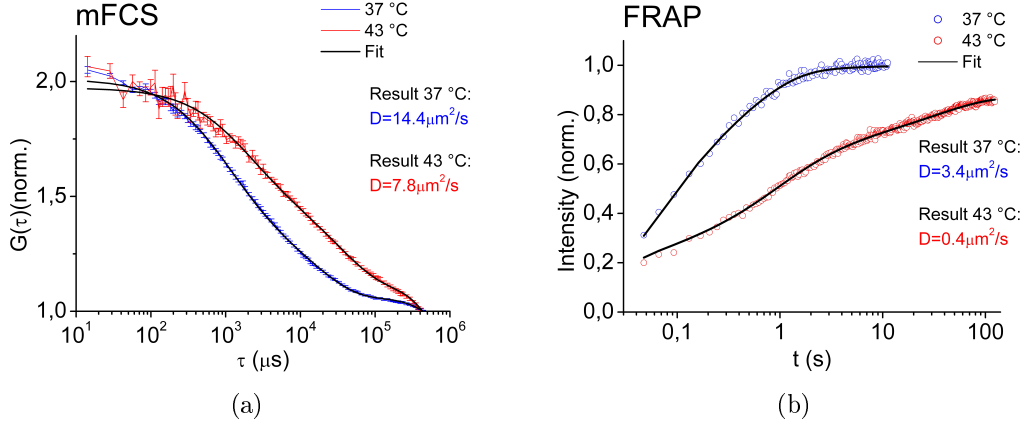


Figure B.3.: Courbes mFCS (a) et FRAP (b) moyennes mesurées dans des cellules HELA-HSF1-eGFP avant (bleu) et pendant un choc thermique (rouge) et fits des données (noir) avec un modèle diffusion-interaction [64]. Des constantes de diffusion D beaucoup plus petites sont obtenues en analysant la dynamique de HSF1 avec le FRAP. (Noter les différentes échelles de temps sur les abscisses.)

Des expériences FRAP en cellules exprimant HSF1-eGFP et des mutants qui ont subi une délétion ont été faites par nos collaborateurs Gaëtan Herbomel et Catherine Souchier à l'Institut Albert Bonniot (IAB) de Grenoble. La figure B.3 montre des courbes mFCS (a) et FRAP (b) mesurées dans des cellules HELA-HSF1-eGFP avant (bleu) et pendant un choc thermique (rouge). Qualitativement le même comportement est observé pour les deux techniques: La dynamique de HSF1 ralentit lors d'un choc thermique. Pourtant, quand les données obtenues par FRAP sont fittées à un modèle de diffusion-interaction [64], analogue à celui utilisé pour les données mFCS (traits noirs), des constantes de diffusion beaucoup plus petites sont obtenues ($D_{FRAP}^{37^\circ C} = 3.4$ et $D_{FRAP}^{43^\circ C} = 0.37$ vs. $D_{mFCS}^{37^\circ C} = 14.4$ et $D_{mFCS}^{43^\circ C} = 7.8$). De plus, la diffusion ne décélère pas de la même proportion lors d'un choc thermique. Tandis que D^{mFCS} est en gros réduit d'un facteur deux, D^{FRAP} est réduite d'un facteur dix.

Le désaccord entre les résultats obtenus avec les deux techniques complémentaires soulève des nouvelles questions intéressantes, auxquelles il n'a pas été possible de

répondre avant la soumission de ce manuscrit. Une approche spécialement prometteuse pour les aborder est le nouveau projet de l'équipe MOTIV: La combinaison de la mFCS et du mFRAP sur un même montage expérimental. Ainsi la couverture d'une grande gamme de temps combinerait les avantages des deux systèmes.

C. Publications and presentations

Publications

- R. Galland, J. Gao, M. Kloster, G. Herbomel, O. Destaing, M. Balland, C. Souchier, Y. Usson, J. Derouard, I. Wang, A. Delon
Multi-confocal fluorescence correlation spectroscopy
Front. Biosci. (Elite Ed.) (2011), Vol. 3, 3, p. 476-488
- D. Tyndall, R. Walker, K. Nguyen, R. Galland, J. Gao, I. Wang, M. Kloster, A. Delon, R. Henderson
Automatic laser alignment for multifocal microscopy using a LCOS SLM and a 32×32 pixel CMOS SPAD array
Proc. of SPIE - OSA Biomedical Optics (2011), Vol. 8086, p. 80860S-80860S-6
- M. Kloster-Landsberg, G. Herbomel, I. Wang, J. Derouard, C. Vourc'h, Y. Usson, C. Souchier, A. Delon
Cellular response to heat shock studied by multiconfocal fluorescence correlation spectroscopy
Biophysical Journal (2012), Vol.103, 6, p. 1110-1119

Presentations on conferences and workshops

- *Multi-confocal fluorescence correlation spectroscopie for parallel multi-spot measurements in living cells*

R.Galland, J.Gao, M. Kloster, G.Herbomel, C. Souchier, Y. Usson, J. Derouard, I. Wang, A. Delon

Talk at the "16th-International Workshop on Single Molecule Spectroscopy and Ultrasensitive Analysis in the Life Sciences" , Berlin, September 15 to 17, 2010

- *Multi-confocal fluorescence correlation spectroscopy and applications to living cells*

R.Galland, J.Gao, M. Kloster, G.Herbomel, C. Souchier, Y. Usson, D.Tyndall, R. K. Hendersson, J. Derouard, I. Wang, A. Delon

Poster presentation at the "Ecole thématique interdisciplinaire en microscopie fonctionnelle en biologie", Seignosse, September 19 to 25, 2010

- *Analysis of HSF1 dynamics during HS using multiconfocal fluorescence correlation spectroscopy*

G. Herbolmel, M. Kloster, I. Wang, E. Col, C. Vourc'h, A. Delon, C. Souchier

Talk at the "Journée de la GDR2588", Toulouse, Mai 30 to 31, 2011

- *Multi-confocal fluorescence correlation spectroscopy: A technique for parallel multi-spot measurements in living cells and its application to the study of cellular response to heat shock*

M. Kloster-Landsberg, G. Herbolmel, Y. Usson, I. Wang, C. Vourc'h, C. Souchier, A. Delon

Poster presentation at the "56th annual meeting of the Biophysical Society", San Diego, February 25 to 29, 2012

Bibliography

- [1] MAGDE, D. ; EISON, E. ; WEBB, W. W.: Thermodynamic fluctuations in a reacting system—measurement. In: *Physical Review Letters* 29 (1972), no. 11, p. 705–708
- [2] KOPPEL, D. E. ; AXELROD, D. ; SCHLESSINGER, J. ; ELSON, E. L. ; WEBB, W. W.: Dynamics of fluorescence marker concentration as a probe of mobility. In: *Biophysical Journal* 16 (1976), p. 1315–1329
- [3] RIGLER, R. ; WIDENGREN, J.: Ultrasensitive detection of single molecules by fluorescence correlation spectroscopy. In: *Bioscience* 3 (1990), p. 180–183
- [4] QIAN, H. ; ELSON, E. L.: Analysis of confocal laser-microscope optics for 3-D fluorescence correlation spectroscopy. In: *Applied Optics* 30 (1991), no. 10, p. 1185–1195
- [5] RIGLER, R. ; METS, Ü. ; WIDENGREN, J. ; KASK, P.: Fluorescence correlation spectroscopy with high count rate and low background: analysis of translational diffusion. In: *Eur. Biophys. J.* 22 (1993), p. 169–175
- [6] V.VUKOJEVIĆ ; PRAMANIK, A. ; T.YAKOVLEVA ; RIGLER, R. ; L.TERENIUS ; BAKALKIN, G.: Study of molecular events in cells by fluorescence correlation spectroscopy. In: *CMLS and Cell. Mol. Life Sci.* 62 (2005), p. 535–550
- [7] DUNDR, M. ; MISTELI, T.: Functional architecture in the cell nucleus. In: *Biochem. J.* 356 (2001), p. 297–310

- [8] SCHEER, U. ; HOCK, R.: Structure and function of the nucleolus. In: *Curr. Opin. Cell Biol.* 11 (1999), p. 385–390
- [9] MISTELI, T.: Cell Biology of transcription and pre-mRNA splicing : nuclear architecture meets nuclear function. In: *J. Cell Sci.* 113 (2000), p. 1841–1849
- [10] GALL, J. G.: Cajal Bodies : the first 100 years. In: *Annu. Rev. Cell. Dev. Biol.* 16 (2000), p. 273–300
- [11] FERREIRA, J. ; PAOLELLA, G. ; RAMOS, C. ; LAMOND, A. I.: Spatial organization of large-scale chromatin domains in the nucleus: A magnified view of single chromosome territories. In: *The Journal of Cell Biology* 139 (1997), no. 7, p. 1597–1610
- [12] CREMER, T. ; CREMER, C.: Chromosome Territories and Nuclear Architecture and gene regulation in mammalian cells. In: *Nature Reviews Genetics* 2 (2001), p. 292–301
- [13] MISTELI, T.: Concepts in nuclear architecture. In: *BioEssays* 27 (2005), p. 477–487
- [14] JAMESON, D. M. ; ROSS, J. A.: Fluorescence fluctuation spectroscopy: ushering in a new age of enlightenment for cellular dynamics. In: *Biophys Rev.* 1 (2009), no. 3, p. 105–118
- [15] PETERSEN, N. O. ; HÖDDELIUS, P. L. ; WISEMAN, P. W. ; SEGER, O. ; MAGNUSSON, K.-E.: Quantitation of membrane receptor distributions by image correlation spectroscopy: Concept and application. In: *Biophysical Journal* 65 (1993), p. 1135–1146
- [16] WISEMAN, P. W. ; PETERSEN, N. O.: Image correlation spectroscopy. II. Optimization for ultrasensitive detection of preexisting platelet-derived growth factor- β receptor oligomers on intact cells. In: *Biophysical Journal* 76 (1999), p. 963–977

- [17] WISEMAN, P. W. ; BROWN, C. M. ; WEBB, D. J. ; HEBERT, B. ; JOHNSON, N. L. ; SQUIER, J. A. ; ELLISMAN, M. H. ; HORWITZ, A. F.: Spatial mapping of integrin interactions and dynamics during cell migration by image correlation microscopy. In: *Journal of Cell Science* 117 (2004), no. 23, p. 5521–5534
- [18] DIGMAN, M. A. ; SENGUPTA, P. ; WISEMAN, P. W. ; BROWN, C. M. ; HORWITZ, A. R. ; GRATTON, E.: Fluctuation correlation spectroscopy with a laser-scanning microscope: Exploiting the hidden time structure. In: *Biophysical Journal* 88 (2005), no. 5, p. L33–L36
- [19] DIGMAN, M. A. ; BROWN, C. M. ; SENGUPTA, P. ; WISEMAN, P. W. ; HORWITZ, A. R. ; GRATTON, E.: Measuring fast dynamics in solutions and cells with a laser scanning microscope. In: *Biophysical Journal* 89 (2005), no. 2, p. 1317–1327
- [20] GIELEN, E. ; SMISDOM, N. ; CLERCQ, B. D. ; VANDEVEN, M. ; GIJSBERS, R. ; DEBYSER, Z. ; RIGO, J.-M. ; HOFKENS, J. ; ENGELBORGHES, Y. ; AMELOOT, M.: Diffusion of myelin oligodendrocyte glycoprotein in living OLN-93 cells investigated by raster-scanning image correlation spectroscopy (RICS). In: *J. Fluoresc.* 18 (2008), p. 813–819
- [21] DIGMAN, M. A. ; WISEMAN, P. W. ; HORWITZ, A. R. ; GRATTON, E.: Detecting protein complexes in living cells from laser scanning confocal image sequences by the cross correlation raster image spectroscopy method. In: *Biophysical Journal* 96 (2009), no. 2, p. 707–716
- [22] GIELEN, E. ; SMISDOM, N. ; VANDEVEN, M. ; CLERCQ, B. D. ; GRATTON, E. ; DIGMAN, M. ; RIGO, J.-M. ; HOFKENS, J. ; ENGELBORGHES, Y. ; AMELOOT, M.: Measuring diffusion of lipid-like probes in artificial and natural membranes by raster image correlation spectroscopy (RICS): use of a commercial laser-scanning microscope with analog detection. In: *Langmuir* 25 (2009), no. 9, p. 5209–5218

- [23] GRÖNER, N. ; CAPOULADE, J. ; CREMER, C. ; WACHSMUTH, M.: Measuring and imaging diffusion with multiple scan speed image correlation spectroscopy. In: *Optics Express* 18 (2010), no. 20, p. 21225–21237
- [24] BROWN, C. M. ; DALAL, R. B. ; HEBERT, B. ; DIGMAN, M. A. ; HORWITZ, A. R. ; GRATTON, E.: Raster image correlation spectroscopy (RICS) for measuring fast protein dynamics and concentrations with a commercial laser scanning confocal microscope. In: *Journal of Microscopy* 229 (2007), p. 78–91
- [25] J.CAPOULADE ; WACHSMUTH, M. ; HUFNAGEL, L. ; KNOP, M: Quantitative fluorescence imaging of protein diffusion and interaction in living cells. In: *Nature Biotechnology* 29 (2011), p. 835–839
- [26] PETERSEN, N. O.: Scanning fluorescence correlation spectroscopy. I. Theory and simulation of aggregation measurements. In: *Biophysical Journal* 49 (1986), p. 809–815
- [27] PETERSEN, N. O. ; JOHNSON, D. C. ; SCHLESINGER, M. J.: Scanning fluorescence correlation spectroscopy. II. Application to virus glycoprotein aggregation. In: *Biophysical Journal* 49 (1986), p. 817–820
- [28] RIES, J. ; SCHWILLE, P.: Studying slow membrane dynamics with continuous wave scanning fluorescence correlation spectroscopy. In: *Biophysical Journal* 91 (2006), no. 5, p. 1915–1924
- [29] PAN, X. ; YU, H. ; SHI, X. ; KORZH, V. ; WOHLAND, T.: Characterization of flow direction in microchannels and zebrafish blood vessels by scanning fluorescence correlation spectroscopy. In: *Journal of Biomedical Optics* 12 (2007), no. 1, p. 014034–1–014034–10
- [30] RIES, J. ; CHIANTIA, S. ; SCHWILLE, P.: Accurate determination of membrane dynamics with line-scan FCS. In: *Biophysical Journal* 96 (2009), no. 5, p. 1999–2008

- [31] RUAN, Q. ; CHENG, M. A. ; LEVI, M. ; GRATTON, E. ; MANTULIN, W. W.: Spatial-temporal studies of membrane dynamics: Scanning fluorescence correlation spectroscopy (SFCS). In: *Biophysical Journal* 87 (2004), no. 2, p. 1260–1267
- [32] SKINNER, J. P. ; CHEN, Y. ; MÜLLER, J. D.: Position-sensitive scanning fluorescence correlation spectroscopy. In: *Biophysical Journal* 89 (2005), no. 2, p. 1288–1301
- [33] PETRÁŠEK, Z. ; SCHWILLE, P.: Precise measurement of diffusion coefficients using scanning fluorescence correlation spectroscopy. In: *Biophysical Journal* 94 (2008), p. 1437–1448
- [34] PETRÁŠEK, Z. ; DERENKO, S. ; SCHWILLE, P.: Circular scanning fluorescence correlation spectroscopy on membranes. In: *Optics Express* 19 (2011), no. 25, p. 25006–25021
- [35] R. MACHÁŇ, M. H.: Recent developments in fluorescence correlation spectroscopy for diffusion measurements in planar lipid membranes. In: *Int. J. Mol. Sci.* 11 (2010), p. 427–457
- [36] SISAN, D. R. ; AREVALO, R. ; GRAVES, C. ; MCALLISTER, R. ; URBACH, J. S.: Spatially resolved fluorescence correlation spectroscopy using a spinning disk confocal microscope. In: *Biophysical Journal* 91 (2006), no. 11, p. 4241–4252
- [37] NEEDLEMAN, D. J. ; XU, Y. ; MITCHISON, T. J.: Pin-Hole array correlation imaging: Highly parallel fluorescence correlation spectroscopy. In: *Biophysical Journal* 96 (2009), no. 12, p. 5050–5059
- [38] OH, D. ; ZIDOVSKA, A. ; XU, Y. ; NEEDLEMAN, D. J.: Development of time-integrated multipoint moment analysis for spatially resolved fluctuation spectroscopy with high time resolution. In: *Biophysical Journal* 101 (2011), no. 6, p. 1546–1554

- [39] REICHERTER, M. ; HAIST, T. ; WAGEMANN, E. U. ; TIZIANI, H. J.: Optical particle trapping with computer-generated holograms written on a liquid-crystal display. In: *Optics Letters* 24 (1999), no. 9, p. 608–610
- [40] LIESENER, J. ; REICHERTER, M. ; HAIST, T. ; TIZIANI, H. J.: Multi-functional optical tweezers using computer-generated holograms. In: *Optics Communications* 185 (2000), no. 1-3, p. 77–82
- [41] CURTIS, J. E. ; KOSS, B. A. ; GRIER, D. G.: Dynamic holographic optical tweezers. In: *Optics Communications* 207 (2002), no. 1-6, p. 169–175
- [42] LOVE, G. D.: Wave-front correction and production of Zernike modes with a liquid-crystal spatial light modulator. In: *Applied Optics* 36 (1997), no. 7, p. 1517–1524
- [43] BLANCQUAERT, Y. ; GAO, J. ; DEROUARD, J. ; DELON, A.: Spatial fluorescence cross correlation spectroscopy by means of a spatial light modulator. In: *J. Biophoton* 1 (2008), p. 408–418
- [44] BURKHARDT, M. ; SCHWILLE, P.: Electron multiplying CCD based detection for spatially resolved fluorescence correlation spectroscopy. In: *Optics Express* 14 (2006), no. 12, p. 5013–5020
- [45] B. KANNAN, J.Y. H. ; LIU, P. ; MARUYAMA, I. ; DING, J. L. ; WOHLAND, T.: Electron multiplying charge-coupled device camera based fluorescence correlation spectroscopy. In: *Anal. Chem.* 78 (2006), no. 10, p. 3444–3451
- [46] MATSUMOTO, M. ; SUGIURA, T. ; MINATO, K.: Spatially resolved fluorescence correlation spectroscopy based on electron multiplying CCD. In: *SPIE-OSA* 6630 (2007), p. 663017–1–663017–8
- [47] COLYER, R. A. ; SCALIA, G. ; RECH, I. ; GULINATTI, A. ; GHIONI, M. ; COVA, S. ; WEISS, S. ; MICHALET, X.: High-throughput FCS using a LCOS spatial light modulator and a 8 x 1 SPAD array. In: *Biomedical Optics Express* 1 (2010), no. 5, p. 1408–1431

- [48] COLYER, R. A. ; SCALIA, G. ; VILLA, F. A. ; GUERRIERI, F. ; TISA, S. ; ZAPPA, F. ; COVA, S. ; WEISS, S. ; MICHALET, X.: Ultra high-throughput single molecule spectroscopy with a 1024 pixel SPAD. In: *Proc. of SPIE* 7905 (2011), p. 790503–1–790503–8
- [49] SARGE, K. D. ; MURPHY, S. P. ; MORIMOTO, R. I.: Activation of heat shock gene transcription by heat shock factor 1 involves oligomerization and acquisition of DNA-binding activity and nuclear localization and can occur in the absence of stress. In: *Molecular and Cellular Biology* 13 (1993), no. 3, p. 1392–1407
- [50] WESTWOOD, J. T. ; WU, C.: Activation of drosophila heat shock factor: Conformational change associated with a monomer-to-trimer transition. In: *Molecular and Cellular Biology* 13 (1993), no. 6, p. 3481–3486
- [51] LARSON, J. S. ; SCHUETZ, T. J. ; KINGSTON, R. E.: Activation in vitro of sequence-specific DNA binding by a human regulatory factor. In: *Nature* 335 (1988), p. 372–375
- [52] AMIN, J. ; ANANTHAN, J. ; VOELLMY, R.: Key features of heat shock regulatory elements. In: *Molecular and Cellular Biology* 8 (1988), no. 9, p. 3761–3769
- [53] PERISIC, O. ; XIAO, H. ; LIS, J. T.: Stable binding of Drosophila heat shock factor to head-to-head and tail-to-tail repeats of a conserved 5 bp recognition unit. In: *Cell* 59 (1989), no. 5, p. 797–806
- [54] ABRAVAYA, K. ; PHILLIPS, B. ; MORIMOTO, R. I.: Heat sShock-induced interactions of heat shock transcription factor and the human hsp70 promoter examined by in vivo footprinting. In: *Molecular and Cellular Biology* 11 (1991), no. 1, p. 586–592
- [55] TRINKLEIN, N. D. ; MURRAY, J. I. ; HARTMAN, S. J. ; BOTSTEIN, D. ; MYERS, R. M.: The role of heat shock transcription factor 1 in the genome-wide regulation of the mammalian heat shock response. In: *Molecular Biology of the Cell* 15 (2004), p. 1254–1261

- [56] FRITAH, S. ; COL, E. ; BOYAULT, C. ; GOVIN, J. ; SADOUL, K. ; CHIOCCA, S. ; CHRISTIANS, E. ; KHOCHBIN, S. ; JOLLY, C. ; VOURC'H, C.: Heat-shock factor 1 controls genome-wide acetylation in heat-shocked cells. In: *Molecular Biology of the Cell* 20 (2009), p. 4976–4984
- [57] HAMAMATSU PHOTONICS K. K. (Hrsg.): *LCOS-SLM and X10468 series (X10468-01,-02,-03,-04) Hardware instruction manual*. Doc. Version 2.7. 5000 Hirakuchi and Hamakita-ku and Hamamatsu City and 434-8601 Japan: Hamamatsu Photonics K. K.
- [58] K., Hamamatsu Photonics K. ; DIVISION, Solid S. ; ICHINO-CHO, 1126-1 ; HIGASHI-KU ; CITY, Hamamatsu ; JAPAN, 435-8558: *LCOS-SLM X10468 series*. http://sales.hamamatsu.com/assets/pdf/parts_X/x10468_series_kacc1172e07.pdf. Version: December 2010
- [59] COJOC, D. ; FABRIZIO, E. D. ; BUSINARO, L. ; CABRINI, S.: Spherical-based approach to design diffractive optical elements. In: *Proc. of SPIE* 5227 (2003), p. 123–131
- [60] ANDOR TECHNOLOGY (Hrsg.): *iXon^{EM+} and Hardware guide*. Version 1.2. : Andor Technology, 2008
- [61] WIDENGREN, J. ; METS, Ü. ; RIGLER, R.: Fluorescence correlation spectroscopy of triplet states in solution: A theoretical and experimental study. In: *J. Phys. Chem.* 99 (1995), p. 13368–13379
- [62] LAGARIAS, J. C. ; REEDS, J. A. ; WRIGHT, M. H. ; WRIGHT, P. E.: Convergence properties of the Nelder-Mead simplex method in low dimensions. In: *SIAM J. Optim.* 9 (1998), no. 1, p. 112–147
- [63] ORIGINLAB CORPORATION (Hrsg.): *Origin Help*. Version 6.1. One Roundhouse Plaza and Suite 303 and Northampton and MA 01060 and USA: OriginLab Corporation
- [64] MICHELMAN-RIBEIRO, A. ; MAZZA, D. ; ROSALES, T. ; STASEVICH, T. J. ; BOUKARI, H. ; RISHI, V. ; VINSON, C. ; KNUTSON, J. R. ; MCNALLY,

- J. G.: Direct measurement of association and dissociation rates of DNA binding in live cells by fluorescence correlation spectroscopy. In: *Biophysical Journal* 97 (2009), no. 1, p. 337–346
- [65] MÜLLER, C. B. ; LOMAN, A. ; PACHECO, V. ; KOBERLING, F. ; WILLBOLD, D. ; RICHTERING, W. ; ENDERLEIN, J.: Precise measurement of diffusion by multi-color dual-focus fluorescence correlation spectroscopy. In: *Europhys. Lett.* 83 (2008), no. 4, p. 46001–p1–46001–p5
- [66] KAPUSTA, P.: *Absolute diffusion coefficients: Compilation of reference data for FCS calibration*. Rev. 1. Rudower Chaussee 29 (IGZ) and 12489 Berlin and Germany: PicoQuant GmbH, 2010
- [67] HINK, M. A. ; GRIEP, R. A. ; BORST, J. W. ; HOEK, A. van ; EPPINK, M. H. M. ; SCHOTS, A. ; VISSER, A. J. W. G.: Structural dynamics of green fluorescent protein alone and fused with a single chain Fv protein. In: *J. Biol. Chem.* 275 (2000), no. 23, p. 17556–17560
- [68] WU, C.: Heat shock transcription factors: Structure and regulation. In: *Annu. Rev. Cell Dev. Biol.* 11 (1995), p. 441–469
- [69] ANCKAR, J. ; SISTONEN, L.: Regulation of HSF1 function in the heat stress response: Implications in aging and disease. In: *Annu. Rev. Biochem.* 80 (2011), p. 1089–1115
- [70] MERCIER, P. A. ; WINEGARDEN, N. A. ; WESTWOOD, J. T.: Human heat shock factor 1 is predominantly a nuclear protein before and after heat stress. In: *Journal of Cell Science* 112 (1999), p. 2765–2774
- [71] LINDQUIST, S. ; CRAIG, E. A.: The heat-shock proteins. In: *Annu. Rev. Genet.* 22 (1988), p. 631–677
- [72] SPRADLING, A. ; PENMAN, S. ; PARDUE, M. L.: Analysis of drosophila mRNA by in situ hybridization: sequences transcribed in normal and heat shocked cultured cells. 4 (1975), no. 4, p. 395–404

- [73] FINDLY, R. C. ; PEDERSON, T.: Regulated transcription of the genes for actin and heat-shock proteins in cultured *Drosophila* cells. In: *J Cell Biol.* 88 (1981), no. 2, p. 323–328
- [74] HIGASHIKUBO, R. ; ROTI, J. L. R.: Alterations in nuclear protein mass and macromolecular synthesis following heat shock. In: *Radiat Res.* 134 (1993), no. 2, p. 193–201
- [75] HENDRICK, J. P. ; HARTL, F.-U.: Molecular chaperone functions of heat-shock proteins. In: *Annu. Rev. Biochem.* 62 (1993), p. 349–384
- [76] LINDQUIST, S.: The heat-shock response. In: *Ann. Rev. Biochem.* 55 (1986), p. 1151–1191
- [77] MORIMOTO, R. I. ; KROEGER, P. E. ; COTTO, J. J.: The transcriptional regulation of heat shock genes: a plethora of heat shock factors and regulatory conditions. In: *EXS.* 77 (1996), p. 139–163
- [78] MORIMOTO, R. I.: Regulation of the heat shock transcriptional response: cross talk between a family of heat shock factors and molecular chaperones and and negative regulators. In: *Genes & Development* 12 (1998), p. 3788–3796
- [79] JOLLY, C. ; KONECNY, L. ; GRADY, D. L. ; KUTSKOVA, Y. A. ; COTTO, J. J. ; MORIMOTO, R. I. ; VOUREC'H, C.: In vivo binding of active heat shock transcription factor 1 to human chromosome 9 heterochromatin during stress. In: *The Journal of Cell Biology* 156 (2002), no. 5, p. 775–781
- [80] COTTO, J. J. ; FOX, S. G. ; MORIMOTO, R. I.: HSF1 granules: a novel stress-induced nuclear compartment of human cells. In: *Journal of Cell Science* 110 (1997), p. 2925–2934
- [81] BIAMONTI, G. ; VOUREC'H, C.: Nuclear stress bodies. In: *Cold Spring Harb Perspect Biol.* 2 (2010), no. 6

- [82] JOLLY, C. ; USSON, Y. ; MORIMOTO, R. I.: Rapid and reversible relocalization of heat shock factor 1 within seconds to nuclear stress granules. In: *Proc. Natl. Acad. Sci.* 96 (1999), p. 6769–6774
- [83] ASHBURNER, M.: Patterns of puffing activity in the salivary gland chromosomes of drosophila. In: *Chromosoma* 31 (1970), p. 356–376
- [84] DREES, B. L. ; GROTKOPP, E. K. ; NELSON, H. C. M.: The GCN4 leucine zipper can functionally substitute for the heat shock transcription factor's trimerization domain. In: *J. Mol. Biol.* 273 (1997), p. 61–74
- [85] SORGER, P. K. ; NELSON, H. C. M.: Trimerization of a yeast transcriptional activator via a coiled-coil motif. In: *Cell* 59 (1989), p. 807–813
- [86] PETERANDERL, R. ; NELSON, H. C.: Trimerization of the heat shock transcription factor by a triple-stranded alpha-helical coiled-coil. In: *Biochemistry* 31 (1992), no. 48, p. 12272–6
- [87] PETERANDERL, R. ; RABENSTEIN, M. ; SHIN, Y.-K. ; LIU, C. W. ; WEMMER, D. E. ; KING, D. S. ; NELSON, H. C. M.: Biochemical and biophysical characterization of the trimerization domain from the heat shock transcription factor. In: *Biochemistry* 38 (1999), no. 12, p. 3559–3569
- [88] RABINDRAN, S.K. ; HAROUN, R.I. ; CLOS, J. ; WISNIEWSKI, J. ; WU, C.: Regulation of heat shock factor trimer formation: role of a conserved leucine zipper. In: *Science* 259 (1993), no. 5092, p. 230–234
- [89] GREEN, M. ; SCHUETZ, T. J. ; SULLIVAN, E. K. ; KINGSTON, R. E.: A heat shock-responsive domain of human HSF1 that regulates transcription activation domain function. In: *Molecular and Cellular Biology* 15 (1995), no. 6, p. 3354–3362
- [90] NEWTON, E. M. ; KNAUF, U. ; GREEN, M. ; KINGSTON, R. E.: The regulatory domain of human heat shock factor 1 is sufficient to sense heat stress. In: *Molecular and Cellular Biology* 16 (1996), no. 3, p. 839–846

- [91] WESTERHEIDE, S. D. ; ANCKAR, J. ; JR., S. M. S. ; SISTONEN, L. ; MORIMOTO, R. I.: Stress-inducible regulation of heat shock factor 1 by the deacetylase SIRT1. In: *Science* 323 (2009), p. 1063–1066
- [92] HAMILTON, A. J. ; BAULCOMBE, D. C.: A species of small antisense RNA in posttranscriptional gene silencing in plants. In: *Science* 286 (1999), p. 950–952
- [93] ELBASHIR, S. M. ; HARBORTH, J. ; LENDECKEL, W. ; YALCIN, A. ; WEBER, K. ; TUSCHL, T.: Duplexes of 21-nucleotide RNAs mediate RNA interference in cultured mammalian cells. In: *Nature* 411 (2001), p. 494–498
- [94] DROSS, N. ; SPRIET, C. ; ZWERGER, M. ; MÜLLER, G. ; WALDECK, W. ; LANGOWSKI, J.: Mapping eGFP oligomer mobility in living cell nuclei. In: *PLoS ONE* 4 (2009), no. 4, p. e5041
- [95] OH, D. ; ZIDOVSKA, A. ; XU, Y. ; NEEDLEMAN, D. J.: Development of time-integrated multipoint moment analysis for spatially resolved fluctuation spectroscopy with high time resolution. In: *Biophysical Journal* 101 (2011), no. 6, p. 1546–1554
- [96] SEKSEK, O. ; BIWERSI, J. ; VERKMAN, A.S.: Translational diffusion of macromolecule-sized solutes in cytoplasm and nucleus. In: *The Journal of Cell Biology* 138 (1997), no. 1, p. 131–142
- [97] ALBERTS, B. ; BRAY, D. ; HOPKIN, K. ; JOHNSON, A. ; LEWIS, J. ; RAFF, M. ; ROBERTS, K. ; WALTER, P.: *Essential cell biology*. New York and USA : Garland Science, 2010
- [98] GÖRISCH, S. M. ; WACHSMUTH, M. ; TÓTH, K. F. ; LICHTER, P. ; RIPPE, K.: Histone acetylation increases chromatin accessibility. In: *Journal of Cell Science* 118 (2005), no. 24, p. 5825–5834
- [99] LEE, D. Y. ; HAYES, J. J. ; PRUSS, D. ; WOLFFE, A. P.: A positive role for histone acetylation in transcription factor access to nucleosomal DNA. In: *Cell* 72 (1993), no. 1, p. 73–84

-
- [100] VETTESE-DADEY, M. ; A.GRANT, P. ; HEBBES, T. R. ; CRANE-ROBINSON, C. ; ALLIS, C.David ; L.WORKMAN, J.: A positive role for histone acetylation in transcription factor access to nucleosomal DNA. In: *The EMBO Journal* 15 (1996), no. 10, p. 2508–2518
- [101] L. SISTONEN, K. D. S. ; MORIMOTO, R. I.: Human heat shock factors 1 and 2 are differentially activated and can synergistically induce hsp70 gene transcription. In: *Molecular and Cellular Biology* 14 (1994), no. 3, p. 2087–2099
- [102] HAGER, G. L. ; MCNALLY, J. G. ; MISTELI, T.: Transcription Dynamics. In: *Molecular Cell* 35 (2009), p. 741–753
- [103] GORSKI, S. A. ; DUNDR, M. ; MISTELI, T.: The road much traveled: trafficking in the cell nucleus. In: *Current Opinion in Cell Biology* 18 (2006), p. 284–290
- [104] MISTELI, T.: Protein dynamics: Implications for nuclear architecture and gene expression. In: *Science* 291 (2001), p. 843–847
- [105] MUELLER, F. ; WACH, P. ; MCNALLY, J. G.: Evidence for a common mode of transcription factor interaction with chromatin as revealed by improved quantitative fluorescence recovery after photobleaching. In: *Biophysical Journal* 94 (2008), no. 8, p. 3323–3339
- [106] PHAIR, R. D. ; SCAFFIDI, P. ; ELBI, C. ; VECEROVÀ, J. ; DEY, A. ; OZATO, K. ; BROWN, D. T. ; HAGER, G. ; BUSTIN, M.I ; MISTELI, T.: Global nature of dynamic protein-chromatin interactions in vivo: Three-dimensional genome scanning and dynamic interaction networks of chromatin proteins. In: *Molecular and Cellular Biology* 24 (2004), no. 14, p. 6393–6402
- [107] SPRAGUE, B. L. ; PEGO, R. L. ; STAVREVA, D. A. ; MCNALLY, J. G.: Analysis of binding reactions by fluorescence recovery after photobleaching. In: *Biophysical Journal* 86 (2004), no. 6, p. 3473–3495
- [108] VUKOJEVIĆ, V. ; PAPADOPOULOS, D. K. ; TERENIUS, L. ; GEHRING, W. J. ; RIGLER, R.: Quantitative study of synthetic Hox transcription

- factor–DNA interactions in live cells. In: *PNAS* 107 (2010), no. 9, p. 4093–4098
- [109] BOELLMANN, F. ; GUETTOUCHE, T. ; GUO, Y. ; FENNA, M. ; MNAYER, L. ; VOELLMY, R.: DAXX interacts with heat shock factor 1 during stress activation and enhances its transcriptional activity. In: *Proc Natl Acad Sci USA* 101 (2004), no. 12, p. 4100–4105
- [110] HONG, S. ; KIM, S. H. ; HEO, M. A. ; CHOI, Y. H. ; PARK, M. J. ; YOO, M. A. ; KIM, H. D. ; KANG, H. S. ; CHEONG, J.: Coactivator ASC-2 mediates heat shock factor 1-mediated transactivation dependent on heat shock. In: *FEBS Letters* 559 (2004), p. 165–170
- [111] COREY, L. L. ; WEIRICH, C. S. ; BENJAMIN, I. J. ; KINGSTON, R. E.: Localized recruitment of a chromatin-remodeling activity by an activator in vivo drives transcriptional elongation. In: *Genes & Development* 17 (2003), p. 1392–1401
- [112] RICHARDSON, J. ; WALKER, R. ; GRANT, L. ; STOPPA, D. ; BORGHETTI, F. ; CHARBON, E. ; GERSBACH, M. ; HENDERSON, R. K.: A 32×32 50ps resolution 10 bit time to digital converter array in 130nm CMOS for time correlated imaging. In: *IEEE 2009 Custom Intergrated Circuits Conference (CICC)* (2009), p. 6–3–1 – 6–3–4
- [113] TYNDALL, D. ; WALKER, R. ; NGUYEN, K. ; GALLAND, R. ; GAO, J. ; WANG, I. ; KLOSTER, M. ; DELON, A. ; HENDERSON, R.: Automatic laser alignment for multifocal microscopy using a LCOS SLM and a 32×32 pixel CMOS SPAD array. In: *Proc. of SPIE - OSA Biomedical Optics* 8086 (2011), p. 80860S–1 – 80860S–6
- [114] RICHARDSON, J. A. ; GRANT, L. A. ; HENDERSON, R. K.: Low dark count single-photon avalanche diode structure compatible with standard nanometer scale CMOS technology. In: *IEEE Photonics Technology Letters* 21 (2009), no. 14, p. 1020–1022
- [115] TYNDALL, D.: personal communication, 2012

- [116] KOPPEL, D. E.: Statistical accuracy in fluorescence correlation spectroscopy. In: *Physical Review A* 10 (1974), no. 6, p. 1938–1945
- [117] HESS, S. T. ; WEBB, W. W.: Focal volume optics and experimental artifacts in confocal fluorescence correlation spectroscopy. In: *Biophysical Journal* 83 (2002), no. 4, p. 2300–2317
- [118] BUSCHMANN, V. ; KRÄMER, B. ; KOBERLING, F. ; MACDONALD, R. ; RÜTTINGER, S.: *Quantitative FCS: Determination of the confocal volume by FCS and bead scanning with the Micr Time 200*. Rudower Chaussee 29 (IGZ) and 12489 Berlin and Germany: PicoQuant GmbH, 2009
- [119] Y.CHEN ; MÜLLER, J. D. ; RUAN, Q. ; GRATTON, E.: Molecular brightness characterization of EGFP in vivo by fluorescence fluctuation spectroscopy. In: *Biophysical Journal* 82 (2002), no. 1, p. 133–144
- [120] LEONARDO, R. D. ; IANNI, F. ; RUOCCO, G.: Computer generation of optimal holograms for optical trap arrays. In: *Optics Express* 15 (2007), no. 4, p. 1913–1922

List of Figures

1.1.	Principle of the FCS technique.	1
1.2.	Schematics illustrating the originally intended mFCS technique.	4
2.1.	Scheme of the mFCS setup.	9
2.2.	Schematics of the SLM consisting of a layer of parallel aligned nematic liquid crystals.	12
2.3.	Schematics illustrating the geometric relation between one pixel of the SLM and the m^{th} spot in the SLM focal plane and example for a phase function applied to the SLM.	13
2.4.	Schematic representation of an EMCCD camera pixel playing the role of a pinhole for confocal detection, schematics illustrating the functioning of an EMCCD camera in the frame transfer mode [60] and scheme of the mask in the EMCCD detection pathway.	15
2.5.	Full image acquisition on the EMCCD camera and wide field acquisition on the CCD camera.	18
2.6.	Screenshot of the graphical user interface developed in MATLAB.	19
2.7.	Graphics describing the data post processing.	20
2.8.	Intensity profile on the last line of the EMCCD camera.	22
2.9.	Autocorrelation functions resulting from an mFCS experiment with five spots without correction for crosstalk and background.	23
2.10.	Autocorrelation functions resulting from an mFCS experiment with five spots with correction for crosstalk and background done in the post-processing.	23
2.11.	Estimated number of molecules for five spots by varying the distances in between the spots.	24

3.1. Autocorrelation functions measured with the different combinations of excitation and detection pathways.	32
3.2. Performance of the APD and the EMCCD camera as a detector for FCS experiments at different excitation powers and fluorophor concentrations.	33
3.3. Average number of molecules and diffusion times measured in solutions of Dextran-Rhodamine Green in a range of concentrations from 400nM-1.1 μ M.	36
3.4. Average number of molecules and diffusion times estimated from FCS experiments when shifting a spot away from the optical axes.	38
3.5. Average number of molecules and diffusion times estimated from FCS measurements in a single spot and in the central spot of five spots.	39
3.6. Diffusion times and count rates per molecule estimated from FCS measurements in an aqueous solution of eGFP at different temperatures.	40
4.1. Schematics depicting the heat shock response in eukaryotic cells.	43
4.2. Structure of heat shock factor 1 (HSF1) [68, 69].	45
4.3. Schematics of the HSF1 deletion mutants.	46
5.1. An example for five individual autocorrelation functions measured in one HELA-eGFP cell.	49
5.2. Mean over 38 autocorrelation functions measured in five spots located in the nuclei of 5 HELA-eGFP cells at 37°C and 43°C.	50
5.3. Color maps depicting the relation between the diffusion time in a spot measured in cell measurements and in the corresponding calibration measurement in solution.	52
5.4. An example for an U87-HSF1-eGFP cell in a non heat-shocked and heat-shocked state with the position of the five observation volumes.	54
5.5. Mean over a subset of 36 autocorrelation functions at 37°C and 31 autocorrelation functions at 43°C in U87-HSF1-eGFP cells.	55

5.6.	Mean normalized intensity in 45 spots in the two series of five acquisitions at $37^{\circ}C$ and at $43^{\circ}C$ for U87-HSF1-eGFP cells and for HELA-eGFP cells.	56
5.7.	Schematics illustrating the hypothetical diffusion and interaction of HSF1 with non-specific and specific binding sites [102–107]. . .	60
5.8.	Wide field images of a HELA cell expressing the full-length or mutated HSF1-eGFP before and during heat shock.	74
5.9.	Mean autocorrelation functions for the measurements in HELA cells expressing the full-length or mutated HSF1-eGFP.	75
6.1.	CMOS-SPAD detector, pictures by courtesy of D. Tyndall	77
6.2.	Distribution of the dark count rates of the 32×32 SPADs.	78
6.3.	Surface plot of the intensity distribution in and in the vicinity of the 3×3 spots.	80
6.4.	Intensity distribution in and in the vicinity of 3×3 spots and fit with a nine-peak Lorentz function.	82
6.5.	The SPAD detector area in the plane of the CCD camera.	83
6.6.	Autocorrelation functions measured for the different combinations of excitation and detection pathways.	84
6.7.	Average number of molecules and diffusion times in solutions of Dextran-Rhodamine Green in a range of concentrations from 50nM-700nM.	85
6.8.	Average number of molecules and diffusion times estimated from FCS experiments when shifting one spot away from the optical axes.	86
6.9.	Average number of molecules and diffusion times estimated from FCS measurements in a single spot, in the central spot of 3×3 spots and in the most intense spot.	88
6.10.	Two examples for the location of the 3×3 spots in cells.	89
6.11.	Mean over 67 autocorrelation functions for spots located in the cytoplasm and 29 autocorrelation functions for spots in the nuclei of 12 HELA-eGFP cells.	89

7.1. Mean mFCS and FRAP curves measured in HELA-HSF1-eGFP cells.	96
A.1. Relation between the fit parameters B and τ_{off}	98
B.1. Le principe de la technique FCS.	99
B.2. Schéma illustrant la technique mFCS initialement prévue.	103
B.3. Courbes mFCS et FRAP moyennes mesurées dans des cellules HELA-HSF1-eGFP.	111

The cell nucleus is spatially heterogeneous in its structure and activity and many of its components are in dynamic interactions with each other. When investigating the cellular response to an external signal such as heat shock, standard fluorescence correlation spectroscopy (FCS) experiments, which are limited to one observation volume, do only give partial results because of the missing spatial information.

This work introduces a novel multi-confocal FCS (mFCS) technique that allows simultaneous FCS measurements in different locations within a cell. It is based on the use of a spatial light modulator (SLM) to create several distinct observation volumes at a time and an electron-multiplying charge coupled device (EMCCD) camera to perform parallel detection. The spatial resolution as well as the sensitivity of the mFCS system are close to that of a classical FCS setup and using a special readout mode, a temporal resolution of $14\mu s$ is reached.

The mFCS technique is applied to study the cellular response to thermal stress by monitoring the transcription factor heat shock factor 1 (HSF1), which is a key regulator of the heat shock response. mFCS experiments in living cells reveal changes in the dynamics of HSF1 upon heat shock. These changes concern the affinity as well as the spatial homogeneity of its interactions with DNA.

Additionally, the performance of a CMOS-SPAD camera, consisting of an array of single photon avalanche diodes, is evaluated and the device is tested as an alternative detector for mFCS in living cells.

Key words: FCS, spatial light modulator, electron multiplying CCD camera, CMOS-SPAD camera, heat shock, transcription factor HSF1

Le noyau d'une cellule est spatialement hétérogène par sa structure et son activité et beaucoup de ses composants interagissent de façon dynamique. Lors de l'étude de processus cellulaires comme la réponse au stress thermique, des expériences classiques de spectroscopie de corrélation de fluorescence (FCS), qui sont habituellement limitées à un seul volume d'observation, n'apportent que des résultats partiels à cause des informations spatiales manquantes.

Ce mémoire de thèse présente une nouvelle technique de FCS multi-confocale (mFCS) qui permet des mesures FCS simultanées à différents endroits d'une cellule. La technique est basée sur l'emploi d'un modulateur spatial de lumière pour la création de plusieurs volumes d'observations distincts et d'une caméra "electron-multiplying" CCD (EMCCD) pour la détection en parallèle. La résolution spatiale ainsi que la sensibilité du système mFCS sont proches de celles d'un système FCS classique et en utilisant un mode d'acquisition particulier une résolution temporelle de $14\mu s$ a pu être atteinte.

La technique mFCS est appliquée à l'étude de la réponse cellulaire au stress thermique en observant le facteur de transcription heat shock factor 1 (HSF1), qui est un régulateur clé de la réponse au stress thermique. Des mesures mFCS dans des cellules vivantes révèlent des changements dans la dynamique de HSF1 pendant le choc thermique. Ces changements concernent l'affinité ainsi que l'homogénéité spatiale des interactions avec l'ADN.

En outre, nous avons également évalué les performances d'une caméra CMOS-SPAD et testé le dispositif en tant que capteur alternatif pour la mFCS en cellules vivantes.

Mots-clés: FCS, modulateur spatial de lumière, caméra EMCCD, caméra CMOS-SPAD, choc thermique, facteur de transcription HSF1